Ligne InterFaces

I. INTRODUCTION

Bien que l'année 2008 se termine par un arrêt anticipé (octobre) de la ligne IF afin de réaliser l'agrandissement de la cabane SUV, tout le temps disponible en année pleine a pu être alloué via les comités. La nouvelle optique donne entière satisfaction, non seulement en termes de performances, mais aussi de fiabilité, de facilité de réglage et de reproductibilité. Aucun incident n'est venu perturber le déroulement normal des expériences.

Les publications listées en fin de ce rapport pour les deux dernières années montrent la qualité des recherches conduites sur la ligne. Une quinzaine d'articles ont été publiés dans des revues de rang A en 2008, dont un Science (facteur d'impact 26,4) , 2 Phys. Rev. Lett. (7), 2 Appl. Phys. Lett. (3,6), 3 Phys. Rev B (3,17). En 2007, une vingtaine d'articles ont été publiés dans des revues de rang A, dont un Nano Letters (facteur d'impact 10), 1 Langmuir (4), 1 Appl. Phys. Lett. (3,6), 8 Phys. Rev. B (3,17), 1 J. Appl. Phys. (2,3), 4 Surf. Sci. (1,9) . Plusieurs thèses ont été soutenues, et 2 chapitres de livre publiés.

Pour l'année à venir, le projet majeur sur la ligne est l'implémentation de la croissance par en phase chimique (UHV-CVD) sur l'instrument SUV, couplé à un agrandissement de la cabane expérimentale, pour un coût total de 400 k€ (UHV-CVD : 180 ; agrandissement : 220). Les deux postes ont dû être ré-estimés à la hausse ; l'UHV-CVD du fait de contraintes de sécurité plus grandes qu'initialement envisagé, l'agrandissement du fait de l'augmentation substantielle des coûts de matières premières (plomb …) lors de la commande. Une partie du financement (250 k€) a été obtenue via le RTRA « Nanosciences aux limites de la nanoélectronique » de Grenoble.

Les 150 k€ manquants se décomposent en 50 k€ non dépensés sur l'investissement en 2008, et 30 k€ demandés au titre de l'investissement « normal» sur SUV en 2009, plus un complément venant du CEA-INAC.

L'agrandissement de la cabane expérimentale SUV est en cours. La MBE initialement rattachée à l'instrument SUV a été déménagée au CEA-INAC en juillet 2008, puis la ligne a été arrêtée le 7 octobre, jusqu'à mi-février, pour réaliser les travaux d'agrandissement. A ce jour (fin octobre), la nouvelle cabane a déjà été montée. Restent tous les autres travaux (peinture, fluides, électricité …) à réaliser. Il est prévu de redémarrer la ligne mi-février, sur l'instrument GMT (Goniomètre Multi-Technique), durant la période de remontage de l'instrument SUV.

Nous avons un besoin urgent d'embaucher un technicien sur l'instrument SUV, poste laissé vacant par le départ Marion Noblet-Ducruet. La complexité de l'installation SUV et les très fréquentes reconfigurations de la chambre ultra-vide rendent indispensable la présence d'un technicien en CDI à plein temps sur cet instrument. Nous ne voyons pas comment continuer au rythme actuel sans ce support.

II. Développements instrumentaux

II.1. Optimisation du 1er cristal du monochromateur

Depuis la confirmation expérimentale (automne 2007) des performances mécanique du nouveau premier cristal monochomateur, la société ACCEL (fabricant de l'actuel monochromateur de la ligne IF) est intéressée pour un accord de licence. Toutefois, la société veut se persuader des performances par ses propres moyens et prépare dans ce sens une collaboration avec une ligne de Brookhaven (National Synchrotron Light Source (New York)). Au mois d'octobre 2007, le processus d'accord pourrait s'accélérer dans la réponse d'un appel d'offre d'une ligne du synchrotron anglais Diamond (Synchrotron Radiation Source, Royaume Uni). Un deuxième point positif est le projet de la ligne française CRG-D2AM d'utiliser comme la ligne IF un cristal optimisé à demeure.

II.2. Développements de monochromateur Germanium collé

Rappelons qu'il s'agit de la fabrication de monochromateurs hybrides constitués d'une couche de Germanium monocristallin reportée par collage moléculaire et amincissement sur un substrat porteur, par exemple en silicium. On bénéficie ainsi des propriétés optiques du Germanium (bande passante donc flux multiplié par trois) en conservant les propriétés mécaniques, thermiques et de coût du Silicium.
Les derniers développements de ce projet sont les suivants :

-Nous avons réalisés la chaîne complète collage/amincissement sur substrat épais et optimisé le processus de collage recuit. L'amincissement du film de Ge a été réalisé, ainsi que différents test de polissage de la surface Ge pour enlever les contraintes de surfaces.

-Les différentes mesures (diffraction haute résolution en laboratoire et topographie X (ESRF)) ont montré des erreurs de pentes sur les plans cristallins du Germanium au-delà de nos spécifications (qui sont extrêmement sévères car il s'agit d'un élément de l'optique de la ligne) . L'origine des erreurs de pentes a été identifiée et une action corrective a été entreprise. Il a fallu pour cela approvisionner des plaques de Germanium 111 épaisses que notre fournisseur habituel n'a pu nous donner à un coût acceptable. Nous avons donc dû rechercher des sources alternatives. Une solution a été trouvée récemment et le processus de polissage des surfaces a été relancé. Compte-tenu de l'expérience acquise, nous pensons atteindre, avec ce deuxième jeu de cristaux, les spécifications nécessaires pour une focalisation de faisceau synchrotron dans nos conditions.

II.3. Détecteurs

Depuis l'origine de la ligne IF nous nous efforçons de maintenir à niveau les systèmes de détection, afin de toujours proposer les systèmes les plus adaptés aux types d'expériences et permettant de développer de nouvelles techniques. C'est avec cet objectif que nous avons acheté, il y a 7 ans une caméra CCD pour développer le GISAXS tant sur SUV que sur GMT, puis en 2007 un détecteur linéaire performant pour les mesures de diffraction sur SUV. Ce système est utilisé couramment sur SUV et il a été amélioré cette année pour pouvoir contrôler le système de filtre automatiques, ce qui permet, d'une part de protéger le détecteur lors du passage sur un pic de diffraction, et d'autre part d'augmenter considérablement la dynamique du système.

II.4. Réalisation de la nouvelle tête porte échantillon pour SUV

Rappelons que la tête porte-échantillon actuelle manque de précision sur les berceaux d'alignement, et surtout sur l'alignement en translation (z) de l'échantillon dans le faisceau.
Nous lancé en 2006 avec Pierre Taunier du SERAS le projet de réaliser une nouvelle tête très précise sur ces trois mouvements, et comportant en outre deux petites translations x,y perpendiculaires au faisceau. 50 k€ avaient été alloués pour cette opération en 2006, mais,

compte tenu de la charge de travail au SERAS le projet avait dû être décalé sur 2007. L'étude (Pierre Taunier, SERAS) a été terminée fin 2007, début 2008. La figure ci-dessous présente une vue tridimensionnelle de la tête.
La mise en plan a été finie en mars 2008, et les pièces fabriquées (Patrick Tabaugat, SERAS) durant l'année 2008. La tête est à présent en cours de montage/tests au SERAS, et sera montée sur le diffractomètre au redémarrage de l'instrument SUV, en février/mars 2009.

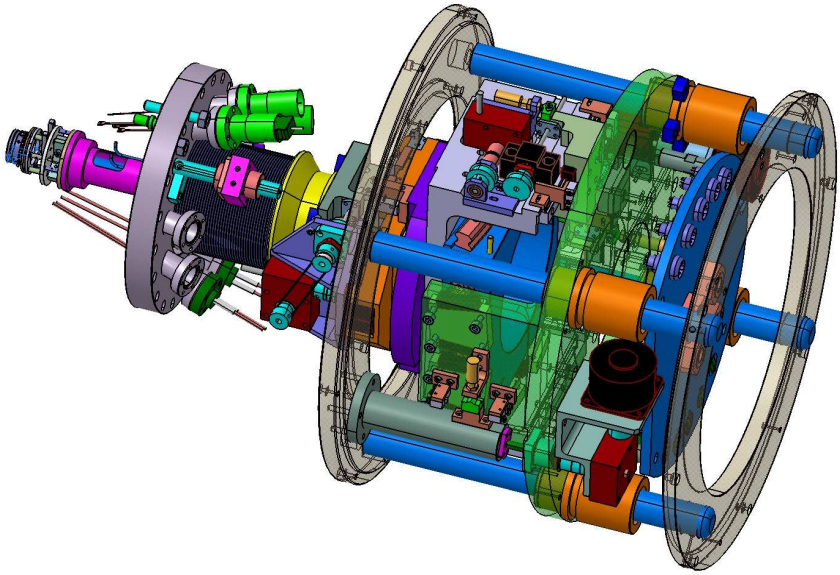

Figure : Vue 3D de la nouvelle tête goniomètrique de l'instrument SUV, conçue au SERAS par Pierre Taunier.

II.5. Développement de fentes de précision pour SUV

Le travail d'étude et de conception du système de fentes fait par un stagiaire en 2007 a permis de lancer la fabrication d'un premier bloc de fentes au SERAS. Ce projet a pour but de remplacer l'ensemble des fentes de SUV, soit 2 jeux complets en entrée, et 2 jeux sur le bras détecteur, avec pour une des fentes une ouverture plus grande pour 'être positionnée en amont du détecteur 1D. Ces fentes mettent en oeuvre des ensembles de micro-mécanique de haute précision pour atteindre des résolutions inférieures à 1µm avec une reproductibilité meilleure que 1µm, des courses de 10mm en ouverture et 5mm en offset, un défaut de parallélisme des lèvres et d'équerrage entre les deux jeux d'un bloc inférieur à 0.2°. Ce travail de micro-mécanique a été réalisé en partie au SERAS, et le premier bloc de fentes est en cours de montage. Les tests de métrologie sont prévus fin novembre. Les électroniques de pilotages seront réalisées par nos soins pour intégrer des contrôleurs performants avec une interface réseau. Le coût initialement prévu de 15k€ sera dépassé. En effet vu les tolérances requises, les usinages sont coûteux en temps, et, le SERAS ayant une trop forte charge de travail, il ne pourra pas produire les autres systèmes. Nous devrons donc faire appel à la sous-traitance ce qui explique le budget complémentaire demandé.

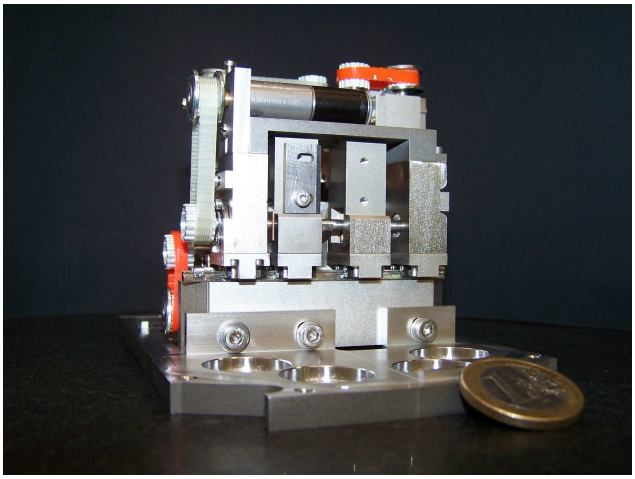

fig 1 : jeu de micro-fentes en cours de montage

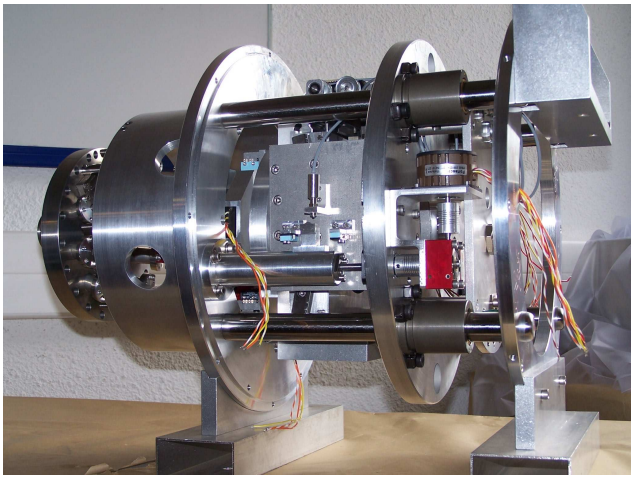

fig 2 : tête porte échantillon en cours de montage

II.6. Instrument de micro-diffraction

Les principaux développements portent sur la diminution des vibrations, l'amélioration des programmes d'acquisition, et l'intégration de machines de traction.

Les vibrations ramenées par le système de refroidissement de la caméra CCD de détection ont été coupées en découplant le châssis portant le système de focalisation KB et l'échantillon de la caméra. Pour cela nous avons construit un nouveau support pour la caméra. Le système est moins compact et plus long à mettre en place, mais ceci nous permet d'atteindre de manière routinière des tailles de faisceau de 1x1µm^2. Avec un temps de réglage plus long, des tailles plus petites sont accessibles. En jouant sur la taille de la source secondaire, on constate que les limitations pour l'obtention de tailles beaucoup plus petites sont les erreurs de forme et de polissage des miroirs KB.

Un gros effort a été fait sur les programmes et procédures d'alignement. Nous disposons maintenant de routines d'optimisation du flux sur l'échantillon, et de procédure simples pour la production du micro-faisceau.

De nombreuses mesures ont été faites avec des machines de traction, et pour certaines en dehors du plan focal; ceci au détriment de la taille. On a ainsi montré que malgré la place exiguë il reste tout de même possible dans la majorité des cas d'insérer un tel équipement. Nous avons aussi testé avec succès le montage d'un four permettant de chauffer l'échantillon, en théorie jusqu'à 900℃. Nous achèterons cet équipement en 20 09 (budget ANR) pour offrir cette fonctionnalité en standard.

Au vu des premières séries d'expériences il s'avère qu'un temps non négligeable est nécessaire pour repérer les zones à mesures sous faisceau. Ce repérage est actuellement fait sur le banc de micro-diffraction avec l'excellent microscope dont nous disposons et qui permet de distinguer des objets de 0.5µm. En 2009 nous nous équiperons d'un banc identique hors faisceau. Les utilisateurs pourraient ainsi préparer la série de mesure suivante, sans "gâcher" le temps de faisceau X.

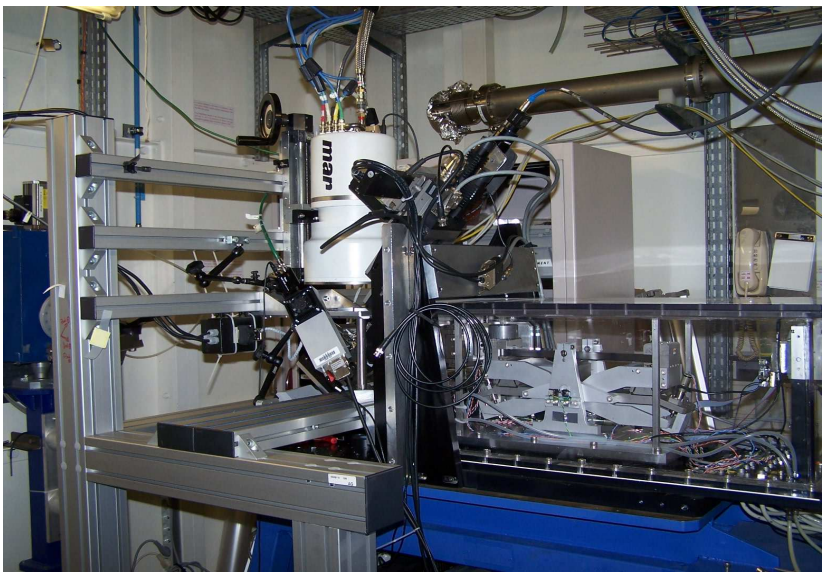

fig 3 : Banc de micro diffraction avec potence séparée pour CCD

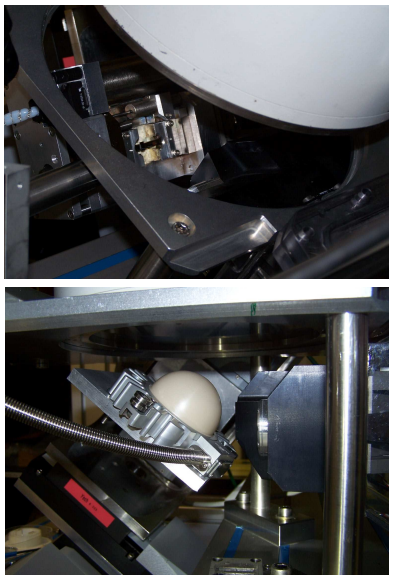

fig 4 : machine de traction et four

III Goniomètre Multi-Techniques (GMT)

III.1. Introduction

La station GMT abrite outre les expériences « traditionnelles » de diffraction réalisées à l'aide du goniomètre multitechnique les expériences de microdiffraction. Le personnel intervenant sur ces expériences comprend un ingénieur de recherche (J.S. Micha) ainsi que des chercheurs et ingénieurs CEA (F.Rieutord (resp. GMT), O. Robach, O. Ulrich, X. Biquard). Ils accueillent les utilisateurs et assurent le fonctionnement, la maintenance et le développement des instruments. L'instrument reçoit les étudiants de Master 2 et d'Hercules (et Hercules spécialisé HSC3) pour des travaux pratiques de réflectivité, diffraction de surface et micro-diffraction Laue.

Les expériences de « commisionning » (micro-diffraction, optique de ligne, performances monochromateur) utilisent pour des raisons pratiques les moyens instrumentaux de GMT. En outre, la cabane GMT et son équipement accueillent les expériences de micro-diffraction demandant un déplacement et une immobilisation du goniomètre pour laisser place au châssis supportant l'ensemble miroirs focalisants, échantillon et caméra CCD.

L'activité expérimentale a consisté cette année en une très forte majorité d'études de la matière dite dure. Trois expériences ont porté sur la matière dite molle (Assemblage de brins d'ADN, cristaux liquides et fluctuations de membranes, et une sur l'étude de surface in situ (voir M.-C. St Lager *et al*.). D'autres avaient pour sujet d'étude des matériaux des micro et nano technologies (Rieutord *et al*, Eymery *et al*, Labat *et al*) ou structure (Pesci *et al*). Les techniques générales employées sont la diffusion aux grands angles (diffraction de surface compris), la réflectivité et la diffusion centrale en incidence rasante (GISAXS). La mesure des contraintes macroscopiques par la méthode des $\sin^2\psi$ est utilisée de plus en plus fréquemment (2 expériences cette année : Pesci *et al* et Labat *et al*). Les comités français et ESRF ont sélectionné une grande majorité d'expériences conduites par des utilisateurs confirmés, maîtrisant les techniques de diffraction et diffusion des rayons X.

L'ouverture de l'instrument de micro-diffraction en faisceau blanc aux utilisateurs français et internationaux a suscité toujours un grand intérêt : cinq expériences « extérieures » ont été acceptées sur les deux comités. Du temps de faisceau a permis de remédier radicalement aux problèmes de vibrations et de trouver les modes opératoires optimaux en terme de flux et de taille de faisceau (largeurs à mi hauteur : H <1 µm V=1 µm sans perte de flux). Il a permis d'augmenter la facilité d'utilisation, le degré d'automatisation des mesures et d'accélérer la transition du mode monochromatique au mode blanc.

Le développement de l'expérience de microdiffraction bénéficie du soutien de l'Agence Nationale de la Recherche par l'intermédiaire du projet PNANO de métrologie/instrumentation MiDiFaBl , alloué aux trois partenaires CEA-INAC, CNRS- Institut Néel et CEA-Institut LETI. Grâce à ce soutien très important, nous avons entrepris ou entreprendrons différentes actions d'optimisation des performances et d'équipements de cette expérience notamment : achat d'un détecteur 2D haute performance (pixel ou CCD à anti-blooming), achat et réalisation d'équipements annexes (four, mécanique etc…). L'ANR finance également un postdoc sur la thématique dans ce cadre (Pierre Bleuet).

Deux études majeures cette année peuvent retenir l'attention. Celle de F. Rieutord *et al*, sur le collage moléculaire bénéficiant des rayons X de hautes énergies (30 voire 45 keV) et apportant un éclairage important sur les mécanismes et les paramètres gouvernant l'adhésion de wafer de Silicium. Les expériences menées par J. Eymery *et al* sont à l'image de l'arsenal de techniques de diffraction/diffusion des rayons X qu'il est possible de déployer afin de caractériser des systèmes complexes à plusieurs échelles.

Nous donnerons à la suite un descriptif d'expériences réalisées avec le goniomètre multitechnique et l'instrument de microdiffraction. Les expériences décrites par la suite correspondent à du temps alloué par le comité français (FR) et international (ESRF).

III. 2. Résultats scientifiques importants sur GMT

Etude du rôle de l'eau dans le collage moléculaire Silicium/Silicium

F. Rieutord, L. Libralesso **FR 32-02-685**

Nous avons étudié l'évolution d'interfaces de collage de silicium hydrophile au cours du recuit en température. Nous rappelons ici que l'effet du recuit est d'augmenter l'énergie d'adhérence. Malheureusement, le recuit produit également des défauts à l'interface, motivant des recherches pour comprendre les mécanismes en jeu à l'interface au cours de cette étape technologique importante. Nous avons effectué des expériences de réflectivité à haute énergie (30keV) sur des interfaces collées ayant reçu différentes préparations et traitements thermiques.

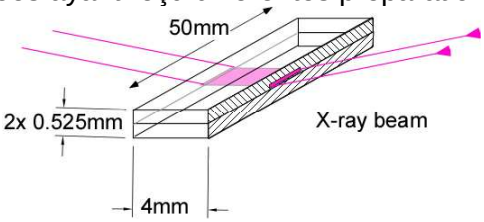

Fig.0 : Géométrie et taille typique d'échantillon dans une expérience de réflexion d'interface solide/solide à haute énergie

Ceci permet d'extraire le profil de densité électronique à travers l'interface, par inversion directe (collage symétrique) ou par des procédures d'ajustement (tous les cas). Des données typiques et les profils de densité électronique extraits sont montrés ci-dessous :

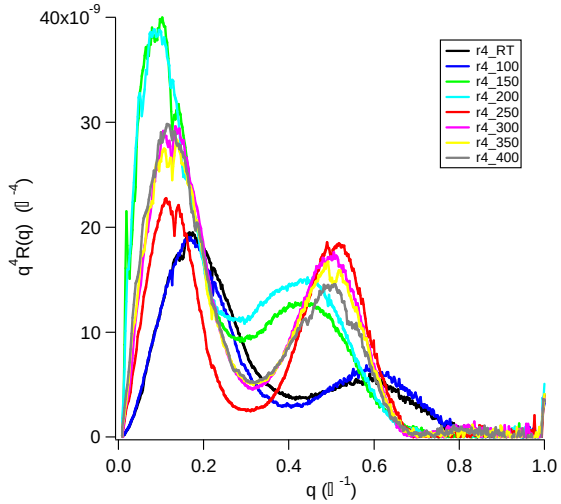

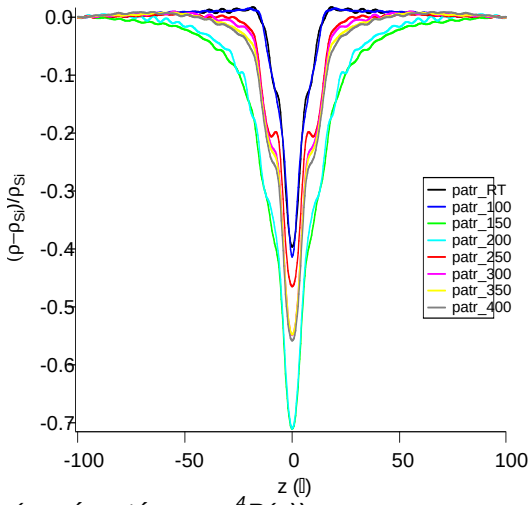

Fig.1 Courbes de réflectivité d'interface pour différents recuits (représentées en $q^4R(q)$)
Fig.2. Profils de densité électronique obtenus par inversion directe des données de la figure 1

De tels profils donnent des informations sur la largeur et la profondeur de l'interface de collage, mais également sur les couches d'oxyde. La largeur et la densité de l'interface sont liées à l'interaction entre les deux distributions d'aspérité des surfaces en vis-à-vis, et à la quantité de l'eau présente dans l'intervalle. La largeur et la densité des couches d'oxyde peuvent également être obtenues, permettant un bilan détaillé des espèces réagissant près de l'interface

De telles données ont été obtenues pour les collages Si/Si et Si/SiO2th. (NB: dans Si/Si, Si signifie silicium couvert d'oxyde natif). Les données ont montré clairement une évolution d'interface à une température environ de 150-200℃ où l'énergie de collage augmente. Nous pouvons observer une augmentation de la densité d'interface à cette température (fig. 3) ainsi qu'une croissance de l'épaisseur d'oxyde natif (Fig.4). La largeur de l'interface ne change pas de manière significative dans ces cas (non montrés).

En conclusion, utilisant la réflectivité de rayons X complétée par des données de spectroscopie de FTIR-MIR, nous avons pu déterminer le mécanisme de fermeture du collage hydrophile de silicium (ci-dessous) :

- dans une première phase, le scellement procède par extension des points de contact pilotés par

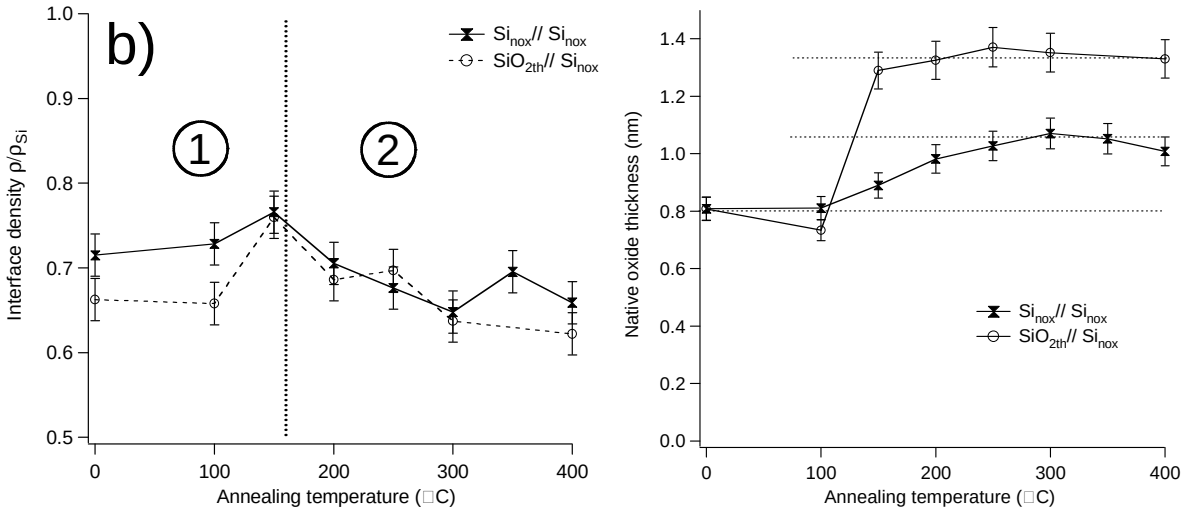

Fig.3: Evolution de la densité d'interface. Le maximum est dû à une compétition entre scellement de l'interface (qui tend à augmenter la densité) et départ de l'eau.
Fig. 4 Evolution de l'épaisseur d'oxyde natif dans les cas Si/Si et SiO2//Si. L'eau ne peut oxyder le silicium qu'au travers de l'oxyde natif conduisant à une augmentation deux fois plus importante lorsqu'un seul silicium est oxydé

l'établissement des liaisons chimiques entre les wafers. La densité de l'interface augmente car plus de silicium entrent dans la zone d'interface
- dans une seconde étape, l'eau s'échappe de l'interface, avec une diminution de la densité d'électrons.
Pendant les deux étapes, l'eau emprisonnée à l'interface ou produite par la réaction de scellement est consommée par oxydation de silicium après diffusion au travers de l'oxyde natif seulement, comme démontré par l'augmentation de l'épaisseur d'oxyde natif. Ceci libère de l'hydrogène gazeux qui est à l'origine des défauts de collage

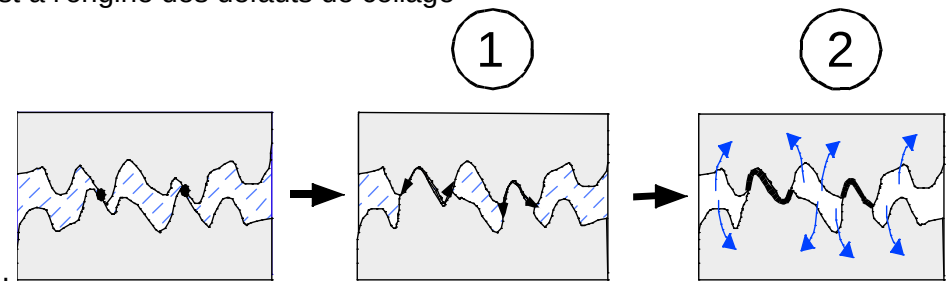

Fig.5: Schéma du mécanisme de fermeture de l'interface de collage au cours du recuit.

Reference: C.Ventosa, F.Rieutord, L. Libralesso, F. Fournel, C.Morales, H. Moriceau, *J. Appl. Phys.* (2008) , accepted.

Impact de la contrainte sur des nanofils verticaux enterrés.

J. Eymery, V. Favre-Nicolin **32-02-677**
CEA-Grenoble, INAC

Nous reproduisons en premier lieu la première page d'une publication scientifique marquante dans « Nano-Letters », relative à des résultats obtenus sur GMT en 2007.

NANO LETTERS
2007
Vol. 7, No. 9
2596−2601

Strain and Shape of Epitaxial InAs/InP Nanowire Superlattice Measured by Grazing Incidence X-ray Techniques

Joël Eymery,* François Rieutord, Vincent Favre-Nicolin, Odile Robach, Yann-Michel Niquet, Linus Frölberg, Thomas Mårtensson, and Lars Samuelson

CEA Grenoble, Département de Recherche Fondamentale sur la Matière Condensée, Service des Matériaux et Microstructures, 17 rue des Martyrs, 38054 Grenoble Cedex 9, France, and Solid State Physics, Lund University, Box 118, S-221 00 Lund, Sweden

Received April 18, 2007; Revised Manuscript Received July 26, 2007

ABSTRACT

Quantitative structural information about epitaxial arrays of nanowires are reported for a InAs/InP longitudinal heterostructure grown by chemical beam epitaxy on an InAs $(111)_B$ substrate. Grazing incidence X-ray diffraction allows the separation of the nanowire contribution from the substrate overgrowth and gives averaged information about crystallographic phases, epitaxial relationships (with orientation distribution), and strain. In-plane strain inhomogeneities, intrinsic to the nanowires geometry, are measured and compared to atomistic simulations. Small-angle X-ray scattering evidences the hexagonal symmetry of the nanowire cross-section and provides a rough estimate of size fluctuations.

The development of vertical semiconductor nanowires (NW) as new building blocks for future nanoscale electronics and photonics devices is strongly dependent on the crystalline quality. For some applications (like field effect transistors), the properties of individual (and identical) NWs must be mastered, whereas in other applications, device operation depends on the characteristics of a number of NW in parallel and therefore on the distribution width of the assembly. For example, resonant sensors or optical microcavities containing many NWs must have well-matched diameters to obtain a high quality factor.

To characterize the structural properties of these new materials, transmission electron microscopy (TEM) is a standard tool that gives first-rate information about individual objects or small assemblies including the determination of the growth directions, heterostructure cross sections, surface facets, dislocations, or stacking faults.[1,2] In spite of their very strong complementarities with TEM, X-ray diffraction techniques are up to now very seldom used to get averaged quantitative information important for practical use. Experiments on epitaxial arrays to study defects, disorientations, and strains are very limited,[3−6] and only powder diffraction or texture methods are routinely performed on broadly oriented NW growths. In this paper, we will show that with the development of the growth control, epitaxial NW heterostructures can now be effectively studied by conventional synchrotron X-ray scattering techniques,[7] i.e., grazing incidence X-ray diffraction (GIXRD) and small-angle X-ray scattering (SAXS). It will be shown that statistical quantitative information can be obtained concerning epitaxial relationships, orientation distributions, strain relaxation, and stacking defects. These points will be illustrated by the detailed analysis of a 20 period InAs/InP nanowire superlattice, including comparison to simulation.

The nanowire growth is Au-assisted and takes place in a chemical beam epitaxy (CBE) system using trimethylindium, precracked *tert*-butylarsine, and precracked *tert*-butylphosphine as growth precursors.[8] Prior to growth, size-selected Au aerosol particles are deposited on a $InAs(111)B$ substrate and the sample is deoxidized in the growth chamber at 520 °C under As pressure. Growth is started at 425 °C for about 530 nm of InAs and then further lowered to 390 °C for the superlattice growth with 20 segments of 20 nm (InAs) and 10 nm (InP). The structure is ended with an InAs segment of about 65 nm.

Figure 1 shows scanning electron microscopy (SEM) images of the sample, indicating that most of the NWs are perpendicular to the surface with a standard hexagonal cross section. TEM analysis shows $\langle 11\bar{2} \rangle$ side facets referred to the cubic substrate and a Wurtzite structure of the nanowire; we have never seen any cubic insertion at the bottom of the nanowire or anywhere else.[8] On top of the surface, small pyramidal hillock overgrowths can be observed (see Figure 1h,e). The narrow NW orientation distribution allows studying the NW reciprocal space according to the substrate lattice, and the (hkl) Miller indexes, corresponding to the $InAs(111)_B$

* Corresponding author. E-mail: joel.eymery@cea.fr. Équipe Mixte CEA-CNRS-UJF, Nanophysique et Semiconducteurs, CEA Grenoble.

10.1021/nl0708891 CCC: $37.00
Published on Web 08/29/2007

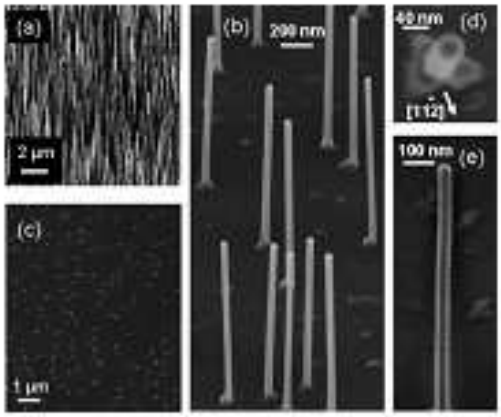

Figure 1. Scanning electron microscopy images of CBE grown epitaxial nanowires. (a,b) tilted views, (c,d) top views, showing the vertical alignment and the hexagonal cross section with facets corresponding to the [11$\bar{2}$] direction indexed in the cubic substrate lattice; (e) side view, where the superlattice periods are barely seen (see cover picture for a SEM picture in the transmission geometry).

surface unit cell, can be used as a reference. The surface unit cell lattice vectors have a hexagonal basis $\mathbf{a}_1$, $\mathbf{a}_2$, $\mathbf{a}_3$ with $\mathbf{a}_1 = \frac{1}{2}[\bar{1}10]$, $\mathbf{a}_2 = \frac{1}{2}[0\bar{1}1]$ in the surface plane, and $\mathbf{a}_3 = [111]$ perpendicular to the surface. The corresponding reciprocal lattice vectors are along three h,k,l axes with h and k in the surface plane, making an angle of 60° and l normal to the surface. In these coordinates, InAs $(111)_B$ bulk Bragg reflections are found at $l = 1, 4, 7, \ldots$ for $(h,k) = (1,0)$ and at $l = 2, 5, 8, \ldots$ for $(h,k) = (0,1)$. X-ray experiments were performed at the European Synchrotron Radiation Facility (ESRF, Grenoble France) under helium flow to prevent sample degradation and to avoid background diffuse scattering from the air. Diffraction (respectively, small angle) data were collected on the BM32 French CRG beamline using 10 (respectively, 18) keV photon energy. The beam footprint on the sample surface, which is about 5 × 0.5 (0.1) mm^2, integrates the intensities of a very large number of NWs.

Figure 2 shows the measurements of the $(01l)$ crystal truncation rod (CTR) for several grazing incidence angles α. Close to the substrate critical angle for total external reflection ($\alpha_c = 0.29°$), we measure at $l = 2$ and 5 the sharp and intense diffraction peaks of the InAs substrate (labeled S). Their intensities decrease with decreasing α and vanish in the "transmission" geometry ($\alpha = 0°$). The extra peaks may come either from the NWs or from other surface overgrowths. Peak intensities at $l \approx 1.5$, 3, and 4.5 (labeled NW in Figure 2) do not depend on the incidence angles, whereas some "satellites" at $l \approx 1$, 2, 4, and 5 (labeled TW, for twinned overgrowth) do. This strongly suggests that noninteger peaks can be attributed to the NWs. It is confirmed by the peak-shape dependence on the incidence shown in the inset of Figure 2. In the transmission geometry and for α close to the critical angle, only a single peak is measured. In intermediate cases, a second peak is measured. Its larger-angle position depends on α, and at $\alpha = 0.1°$, the two peaks overlap. These observations can be explained by using the distorted-wave Born approximation (DWBA). In

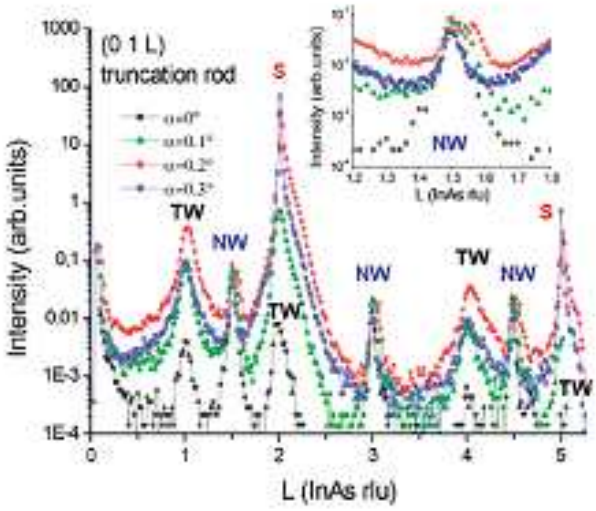

Figure 2. $(01l)$ crystal truncation rod measurement for several grazing incidences ($\alpha = 0$, 0.1, 0.2, 0.3°). l is in reciprocal lattice units (rlu) of the cubic InAs(111) substrate (marked by S). NW (TW) correspond to the nanowires (substrate overgrowths) peaks. Inset: splitting of NW-peak at $l = 1.5$ in two contributions as the function of α. This effect is explained in the text by the coexistence of several scattering processes at very grazing angle.

this formalism, the scattered wave amplitude is composed of four terms, including all combinations of scattering from the NW and reflection from the substrate.[9] At very low grazing incidence (transmission geometry), the incident beam is scattered by the NW and collected by the detector, whereas at larger α (but lower than α_c), a second contribution comes from the reflection by the surface toward the NW. This reflection acts as a second "incident beam" with a wave vector pointing slightly upward. The surface reflection is sharply decreased for $\alpha > \alpha_c$, which explains why the two terms are observed only at very grazing angle. The third and fourth term considered in DWBA, coming respectively from the beam scattered by the NW and reflected by the surface and from both incident and scattered beam reflected by the surface, are negligible because downward scattered beams have an angle much larger than α_c with respect to the surface. This multiple scattering effect also applies to the TW peaks, and a small shift is observed with α, but peak broadness causes the two contributions to overlap. The TW peaks intensities decrease with the incidence suggesting a different origin.

To have more insights about the nature of these peaks, we measure for $\alpha = 0.3°$ several CTRs in the $(h0l)$, $(0kl)$, and (hhl) reciprocal planes (see some examples in Figure 3b,c). Figure 3a summarizes the $(h0l)$ measurements referred to the InAs cubic substrate lattice. Zinc-blende InAs substrate and hexagonal NWs peaks are easily indexed by considering the stacking sequence of (111) planes.[6] Note that two variants having the same peak intensities are measured for the hexagonal NWs. They correspond to "equivalent" 60° rotations domains, which can be probably attributed to different NWs orientations on the (111) surface. TEM observations rule out defects in individual NWs, moreover, this kind of defect should not give identical domains

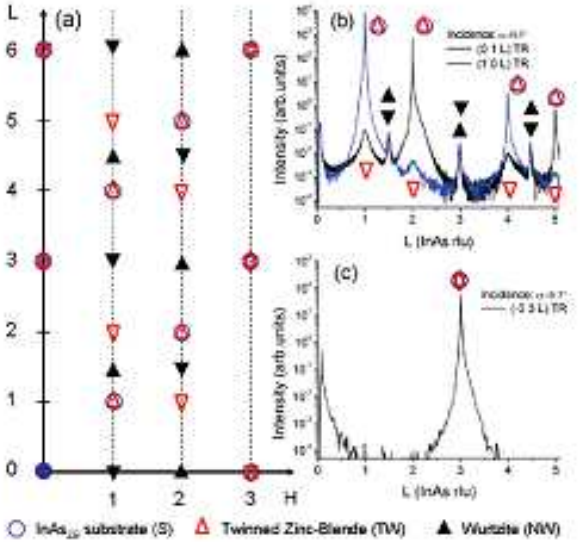

Figure 3. (a) Schematics of the (*h*0*l*) reciprocal plane of the sample shown in Figure 1 (*h*,*l* scales and peak positions are only indicative): (○) InAs cubic substrate, (▲▼) hexagonal NW variants obtained by 60° in-plane rotations, (△▽, in red) twinned cubic substrate overgrowth (ACB stacking of the (111) planes instead of ABC). (b,c) Truncation rod measurements examples (*l* scans) for $\alpha = 0.3°$: (b) along (10*l*) and (01*l*) (equivalent to (20*l*) in (a)), and (c) along (−33*l*).

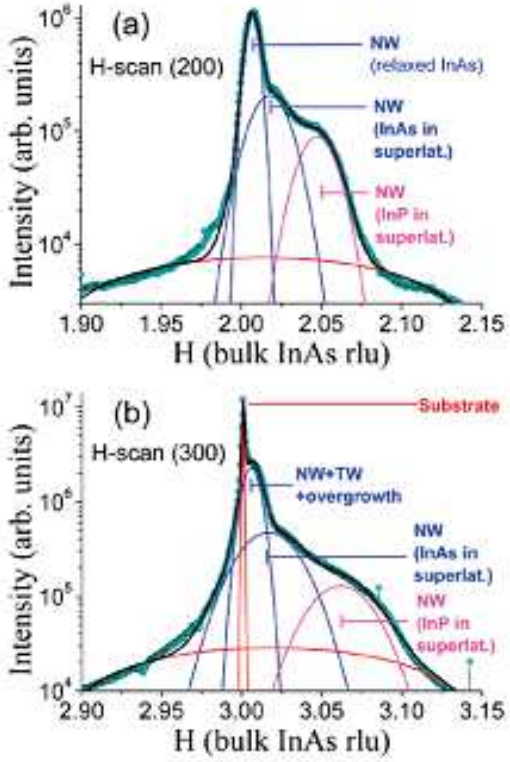

Figure 4. In-plane measurements along *h* (see the definition in Figure 3) for the (a) (200) and (b) (300) reflections. Points correspond to measurements and thick curves to the best fits of the nanowires (NW), twinned overgrowth (TW), and substrate (S) contributions. *h* is in reciprocal lattice units (rlu) of the cubic InAs-(111) substrate.

intensities. The TW peaks are consistent with twins of a cubic phase having a lattice parameter close to the substrate. They can be attributed to the pyramidal hillocks observed by SEM (see Figure 1b,c) in agreement with the α-dependence shown in Figure 2 and with the in-plane orientation distribution (mosaicity) discussed later. The hillock morphology is commonly observed in zinc-blende (111) epilayers for II−VI and III−V compounds. This structure may be nucleated on a surface defect (for example on a gold contamination coming with the aerosol catalysts). The stable cubic phase is obtained due to the strong coupling with the surface. Indeed, we do not have the influence of the NW geometry (dimension and surface effects) that could stabilize the metastable hexagonal structure. The NW and TW lattice parameters are deduced both from in-plane ⟨200⟩, ⟨300⟩, and out-of-plane ⟨01*l*⟩ measurements according to the cubic phase reference ($a^{InAs}_{Subst} = 0.60583$ nm and $a^{InP}_{Subst} = 0.58687$ nm).

As shown in Figure 4, the fit of in-plane measurements (reflections perpendicular to the surface) allows determination of the different contributions to the measured intensity: the substrate overgrowths, the relaxed InAs segments at the bottom and the top of the nanowire, and the average InAs and InP insertions in the superlattice. For the sake of simplicity, we chose a Gaussian function to model the Bragg peak shape. This choice is adequate to describe the center position and the width of the peak, but it is surely not enough to describe the peak tails. A more complicated description (with more parameters to fit) should take into account these features. It should probably decrease the background below the signal (see the red curve in Figure 4), but up to now no strong physical argument can be given to select the function type (Lorentz, Voigt, Pearson...). Wurtzite InAs NW position (shown in (200) *h* scan and in Figure 3) is slightly larger than the cubic InAs substrate. It corresponds to the bottom and to the top of the NW and should be relaxed due to the small NW diameter and to the small lattice mismatch: the in-plane lattice parameter is only decreased of about 0.32% ± 0.03 according to the substrate reference. For the (003) measurement (see Figure 4b), the relaxed InAs NW signal is superposed to the TW contribution and eventually to planar (and not twinned) substrate overgrowth. The fit of this composite peak gives 0.17% ± 0.03, suggesting that the two last phases are very close to bulk cubic InAs. For the NW superlattice, the InAs and InP average in-plane lattice parameters can be estimated by the positions of the peak maxima of (002) and (003) *h* scans: $a^{InAs}_{NW}/a^{InAs}_{Subst} = 0.9936 \pm 0.001$ and $a^{InP}_{NW}/a^{InAs}_{Subst} = 0.9787 \pm 0.001$ (see also the Table 1). It was difficult to assess accurately c^{InP}_{NW} due to the low experimental resolution used in CTR measurements and to the low signal, but for InAs, we measured $c^{InAs}_{NW} \approx a^{InAs}_{NW}/\sqrt{2}$. Note that no clear signals due to the NW superlattice periodicity have been measured in these experiments. It may be due to several reasons, the effects of which are probably combined: strain relaxation distribution along the NWs, disorientations, section variations induced by the catalyst particle's diameter distribution and growth fluctuations (the

Table 1. Calculated Averaged In-Plane Deformation $\langle \epsilon_{yy} \rangle$ for Nanowire Superlattices with Radius $R = 22$ nm Consisting of 20 nm InAs/7 or 10 nm InP Layers[a]

		20 nm InAs/ 7 nm InP NW	20 nm InAs/ 10 nm InP NW
$\langle \epsilon_{yy} \rangle$ (%)	InAs (-0.64 ± 0.1‡	−0.46	−0.61
	InP (-2.13 ± 0.1‡	−1.82	−2.15
σ_{yy} (%)	InAs:	0.37	0.42
	InP:	0.50	0.43

[a] The atomic positions are relaxed with the valence force field described in the text. The deformations are calculated with respect to the cubic InAs reference and the experimental values are parenthesized. The standard deviations (σ_{yy}) of these deformations show the intrinsic broadening of this longitudinal nanowire structure.

longitudinal growth rate, and therefore the insertion thickness, varies with the NW diameter), or to a height (i.e., phase) shift coming from a nucleation delay before the beginning of the growth of individual NW.

The diffraction peak broadening may have several origins: (i) the NW size along the momentum transfer, (ii) the NW mosaicity corresponding to the in-plane (twist) and out-of-plane (tilt) rotations of the individual NWs, (iii) a nonuniform strain field with a local lattice parameter variation, including heterostructure strain relaxation and bending of the growth axis. (ii) and (iii) depend on the modulus of the momentum transfer, whereas (i) does not.

In-plane mosaicity is measured from transverse scans along (*h*00) reflections (rocking scan of the sample along its surface normal). It gives a full width at half-maximum (fwhm of a Gaussian function) of the TW peaks lower than 0.02°, whereas the NW peaks have an in-plane mosaicity of about $0.5 \pm 0.1°$. The fwhm of in-plane radial scans along [*h*00] (for example, for the relaxed InAs peak of Figure 4a) is 0.143 ± 0.006 nm^{-1}, which can be attributed to a NW cross-section diameter between hexagonal facets of about 44 ± 2 nm. This value, consistent with Figure 1, will be confirmed by SAXS measurements below.

The experimental results can be compared to atomistic simulations. We consider hexagonal [0001]-oriented InAs/InP nanowires superlattices with the wurtzite structure. The edge length (and radius) of the regular hexagon ($\{10\bar{1}0\}$ facets in hexagonal notation) is $R = 22$ nm, and the period of the superlattice is $l \approx 30$ nm. The thickness of the InAs layer is 20 nm, while the thickness of the InP layer is varied from 7 to 10 nm. The relaxed atomic positions are computed using Keating's valence force field (VFF model).[10] In this model, the elastic energy depends on the nearest-neighbor bond lengths and bond angles through bond stretching and bond bending constants. These parameters are fitted to the bulk modulus and Poisson ratio ν_{111} of the zinc-blende materials,[11−12] assuming that the elastic constants of the wurtzite phases fulfill Martin's relations.[13] The elastic energy is then minimized with respect to the atomic positions and period of the superlattice using a conjugate gradients algorithm, and the strain tensor is computed from the atomic positions in the $x = [2\bar{1}\bar{1}0]$, $y = [01\bar{1}0]$, and $z = [0001]$ axis set. Within this axis set, the k scans of GIXRD correspond to the y direction perpendicular to the hexagonal facets.

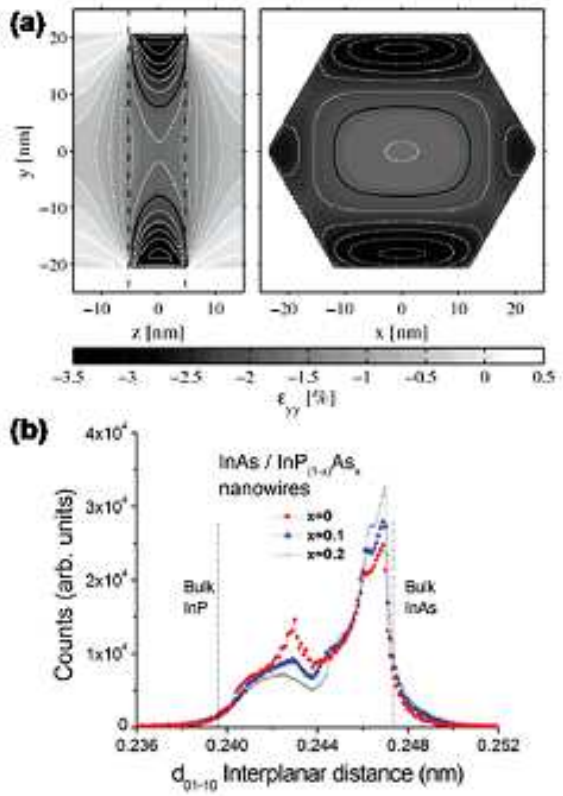

Figure 5. (a) In-plane deformations ϵ_{yy} (with reference to bulk InAs) for a 20 nm InAs/10 nm InP nanowires superlattice (cross sections at $x = 0$ and $z = 0$, respectively). The atomic positions are relaxed with the valence force field model described in the text. The black line is $\epsilon_{yy} = -2\%$, the difference between white dotted lines being $\Delta\epsilon_{yy} = 0.25\%$. (b) Histogram of the distances between $(01\bar{1}0)$ planes (perpendicular to the y direction; i.e., parallel to the hexagonal facets) for a 20 nm InAs/10 nm InAs$_x$P$_{1-x}$ nanowires superlattices with $x = 0$, 0.1, 0.2.

The in-plane deformation ϵ_{yy}, computed with reference to bulk InAs,[15] is shown in Figure 5a for the 20 nm InAs/10 nm InP structure. The InP layer, whose elastic constants are close to InAs, is heavily compressed by the latter. The surface of the nanowires can, however, bulge to relieve part of the stresses, which leads to a very inhomogeneous strain distribution (see for example refs 12 and 14 for a discussion of the electronic and optical properties of InAs/GaAs nanowire superlattices). The average in-plane deformations in InAs and InP are reported in Table 1 for two InP thicknesses (7 and 10 nm). The standard deviations of these values are very large even for ideal objects, indicating that the strain inhomogeneity is an intrinsic source of the peak broadening observed in GIXRD. These distributions must be taken into account to optimize band gap strain engineering in complex heterostructures. The strains are, moreover, very close to those computed in similar zinc-blende nanowire superlattices.

The calculated average in-plane deformations in InAs and InP (inside the 20 nm InAs/10 nm InP NW superlattice) are in very good agreement with the experimental values parenthesized in Table 1. The impact of various structural

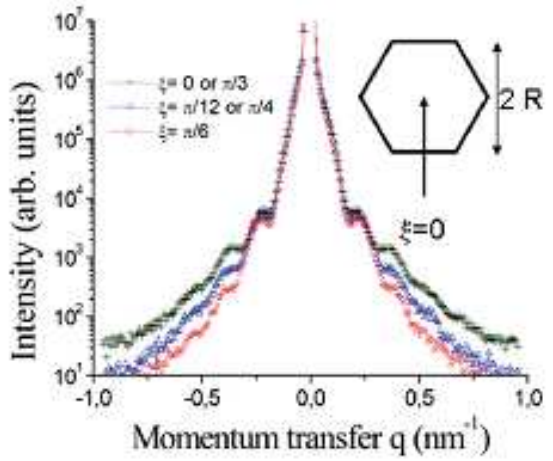

Figure 6. Small-angle X-ray scattering measurements for several azimuth ξ (see inset for definition) as the function of the momentum transfer $q = 4\pi \sin(\theta)/\lambda$ (θ is half of the scattered angle, λ is the wavelength). Grazing and emergence angles are very low (a few hundredths of a degree). Only three measurements (i.e., azimuths) are drawn, representative of the $\pi/6$ symmetry of the scattered intensity.

parameters (thickness of the InP layer, presence of an InAs shell, interdiffusion) has been investigated. The deformations in thinner (7 nm) InP layers are actually too small. The calculated deformations in core/shell 20 nm InAs/10 nm InP NW superlatices remain quite close: for a 1 nm thick InAs shell around a core with radius $R = 21$ nm, we get $\langle \epsilon_{yy} \rangle_{InAs} = -0.60\%$ and $\langle \epsilon_{yy} \rangle_{InP} = -2.04\%$, while for a 2 nm thick shell around a core with radius $R = 20$ nm, we get $\langle \epsilon_{yy} \rangle_{InAs} = -0.57\%$ and $\langle \epsilon_{yy} \rangle_{InP} = -1.94\%$. The interdiffusion is very limited for the low-temperature growth used in this study (390 °C): TEM energy dispersive spectrometry experiments estimate that the P atom concentration in InAs is lower than 2% (i.e., the noise level). For higher growth temperature, the influence of the substitution of P atoms by As in the InP layer (i.e., the insertion material) can be assessed by the distance between the $(01\bar{1}0)$ planes parallel to the nanowires edge (i.e., perpendicular to the k direction). Figure 5b gives the histogram of this distribution for 20 nm InAs/10 nm $InAs_xP_{1-x}$ superlattices with $x = 0$, 0.1, 0.2. It shows that a small substitution of P atoms largely shifts and broadens the initially "peaked" InP contribution, which can also contribute to an increase of the width of the in-plane diffraction peaks. Experimentally, the separation of interdiffusion and elastic relaxation contributions should be obtained by X-ray anomalous measurements around the As k absorption edge (11.868 keV).

After having analyzed the in-plane deformation with X-ray diffraction, we can also access to the average NW shape and size of this assembly by using small-angle X-ray scattering (SAXS)[15] at very grazing incidence and emergence ($\alpha = \beta \approx 0.1°$). Figure 6 shows selected intensity measurements $I(q)$ as a function of the in-plane scattering vector q for several sample orientations (azimuth) around the surface normal. Contrary to what is measured for cylindrical cross sections, we observe the dependence on the azimuth ξ of the

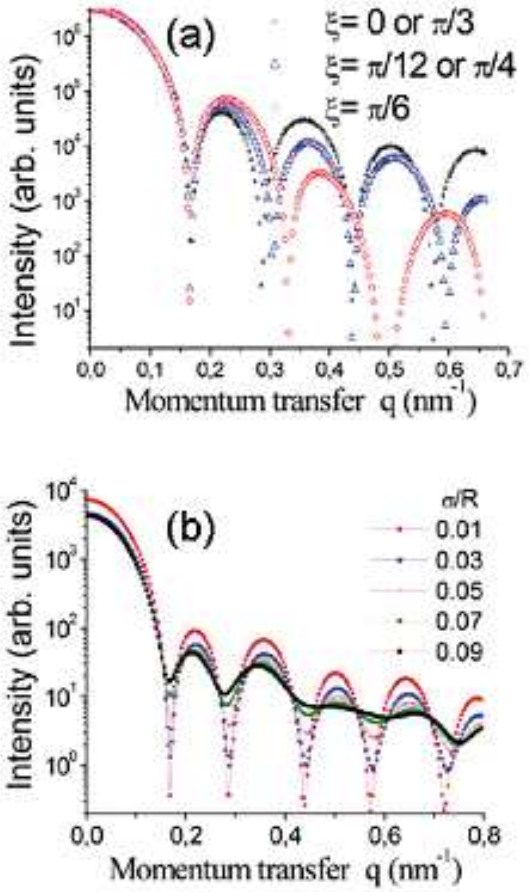

Figure 7. (a) DWBA calculation[10] of the in-plane intensity scattered by uncorrelated regular hexagonal NW of radius $R = 22$ nm at grazing incidence and emergence angles ($\alpha = \beta = 0.1°$). No size distribution is included in these calculations, and the azimuth ξ is defined by the inset of Figure 6. (b) Small-angle intensity calculated at $\xi = 0$ for a Gaussian distribution of the radius R of hexagonal NW. σ is the standard deviation of the R distribution ($\exp[-(x - x_0)^2/(2\sigma^2)]/[(2\pi)^{1/2}\sigma]$), and σ/R indicates the broadening.

oscillation fringes due to the NW size in a direction perpendicular to the beam both in position and intensity. The origin $\xi = 0$ is defined by a direction perpendicular to the NW facets (k direction in the diffraction experiments), as shown in the inset of Figure 6. The systematic measurement of $I(q)$ as a function of ξ (over $\pi/2$, every $\pi/36$) has shown a $\pi/6$ symmetry. The main features of the azimuth−angle dependence consist of the damping and the shift of the second-order fringe from $\xi = 0$ to $\pi/6$ and of the disappearance of the third oscillation at $\xi = \pi/6$. The center part of the experimental curve comes from the surface and overgrowth scattering. Note that in this sample, the NW density is very low (only about 2.5 NWs/μm^2 from Figure 1) so that synchrotron radiation is necessary. For higher densities, this method should be applied with a laboratory setup. Because no interparticle−position interactions have to be considered (see Figure 1c where the distribution of distances between nearest-neighbors NWs is very broad), the X-ray pattern can be analyzed as a convolution of the NW form factor by the

size distribution function. This form factor, derived in the simplest approximation from the Fourier transform of the NW shape,[15-17] can be calculated with the DWBA for a regular hexagon of height H and facet width R. As seen in Figure 7a, all the main features of the experimental measurements can be simulated by a monodisperse size distribution with $R = 22$ nm. The sharp interferences fringes appearing at roughly $q_R \sim 2\pi/R$ are associated to the zero of the sine cardinal or Bessel function for simple shapes like parallelepiped or cylinder. As observed in electron microscopy, the growth distribution involves both size and shape variations of the hexagonal cross sections with eventually a variation along the wire length. In a first approximation, only the R variation will be considered, giving a fringe smoothening with the increase of the width of the size distribution. This distribution can be modeled by a Gaussian function (fwhm σ) in the DBDA calculations. The calculated intensity for $\xi = 0$ is drawn in Figure 7b as a function of σ/R. Because the experimental measurements still show the third oscillation fringe, the maximum of the size distribution can be roughly estimated to be lower than $\sigma/R < 8\%$. This variation is mainly imposed by the aerosol particle size distribution and by fluctuations of the catalyst-assisted growth. More accurate measurements with 2D detectors in the grazing incidence SAXS geometry are presently under way to decrease the error bars and to study facets distribution.

In summary, this letter demonstrates the interest of X-ray grazing incidence techniques to get quantitative structural information on epitaxial NWs assemblies. The change of grazing incidence angle in surface diffraction experiments allows separating the different contributions of the signal, i.e., the nanowires from parasitic substrate overgrowths. More generally, these methods could be advantageous when studying samples grown by molecular beam epitaxy, which is a less selective growth method, leading to a larger overgrowth at the nanowires base. The crystalline phases (cubic or hexagonal) as well as growth defects (stacking faults) are determined from the direct analysis of crystal truncation rods. In the present study, the InAs/InP heterostructure was entirely hexagonal with equivalent variants, and a second twinned phase is present only as a substrate overgrowth. The same method could also be applied to inhomogeneous NW (for example GaAs) having a mixture of hexagonal and cubic phases. The in-plane epitaxial disorientations of the NW are small (fwhm $\approx 0.5°$), indicating a very good control of the initial growth stage consistent with classical mosaicity observed in metal (aerosol)/semiconductor substrate epitaxy. The strain distribution resulting from the relaxation in the NW geometry, measured from the position and broadening of the diffraction peaks, is in agreement with atomistic calculations of ideal structures. Complementary experiments using small-angle scattering have shown the possibility to check the size and shape of the objects. This method seems to be very promising in homogeneous assemblies to estimate such geometrical fluctuations, in particular with colloid-assisted growth, where synchrotron experiments are not necessary for dense assemblies. Last, grazing incidence X-ray techniques can be developed to study and to optimize the NW growth mechanisms or the technological processes. They will be helpful to integrate well-controlled NW building blocks into functional assemblies, and ultimately into systems.

Acknowledgment. This work has been performed under the EU program NODE 015783. We thank the French CRG-IF and ID01 ESRF beamlines for their technical help.

References

(1) Bell, D. C.; Wu, Y.; Barrelet, C. J.; Gradečak, S.; Xiang, J.; Timko, B. P.; Lieber, C. M. *Microsc. Res. Techn.* **2004**, *64*, 373.
(2) Johansson, J.; Karlsson, L. S.; Svensson, C. P. T.; Mårtensson, T.; Wacaser, B. A.; Deppert, K.; Samuelson, L.; Seifert, W. *Nat. Mater.* **2006**, *5*, 574.
(3) Bakkers, E. P. A. M.; Van Dam, J. A.; De Franceschi, S.; Kouwenhoven, L. P.; Kaiser, M.; Verheijen, M.; Wondergem, H.; Van Der Sluis, P. *Nat. Mater.* **2004**, *3*, 769.
(4) Svensson, C. P. T.; Seifert, W.; Larsson, M. W.; Wallenberg, L. R.; Stangl, J.; Bauer G.; Samuelson, L. *Nanotechnology* **2005**, *16*, 936.
(5) Kawamura, T.; Bhunia, S.; Watanabe, Y.; Fujikawa, S.; Matsui, J.; Kagoshima, Y.; Tsusaka, Y. *J. Appl. Phys.* **2005**, *97*, 084318.
(6) Mandl, B.; Stangl, J.; Mårtensson, T.; Mikkelsen, A.; Eriksson, J.; Karlsson, L. S.; Bauer, G.; Samuelson L.; Seifert, W. *Nano Lett.* **2006**, *6*, 1817.
(7) Metzger, T. H.; Schülli, T. U.; Schmidbauer, M. *C. R. Phys.* **2005**, *6*, 47.
(8) Larsson, M. W.; Wagner, J. B.; Wallin, M.; Håkansson, Fröberg, L. E.; Samuelson, L.; Wallenberg, L. Reine *Nanotechnology* **2007**, *18*, 015504.
(9) Rauscher, M.; Paniago, R.; Metzger, H.; Kovats, Z.; Domke, J.; Peisl, J.; Pfannes, H. D.; Schulze, J.; Eisele, I. *J. Appl. Phys.* **1999**, *86*, 6763.
(10) Keating, P.-N. *Phys. Rev.* **1966**, *145*, 637.
(11) Niquet, Y.-M. *Phys. Rev. B* **2006**, *74*, 155304.
(12) *Physics of Group IV Elements and III-V Compounds*, Madelung, O., Schulz, M., Weiss, H., Eds.; Landolt-Börnstein, New Series, Group III, Vol. 17, Part A; Springer-Verlag: New York, 1982.
(13) Martin, R. M. *Phys. Rev. B* **1972**, *6*, 4546.
(14) Niquet, Y.-M. *Nano Lett.* **2007**, *7*, 1105.
(15) Lazzari, R. *J. Appl. Crystallogr.* **2002**, *35*, 406.
(16) Vargas, R.; Louër, D.; Langford, J. I. *J. Appl. Crystallogr.* **1983**, *16*, 512.
(17) Boudet, A.; Conchon, F.; Guinebretière, R. *Acta Crystallogr., Sect. A: Found. Crystallogr.* **2006**, *A62*, 11.

NL0708880

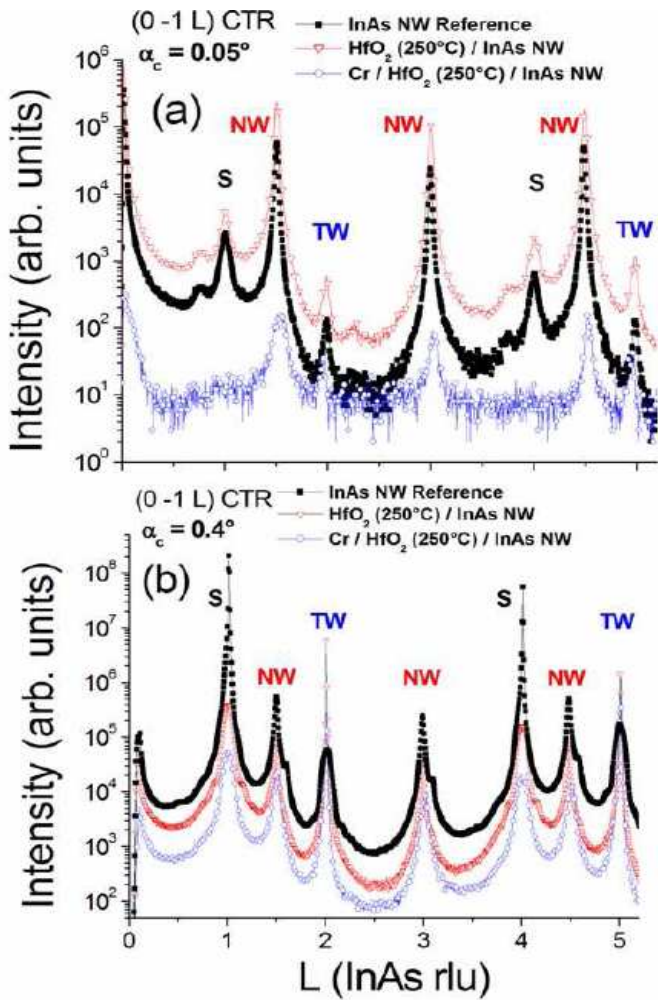

Figure 4 : Mesure des tiges de troncatures (0 -1 l) (CTR) de la reference et des structures core/ pour deux incidences rasantes (a) α=0.05° and (b) 0.4°. l est l'unité du réseau réciproque (rlu) du substrat(S). cubique InAs(111) (noté S).

Après avoir étudié les hétérostructures longitudinales de nanofils InAs/InP nous avons focalisé nos études sur des structures de type coeur/coquille qui sont à la base des architectures de transistors et d'émetteurs optiques. Cette expérience a été conduite avec des échantillons provenant de l'Université de Lund (Suède), leader dans le domaine des composés III-V (croissance CBE) et plus particulièrement sur des empilements radiaux de diélectriques et de métaux (HfO2 et Cr) sur des fils d'InAs (111). Ces structures sont dès à présent utilisées dans des transistors verticaux et donne de bonnes caractéristiques électriques. Un des points primordial pour ce type de structure est de ne pas rajouter de défauts en reprenant la croissance latérale et de maîtriser la contrainte introduite par les procédés technologiques. Ces deux points ont été étudiés par diffraction de rayons X en incidence rasante lors de différentes étapes technologiques de la création d'un transistor: InAs NW nus (i.e. référence), HfO2 / InAs NWs et Cr / HfO2 / InAs NWs (Voir Fig. 1).

Plusieurs techniques de caractérisation ont été effectuées durant 18 shifts : Diffraction de surface (diffraction dans le plan de la surface et tiges de troncature), réflectivité et diffusion centrale en incidence rasante (GISAXS).

La diffraction dans le plan a été effectuée en géométrie GIXRD, la qualité de l'épitaxie permettant de définir une matrice d'orientation par rapport au substrat InAs (111) cubique. Les fils d'InAs sont hexagonaux et ont des pics de diffraction dans le plan comme nous l'avons montré dans une publication précédente. Les expériences ont montrées que pour toutes les variantes étudiées, le déplacement des pics dans le plan était très faible (dans la barre d'erreur des mesures), ce qui indique une déformation faible dans le plan. Un point plus remarquable correspond à l'élargissement de ces pics de diffraction pour des balayages radiaux des réflexions h 0 0. Cet élargissement est notable surtout pour les dépôts de Cr, avec une augmentation linéaire en fonction de h. Comme le montre la figure, cette largeur est d'autant plus importante que l'incidence est rasante. L'analyse de ces données permettra d'obtenir la taille des domaines (i.e. les fils, à comparer avec les images MEB) ainsi qu'une « mosaicité » liée essentiellement au dépôt de Cr qui doit rendre les contraintes plus inhomogènes.

D'après les mesures précédentes, la déformation radiale est faible. La déformation longitudinale a été estimée grâce à l'analyse des **tiges de troncature** (0 -1 /) pour les quatre échantillons. La Figure 4 présente quelques mesures pour les angles d'incidence α=0.05° et 0.4° respectivement en dessous et au dessus de l'angle critique de réflexion totale. Comme on l'a déjà montré dans ce système, ces mesures permettent de séparer les contributions des différentes phases de l'échantillon (voir indexation sur la Figure 4: N nanofils, TW recroissance sur le substrat et S

substrat). Pour α =0.4° et l =4, on voit que la position du pic du substrat est insensible au dépôt des diélectriques et du métal. Cela fournit une référence interne à l'échantillon et permet de vérifier l'alignement du goniomètre et de baisser la barre d'erreur. Ainsi, la barre d'erreur de la position du pic S est estimée à ±0.065% en considérant trois incidences rasantes (0.05°, 0.2°, 0.4°), deux CTRs ((0 -1 l) , (0 -2 l)), et quatre valeurs de l (1, 2, 4, 5).

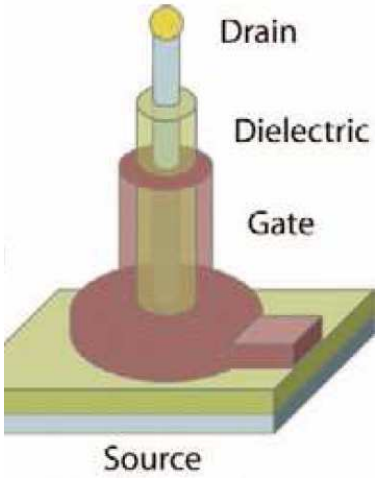

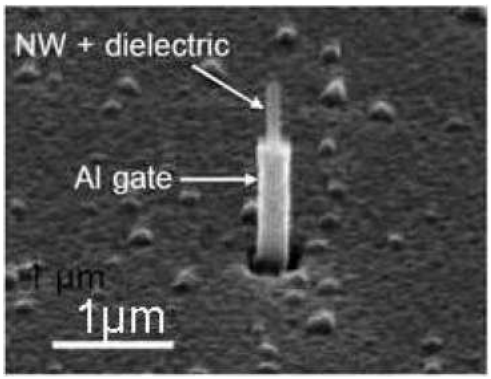

Figure 1 : géométrie utilisée dans les nanofils et image MEB de l'épitaxie sur InAs.

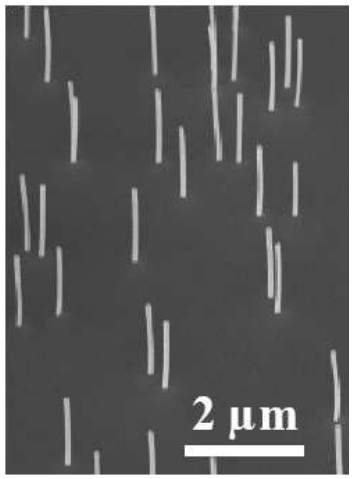

Les nanofils ont des pics distincts (appelés NW) de ceux du substrat et des recroissances (TW) ce qui permet de mesurer la déformation le long de l'axe de croissance. Pour α =0.4° et l =4.5, les pics NW sont faiblement déplacés pour les nanofils avec HfO2 et beaucoup plus lorsqu'on a la coquille supplémentaire de Cr. La contraction le long de la direction de croissance est de 0.95 % ±0.07 pour Cr/HfO2 (T=250℃)/InAs et de 0.13 % ±0.07 pour HfO2 (T= 250℃)/InAs. Des mesures similaires ont été effectuées avec des températures de dépôt de 100℃ pour le HfO2 et donnent une contraction d'environ 0.26 %. Ces valeurs de déformation ne sont pas du tout négligeables et affectent les propriétés de transport. Pour nous en convaincre, le laboratoire (Y.M. Niquet dans le cadre du projet Européen NODE) a étudié des structures coeur coquille dont les conditions aux limites du problème d'élasticité sont mieux définies : *i.e.* des structures coeur/coquilles radiales en épitaxie cohérente InAs/InP. Ces calculs atomistiques et de structure électronique avec des liaisons fortes ont montrés que dans ce cas aussi, la déformation dans le plan était un ordre de grandeur plus faible que celle hors du plan. Cette déformation a pour conséquence d'augmenter la mobilité des trous par un facteur deux si le rayon de la coquille est suffisant grand (voir les rapports publics de NODE). Le problème élastique mesuré dans cette expérience est plus complexe avec la couche intermédiaire d'oxyde et la couche de Cr nanocristallisé, mais il obéit aux mêmes tendances.

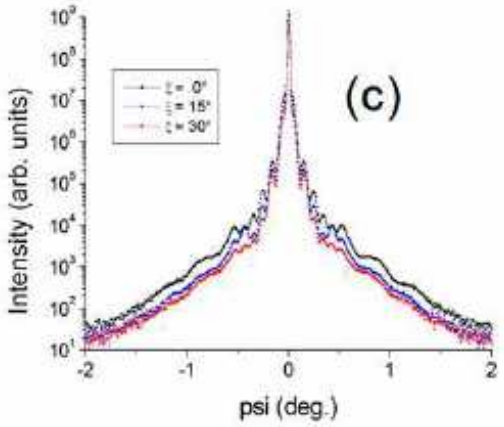

*Figure 5 : Mesures aux petits angles (pour des incidences etémergences de 0.27°) pour plusieurs orientations (*psi= *0 est perpendiculaire aux facettes de la forme hexagonale de l'échantillon) d'un dépôt de Cr sur coquille HfO_2 autour d'un nanofil nu (croissance 250℃).*

Cette expérience a aussi fait l'objet de **mesures aux petits angles** (version dégradée du GISAXS de SUV) comme le montre la Figure 5. Ces mesures nous permettent de confirmer la forme générale des nanofils, à savoir hexagonale au départ, puis de voir une modification avec les dépôts de coquilles successives. L'analyse sera conduite avec le programme IsGISAXS pour extraire les différentes épaisseurs de dépôt. La structure avec le Cr sera la plus complexe à analyser.

Enfin, des **mesures de réflectivité** ont également été effectuées sur tous ces échantillons. La densité des fils étant faible, on a encore suffisamment de réflectivité spéculaire pour extraire

l'épaisseur des dépôts bidimensionnels réalisés sur le substrat. La comparaison entre les épaisseurs radiales sur les fils et les épaisseurs 2D sera très intéressante pour estimer la sélectivité de la croissance sur le fil.

Conclusions générales:

- L'expérience s'est très bien déroulée et a donnée de nombreux résultats qui sont en cours de rédaction pour publication. Une suite sera demandée.
- Le dépôt de Cr contracte d'une façon significative le fil le long de son axe de croissance. Ce niveau de déformation doit être étudié en détail pour comprendre son impact sur les propriétés de transport.
- Les déformations dans le plan (radiales) sont beaucoup plus faibles, comme on peut l'expliquer par des calculs de déformation continue. Nous observons un élargissement des pics probablement du à l'hétérogénéité de contrainte du Cr.
- La diffusion aux petits angles et la réflectivité spéculaire ont été utilise pour accéder à la géométrie des fils et des dépôts planaires.

III. 3. Résumés scientifiques GMT

DNA Organization in a neutral lamellar: a supported film experiment.

L. Navailles, F. Nallet, E. Grelet, E. Andreoli de Oliveira **FR-32-02-655**
C.R.P.P CNRS/ Université Bordeaux/ Universidad da Sao Paulo (Brazil)

Gene therapy is a very promising technique which consists in introducing a nucleotide sequence (DNA) into the cell nuclei that will control the expression of a given gene. A strategy must be envisioned to deliver the genetic material into the nucleus, since the DNA does not do it naturally. During the last decade, different approaches to the elaboration of synthetic vectors have been tried, e.g. cationic phospholipids (CL). Some of them have been successful for *in vitro* applications; however the transposition to *in vivo* applications has not yielded the same performance. It has been shown that such DNA-CL systems have an ordered liquid crystal structure due to electrostatic interactions between the negatively charged DNA and the cationic membrane. For such formulations, although the encapsulation ratio is high, the main problem is toxicity due to the cationic behavior.

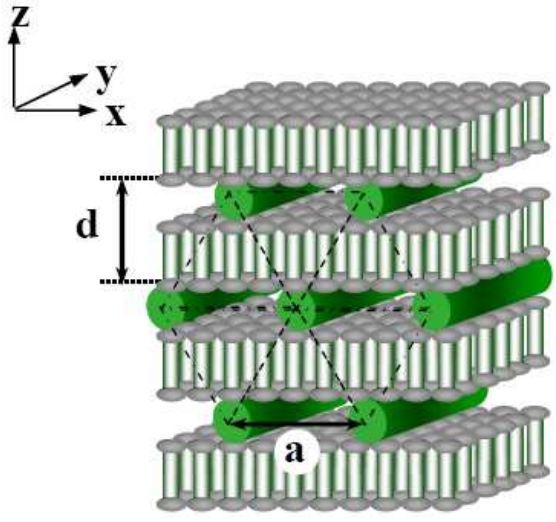

DNA hexagonal lattice in lamellar phase

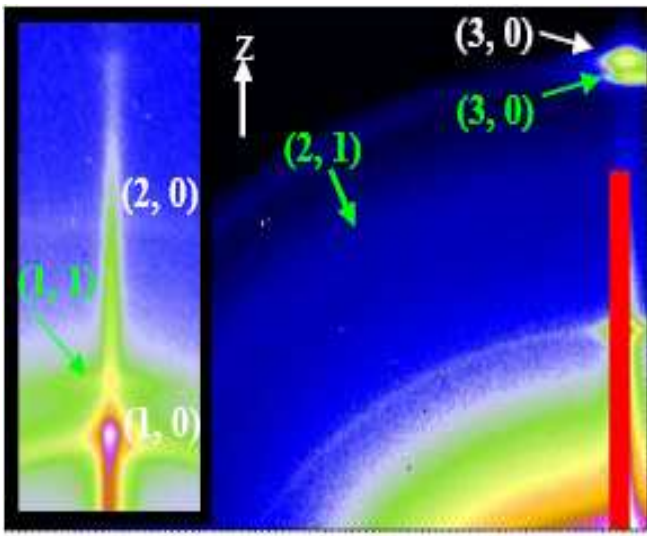

Figure 2(a) and (b): parts of GISAXS patterns showing superstructure Bragg reflections of DNA (green) and lamellar phase (white).

Recently, we have demonstrated that a large amount of DNA can be incorporated in lamellar phase of neutral lipids, with the DNA intercalated between the lipid lamellae. In particular, it was shown that multilamellar vesicles in a close-packed structure can be obtained as a result of a

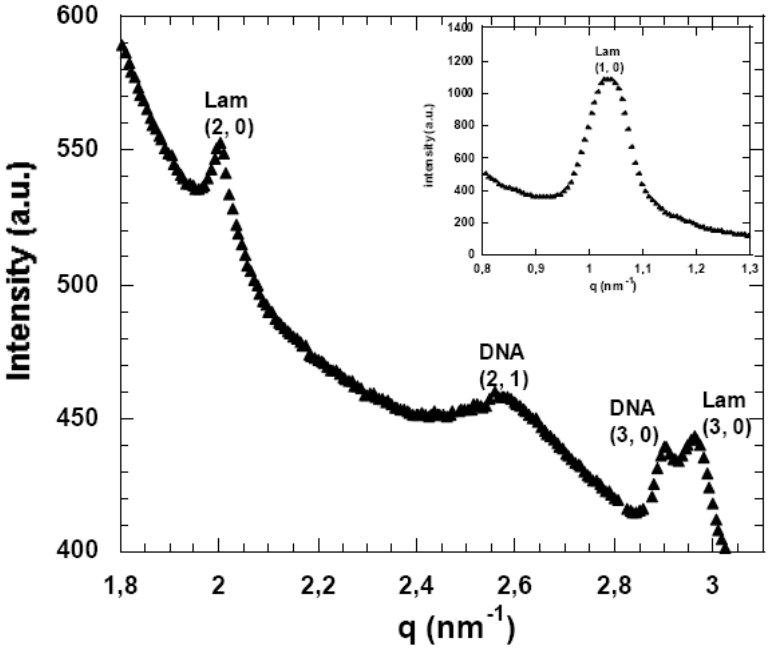

Azimuthally-averaged intensity for figure 2a as a function of the scattering wave vector.

hydrodynamic instability specific to L_α phases. The vesicles, obtained by shear, are called onions or spherulites, and consist of regularly stacked membranes. In a second step, biological molecules can be attached to the neutral surfaces of the onions to interact with a specific protein in the cell surface. Using the neutral lipid system seems to be a very promising strategy in order to obtain **non-cationic and non-viral DNA vector.** A theoretical model, based on the Flory model, has been proposed to explain the ternary phase diagram observed for the DNA-neutral lipid-water system considering mainly steric (excluded volume) interactions.

The aim of the present experiment was to obtain new information about the structure of the DNA/neutral lipid/water system. In particular, we planned to monitor the DNA-DNA correlation peak as a function of the water concentration. **Using well oriented samples** of freely suspended films, we expected to obtain—for the first time—the complete structure of our system including layer-to-layer correlations, 2D or 3D organization, and evidence DNA phase transition.

X-ray scattering experiments were performed on the BM32 beam line at the European Synchrotron Radiation Facility (ESRF). We worked with the selected energy of 12 keV, corresponding to a wavelength of λ=1.0332Å. The final beam size was $50 \times 500\ \mu m2$ (V × H) at sample position, hence fixing the vertical resolution in reciprocal space to 2.6 x 10^{-3} $Å^{-1}$. The scattered X-rays were recorded either on a low background scintillation detector (NaI) located at about 600 mm from the sample, or on a 2D CCD array detector (Princeton 1242*1152 pixels). In order to optimize the accessible domain of wave vectors, the sample-to-detector distance has been fixed to 1138 mm when using the CCD detector. Only 1/4 of the surface of the detector was irradiated. In order to check the film orientation, we made reflectivity scans with the NaI detector. A special humidity control chamber designed at Centre de Recherche Paul-Pascal for free standing films [relative humidity (rH) +/- 1%] was mounted on the goniometer. Two different geometries were used: freely suspended films and open supported films. The size of the film was 10 x 2 mm^2 and 10 x 30 mm^2 respectively. For both geometries, the chamber was oriented with the bilayer plane parallel to the x-ray beam, along the y axis.

The various samples were prepared and controlled at CRPP before the run. We drew films using samples at different compositions. We finally extensively studied 4 suspended films with a lamellar phase without DNA (45% of water or more) and 3 open supported films with weight % lipid / weight % DNA = 2.

In addition to humidity calibration, the experimental procedure was to draw a film with the neutral lipid / DNA / Water system. Figure 2-a is an example of the images obtained in the reflectivity geometry, while figure 2-b displays the azimuthally-averaged intensity of the same image as a function of the scattering wave vector. We clearly distinguish the second and third order for the lamellar phase. The signal is clearly anisotropic with the Bragg peak reflections on the vertical axis, proof of a very well oriented sample, as expected from a supported film.

The data shows the two harmonics of the lamellar scattering at q_{20} = 2 nm^{-1} and q_{30} = 2.96 nm^{-1}, which corresponds to a first order peak (inset of figure 2b) of q_{10} = 1.04 nm^{-1}, very close to q_{20}

/ 2. The associated spacing is d = 6.28 nm^{-1}, consistent with the thickness of the lipid bilayer (δ = 3.7 nm^{-1}) plus a hydrated DNA diameter (2 nm). After a beam stop translation (inset of figure 2a and 2b) we were indeed able to visualise the first order peak (q_{10} = 1.04 nm^{-1}) of the lamellar structure. In a more spectacular way, three additional peaks are observed on these images and cannot be attributed to the lamellar structure. These additional reflections cannot be explained either by an in-plane positional correlation of an intercalated DNA rod lattice, a centered rectangular columnar DNA lattice or an inverted hexagonal phase as described in detail in the literature for cationic systems.

The peak positions can be indexed to a 2D, hexagonal DNA lattice with $q_{hk} = \sqrt{h^2 + k^2 + hk}$ inside the lamellar neutral lipid phase as shown in figure 3.

The three DNA scattering peaks are indexed (1,1), (2,1) and (3,0) respectively. For the 2D hexagonal phase of the DNA/water system, the systematic absence of the (2,0) reflection, which is normally observed for such a lattice, could be due to the form factor.

As expected for an oriented hexagonal lattice with the DNA long axes parallel to y, the (1,1) and (2,1) reflections are off the z axis. For a perfectly oriented sample (as shown in figure 1) the (1,1) reflection (6 positions allowed) is expected to be +/-30 deg with respect to the z axis and the (2,1) reflection (more intense with 12 positions allowed) will appear in the reciprocal space for +/-11 deg with respect to the z axis modulo 60 deg. In the other case, an oriented sample with the DNA long axis perfectly oriented along **x** will only show the (1,0) and (3,0) reflections along z. Our data seems to indicate a DNA orientation degeneracy in the xy plane since the (1,1) and (2,1) reflections appear at 18 and 36 deg with respect to the z axis respectively.

With this experiment, we got new information about the structure of the DNA/neutral lipid/water system. Most importantly, we obtain for the first time a hexagonal DNA organization in a neutral lamellar phase. This new phase has been found in a very concentrated system—that is to say with a small amount of water. To our knowledge, this new phase has not yet been described in the literature for any cationic system. Indeed, the cationic vectors are obtained by mixing together the constituents in a one pot process. In contrast, we obtain directly a DNA condensation by controlling the concentration and the mixing protocol in a lamellar phase of phospholipids. With this new kind of DNA organization, the neutral (i.e. non-toxic) lipid system shows once again all its originality and seems to be an excellent alternative to the cationic systems for non-viral vectors.

Using a home-made special chamber designed for humidity control, we obtained oriented samples with supported films. This geometry allows the accurate description of the DNA orientation with respect to the lipid bilayer. Our data demonstrate degeneracy for the DNA orientation in the (xy) plane. High resolution is crucial in order to allow an accurate measurement of the scattering wave vectors: the reflections on the z axis for the DNA and for the lipids signals are very close. The use of the BM32 beam line was crucial for this experiment in order to obtain sufficiently high instrumental resolution, maximum intensity and 2D detection. The relatively long experiment time of 18 shifts was essential to be able to prepare the films, to change slowly and continuously the relative humidity and to wait for the equilibrium. Following the success of the experiment, a publication is currently in preparation.

Evolution de l'état de contrainte dans la cémentite de l'acier de cuve 16MND5 au cours d'essais de traction à basse température (-150℃)

R. Pesci, M. Wary, D. Bouscaud **FR 32-02-686**
ENSAM/LPMM Metz

Alors que le remplacement de la plupart des réacteurs nucléaires est prévu aux alentours de 2010-2015 (durée maximale d'exploitation atteinte), les aciers de cuve représentent un enjeu important, car se pose aujourd'hui la question de l'augmentation de leur durée de vie ou leur remplacement par de nouveaux matériaux. De vastes programmes de recherche expérimentaux et numériques ont donc été lancés (en particulier par EDF et le CEA), afin d'analyser et de prédire le comportement et les mécanismes de rupture de l'acier 16MND5 (notamment à basses températures, caractéristiques d'un refroidissement brutal du réacteur ou de la perte de réfrigérant

primaire, car sous l'effet de l'irradiation, sa courbe de résilience est décalée vers les hautes températures) : ces derniers dépendent en particulier de la distribution des contraintes par phase, car la ferrite et la cémentite - respectivement phase molle et phase dure - n'ayant pas les mêmes propriétés mécaniques, elles ne vont pas se comporter de la même façon. Cela passe par une approche multi-échelles sur laquelle repose une meilleure identification de la microstructure et des sites d'amorçage des fissures, la détermination de contraintes critiques, et que ce soit dans la caractérisation expérimentale ou la modélisation. Grâce à des manipulations « in-situ » novatrices, il a été possible d'identifier les mécanismes physiques d'endommagement de cet acier et de déterminer par DRX les états de contrainte dans la phase ferritique qui y sont associés ; la faible fraction volumique de cémentite (1 à 2%) rend en revanche impossible toute mesure directe dans cette phase (aucun pic « exploitable »). Il faut donc un flux de rayons X beaucoup plus important pour parvenir à exploiter les pics de diffraction associés à la cémentite : c'est pourquoi le seul outil, la seule technique qui permette d'envisager ce type d'essais est le rayonnement synchrotron. Son utilisation étant cependant « limitée », de nombreux modèles numériques très performants ont été développés, capables de reproduire correctement l'influence de la température constatée expérimentalement, et de prédire par conséquent le comportement de l'acier 16MND5.
Qu'ils soient de type Mori-Tanaka ou autocohérent, qu'ils prennent en compte la taille de grain ou utilisent le calcul par éléments finis, tous ces modèles prédisent que l'état de contrainte dans la cémentite à basse température peut atteindre des valeurs proches de 3500-4000MPa (figure 1), voire plus : ces valeurs peuvent se justifier assez facilement, puisqu'une simple loi des mélanges utilisée au cours du chargement permet d'envisager les mêmes niveaux de contrainte (fraction volumique de cémentite estimée entre 1 et 2%).
Or, aujourd'hui beaucoup de personnes se demandent s'il est réaliste de penser que cette phase peut effectivement supporter de tels chargements. C'est pourquoi nous avons essayé « lever cette indétermination », pour valider définitivement les différents modèles développés, car la question de la distribution des contraintes est fondamentale : elle conditionne tout le comportement de cet acier et les « prédictions » qui en découlent (tenue en service des composants, durée de vie en fatigue, contrainte maximale ou à rupture…).

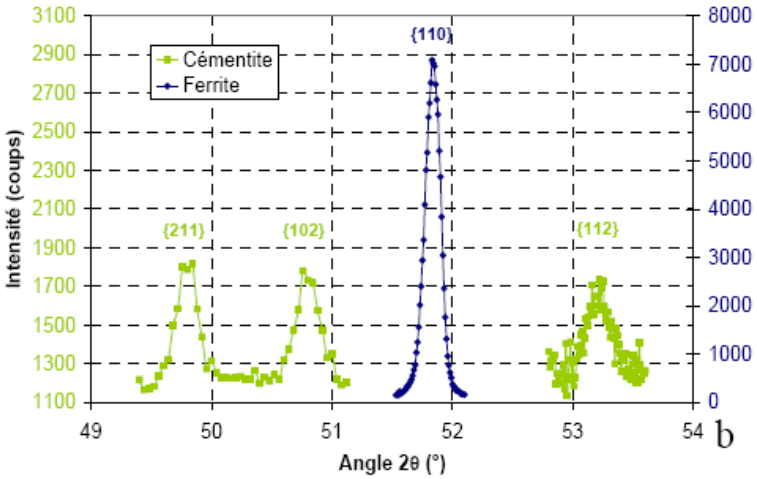

Balayage en 2θ: pics de cémentite et ferrite

La géométrie de la machine de traction (éprouvette plus basse que certaines parties de la machine) combinée aux mouvements du goniomètre présent sur BM32 ne permettaient pas des analyses à des angles ψ suffisamment élevés et variés. En outre, la présence éventuelle d'une texture dans la cémentite était inconnue.
Les éprouvettes ont donc été chargées ex-situ à froid jusqu'à la contrainte maximale, puis la contrainte dans la cémentite a été déterminée après décharge, afin de conforter la validité de nos mesures (angles ψ compris entre 0° et 70° dans ce cas).
Les mesures ont été réalisées juste en dessous du seuil d'absorption du fer, à une énergie de 7keV. Après un balayage en 2θ, les plans {211} de la cémentite ont été choisis, car ils présentaient le meilleur compromis « pic de diffraction intense/temps d'acquisition raisonnable et angle 2θ le plus élevé possible » (figure 2b) ; les utilisateurs ont également décidé d'acquérir systématiquement les
pics {110} de la ferrite (temps de comptage beaucoup plus faible), afin d'avoir une idée de l'état de contrainte dans cette phase et un point de comparaison avec les analyses in situ réalisées au préalable par « DRX conventionnelle » dans cette même phase.
Les analyses de contrainte ont donc été réalisées dans la ferrite et la cémentite après décharge, et les écarts de contrainte constatés entre ces deux phases et la contrainte macroscopique ont ensuite été

reportés au dernier point de charge (figure 3). Les résultats montrent que la contrainte dans la ferrite reste proche de la contrainte macroscopique, avec un écart qui ne dépasse pas 120MPa +/- 40MPa, ce qui est tout à fait comparable à ce qui a été déterminé auparavant par DRX. La cémentite, elle, est beaucoup plus chargée, puisqu'elle atteint des valeurs de contrainte proches de 2200MPa, avec une erreur estimée toutefois à +/- 300MPa : cette valeur de 2200MPa est bien plus faible que celle prédite par les différents modèles, qui l'estiment supérieure à 6000MPa si l'on considère une fraction volumique de cémentite de 1,2% (fraction volumique déterminée par diffraction en dispersion d'énergie ; une deuxième estimation par diffraction des neutrons est également en cours).
Ces expériences nous ont donc permis d'estimer la contrainte maximale que peut atteindre la cémentite au cours d'un chargement à -196℃ : *2500MPa*. Toutefois, l'objectif initial étant la détermination in situ de l'évolution de la contrainte dans la cémentite de l'acier de cuve 16MND5 à -150℃ (premiers essais de traction in situ de leur genre), des analyses complémentaires vont être demandées par l'intermédiaire d'une nouvelle proposition d'expérience. Pour cela, nous envisageons d'installer un berceau d'Euler supplémentaire sur la ligne BM32 et nous allons construire une nouvelle petite machine de traction capable de solliciter les éprouvettes à sa surface (donc permettant des analyses de contrainte in situ « sans obstacle », à tous les angles ψ): cette dernière spécificité étant visiblement très recherchée - notamment au sein de l'ESRF -, des discussions ont déjà eu lieu avec des responsables d'ID15, afin que sa réalisation se fasse conjointement.

Size and structure dependence of the catalytic activity of supported gold nanoparticles for CO oxidation 32-02-688

M.C. St-Lager, R. Lazzari, P. Dolle, S. Garaudee, M. Mantilla, J. Jupille,H. Cruegel,I. Laoufi
CNRS- Institut Néel Grenoble/ Institut des Nanosciences Paris

In the previous experiments, equivalent gold thickness between 0.4 to 3 gold monolayers (ML), were explored (RE n° SI1459, n° 32 02 648 and ref [1]). The quantitative analysis of the GISAXS pattern was performed using the dedicated *IsGISAXS* software. The growth was found 3D and the particles were best modeled by a truncated sphere. The size of the nanoparticles, in UHV, ranged from 2 to 5 nm. The reaction rate per Au atom measured at 470 K was seen to increase as the cluster size decreases. Particles of size lower than 3 nm were stable under oxygen but sintering occurs when CO is added at 470K. That dimension coincides with the switch which was previously observed from nucleation-growth, with particles pinned on defects, to coalescence where particles become independent of defects. However we did not succeed to simultaneously measure the

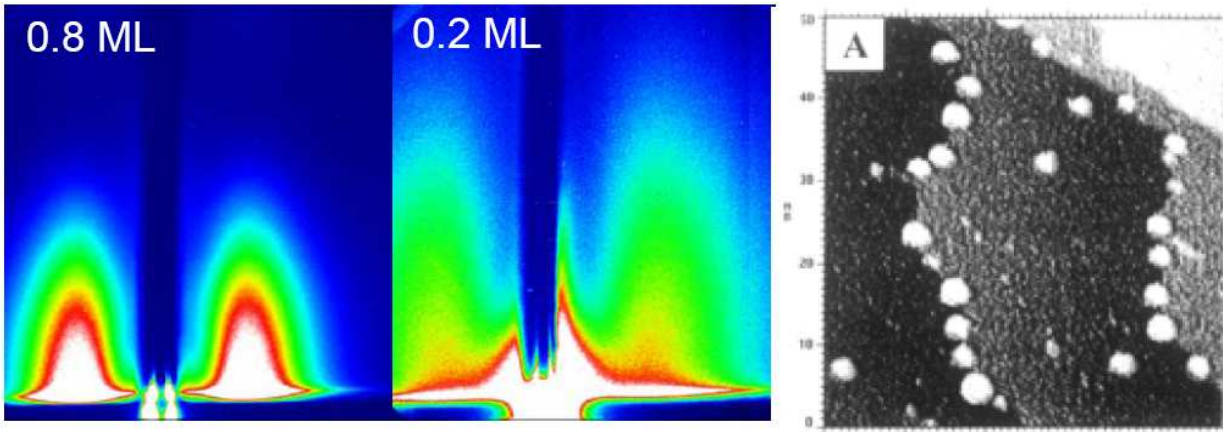

Figure 1 : Grazing incidence Small X-ray Pattern of 0.8 and 0.2 Au monolayers deposited on rutile (left) forming nanoparticles as shown on STM image (right).

activity and the size of the clusters by GISAXS. The link between them was obtained by complementary experiment at the laboratory. During the June campaign at ESRF on BM32, we succeeded to do simultaneously such measurements; moreover we also performed GIXS (or Surface X-ray diffraction) and get the structure and the lattice parameter in the gold nanoparticles.

We extend our study to smaller coverage, down to 0.1 ML. Figure 1 shows examples of collected GISAXS patterns. For coverage, higher than 0.4 gold ML, there is one correlation peak on each side of the beam shutter footprint (which masks the reflected beam). In that case the interparticles spacing is centered around one value. In the case of thinner coverage, as illustrated for 0.2ML, there are two correlation peaks which correspond to two distances (one being close to the beamshuter). This is consistent with STM images (see right hand of figure 1), recorded for similar coverage, that shows clusters localized along the step of the substrate terraces, with two mains distances: along the step and perpendicularly.

As previously, we observed, that under exposure to millibars of the reactive gas, particles were stable for equivalent coverage thicker than 1 ML, even under the reactive mixture O_2+CO at 470K.

This 1 ML corresponds to particles with 3 nm size. Below they are instable and sintering occurred. Data were collected under CO and O_2 alone, and CO+O_2 at several temperatures in order to understand the sintering driving force, especially to determine the role of the increase of the local temperature due to the exothermic conversion of CO into CO_2. The analysis is presently under progress.

Whatever the gold coverage thickness, we were able to measure at 470K the CO conversion into CO_2 even for 0.1 ML. Figure 2 shows the rate per Au atom as a function of the deposited quantity. The results, obtained during the preparation at the laboratory follow the same variation as this found at ESRF during x-ray measurements, with a maximum for around 0.2ML. On figure 3, the rate (green curve) is plotted with nanoparticles parameters, as deduced by GIXS performed in the same time as the reactivity: diameter (horizontal axis), cluster height (red curve with the right hand vertical axis) and gold nanoparticles lattice parameter (black curve with the left hand vertical axis).

The ESRF experiments being recent, the whole analysis is not complete, but first very important conclusions can be already drawn:

- The rate of CO conversion into CO_2 presents a maximum around 2.5 – 3 nm
- At the maximum, the particles clearly kept a 3D-character with at least 6-7 atoms-heights.
- A significant lattice contraction is evidenced.

The rate variation confirms the maximum in turnover frequency (TOF) observed by Valden *et al* [4] but it discards the metal non-metal transition (quantum size effect) as suggested by these authors.

On the other side it seems to be contradictory to models that attribute the activity to the increase of low coordinated sites concentration when decreasing the size, with no maximum. However, previous work shows that surface activity diminishes with a lattice contraction.

The open questions are thus: Is the measured lattice contraction enough to explain the observed drop of the activity for the smaller sizes? Does the substrate reducibility play a role or not in the behaviour of the activity versus size curve?

Grain Orientation and Full Strain/Stress Tensors Mapping in He Implanted UO2 Nuclear Fuel Using µ-Laue Diffraction

H. Palancher, P. Martin **ESRF MA 452**
CEA-Cadarache/Dir. Energie Nucléaire

This work is part of the PRECCI project (CEA, EDF) dedicated to the study of nuclear fuel (UO2) microstructure evolutions in conditions of long term and interim storage. In that framework, one of the main issue is related to the behaviour of the significant quantity of the helium produced by the actinides alpha decay in the UO2 pellets. The main aim of this work was to derive mechanical data from He implanted UO2 polycristalline disks.

After anneling of He implanted UO2 polycristalline disks (9 µm in diameter), it has been recently shown by nuclear reaction analysis at the micrometer scale (µ-NRA) that [1]:

- grain boundaries act as short cuts for He diffusion,
- He diffusion is furthermore significantly enhanced in the vicinity of grain boundaries from a temperature of 900℃.

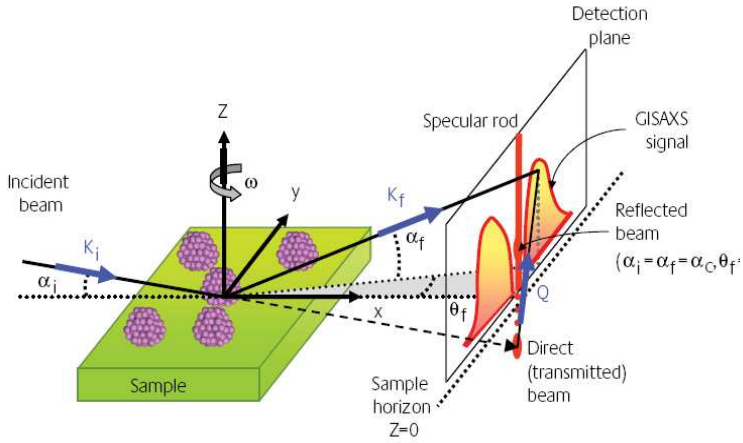

Experimental scattering geometry for GISAXS.

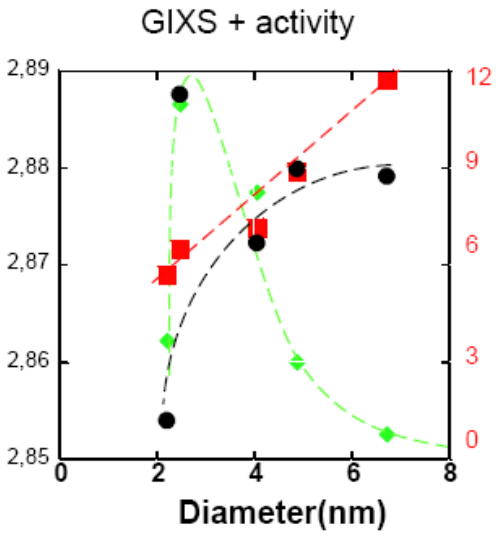

Figure 3: (left & black) d_{Au-Au} in Å and (right & red) Au nanoparticles height (in number of atomic plane)

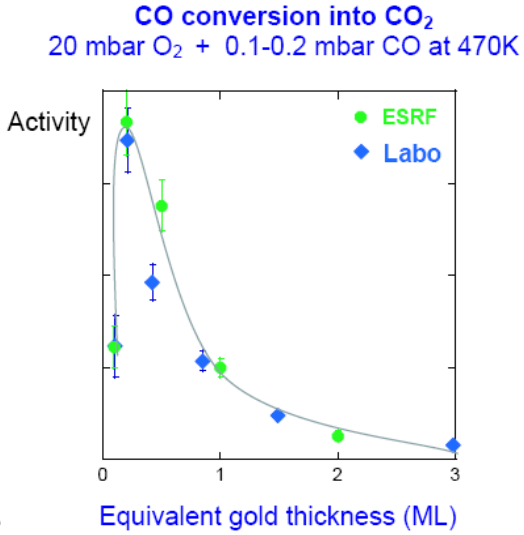

Figure 2:

The main aim of this work was to characterize the full strain/stress tensors in the UO2 in the centre of the grain and at its periphery. In that view, 2D mapping using micro-focused Laue X-ray diffraction measurements were required since this technique enables the localization of grain boundaries and also the determination of the strain/stress tensor.

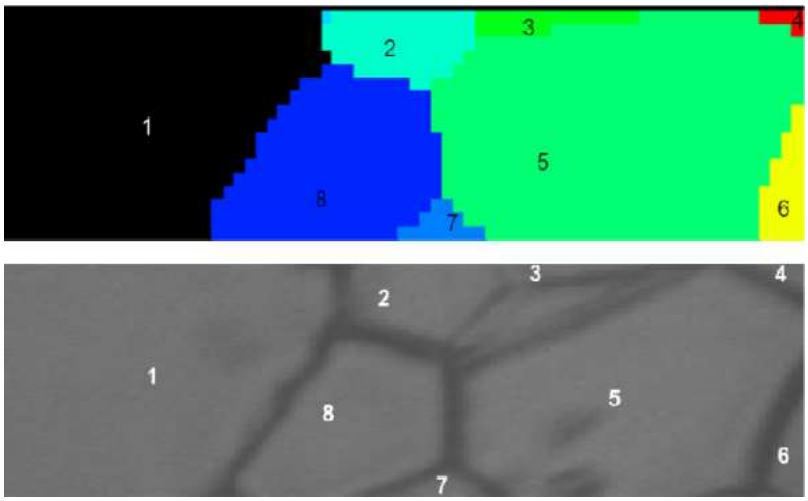

Fig. 2: Grain orientation map compared with an optical micrograph of the same UO2 polycristalline sample (He implantation followed by a 1 hour annealing at 1000℃). Numbers written on t he grains help for comparison.

The samples of interest were UO2 sintered polycristalline disks, the average grain size being around 9 µm. He (500 keV) implantations and annealings were performed at the CEMHTI laboratory. Three kinds of samples have been analyzed during this experiment: (1) non-implanted

(fresh) samples (mono and polycristals), (2) as He implanted samples, (3) He implanted and subsequently annealed samples. Based on µ-NRA results, two kinds of annealing conditions were selected:
- in the first no He depleted zone had been observed at grain boundaries (typically 1 to 4 hours at 800℃),
- in the second thick depleted zone were evidenced: this is the case for temperatures higher than 900℃ and short durations.
The influence of sample preparation on the stress/strain in these three kinds of samples has also been evaluated. 12 samples have thus been characterized. They were conditioned under kapton tape for safety reasons.
The conventional set-up of BM32 set-up for µ- focused X-ray diffraction in Laue mode has been used. The size of the pink X-ray beam has been reduced down to about 1×2 µm² (H×V). To be more sensitive to the He
implanted volume in the sample which is located at 1.0±0.5 µm under the sample surface, the energy range of the X-ray pink beam has been restricted: at the beginning the natural range was used (5-28 keV) and successive limitations were performed first at 16 keV and then at 13 keV. This energy range reduction does not affect significantly the accuracy of the calculated mechanical data: the number of Bragg peaks measured
on the CCD camera remains large enough for good statistic. On the UO2 single crystal used as reference, 21 Bragg peaks have been found with the 5-13keV energy range (cf. Fig.1). At 13keV, X-ray penetration depth into UO2 was about 7 µm (IR/I0=10%).
During this expriment, 2D µ-XRD mapping has only been performed using a pink X-ray beam; for this reason only the deviatoric part of the strain tensor could be determined. Preliminary analysis of these data shows that whatever the sample preparation methodology, only as-implanted samples present a streaking of Bragg peaks (espacially those measured at high 2q angles). This streaking is directed towards the center of the camera. For annealed samples this streaking has not been observed demonstrating that only elastic deformations remain. To illustrate the strong deformations in UO2 caused by He implantation, it must be added that average von Misès stress in the as implanted samples is close to 1000 MPa whereas this value reaches only 100-200 MPa in fresh polycristalline UO2 disks. This stress in the as-implanted samples has been obtained by taking into

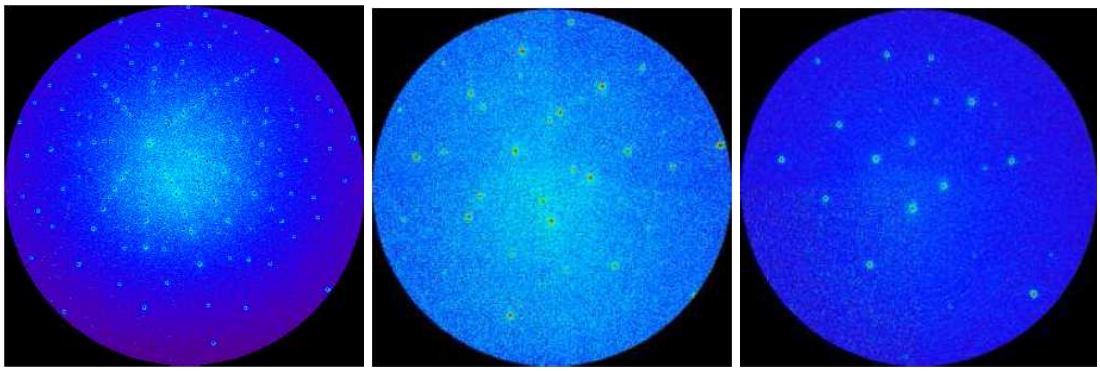

Influence of the energy range of the X-ray beam on the number of peaks measured on the same UO2 single crystal. From left to right: 5-28keV (129 peaks found), 5-16keV (43), 5-13keV (21 peaks found).

account only the corresponding Bragg peak part .

Conclusions:
In this first experiment, the interest of Laue diffraction using micro-focused X-ray beams for strain/stress study in polycristalline He implanted UO2 has been demonstrated. Specificities of the UO2 matrix have been
overcome. Further calculations are ongoing to characterize quantitatevely the stress gradients along the grains after the different annealing treatments to establish definetly whether this variation may be correalated with the He depletion.
On each of the 12 polycristalline samples, a 58×30 µm² µ-XRD mapping (H×V) has been carried out using this last energy range (5-13keV). XRD Laue images were analyzed with the Xmas software package. If only the most intense Bragg peaks are considered, the automatic indexation procedure leads to grain orientation maps in excellent agreement with optical micrographs (cf. Fig.

2). However, it must stressed that despite the band pass reduction of the X-ray beam energy, a very large amount of Bragg peaks can be found on all images collected on polycristalline samples: about 200 peaks are identified that correspond to an unexpected high number of grains (10 grains defined by more than 10 Bragg peaks). It is very difficult to interpret those results by just comparing the measured size of the X-ray beam (2×1μm²), the crystallite size (6 to 9 μm diameter) and the X-ray penetration depth into the matrix (7μm). Most probable hypothesis at this step is that the conventional method for defining the X-ray beam size which is based on the full width at half maximum, is not relevant when dealing with the characterization of a matrix containing heavy scatterers like U (Z=92e-). In this case, the X-ray beam appears to be larger.

III. 4. Autres expériences menées en 2007-2008 sur GMT

X-ray microdiffraction on a single-crystalline copper micro-tensile specimen
J. Keckes, O. Thomas, C. Kirchlechner, N. Vaxelaire, K. Martinschitz **ESRF MA 451**
Universität Leoben/ E. Schmid Insitute of Materials Science (Austria)/ CNRS –Université Marseille IM2NP

Stress tensor determination and crystal orientation evolution during uniaxial loading of a copper bicrystal
T Hoc et al. **ESRF MA 555**
Ecole Centrale Paris

Grain growth during annealing of sub-micron copper lines used for interconnections
S. Labat, B. Kaouache, O. Sicardy, O. Thomas **FR 32-02-676**
CNRS-IM2NP Marseilles/CEA-Grenoble-LITEN

Commensurate - incommensurate phase transition in chiral liquid crystals investigated by resonant scattering of x-rays
P. Barois et al **ESRF SC 2457**
C.R.P.P. CNRS/Université Bordeaux

Analyse de coupes stratigraphiques de peintures de chevalet par micro-diffraction de Laue.
E. Dooryhee, P. Martinetto, C. Dejoie, E. Wellcomme, J.L. Hodeau **FR 32-02-681**
Institut Néel, CNRS Grenoble/ LRMF CNRS Paris

Thin film delamination study during in situ compressive testing by Scanning micro X-ray Diffraction
P. Goudeau, G. Geandier **FR 32-3-687**
LMP, UMR 6630 CNRS - Poitiers

III. 5. Développement de l'analyse de la microdiffraction

Contexte et objectifs :

Depuis deux ans nous développons un code d'analyse et de traitement des données de microdiffraction adapté aux images collectées sur la ligne BM32 et dans le but de répondre rapidement aux demandes des utilisateurs pour des besoins et des outils spécifiques. Il s'agit à terme de disposer d'un outil comparable à celui développé par N. Tamura (ALS, berkeley). Nos motivations nous poussent à réaliser un logiciel ouvert, flexible, modifiable, évolutif permettant ainsi :

- d'accueillir facilement de nouvelles fonctionnalités
- d'améliorer notamment les performances de calculs en terme de rapidité (cf. analyse en vol à l'image de ce qui se fait en Electron Back Scattering Diffraction (EBSD))
- de donner la possibilité à une communauté de contrôler *toutes* les étapes de l'analyses et les modèles théoriques employés.
-

Nous avons choisi un développement en langage python (OpenSource) qui facilite le développement d'un code scientifique et de prototype logiciel. Il bénéficie d'accès simple à des bibliothèques graphiques et de calculs rapides (C, Fortran). L'avantage de ce choix est qu'il l'offre la possibilité aux utilisateurs d'analyser les données à l'aide d'une interface graphique ou par le biais de commandes (mode intéractif ou sous forme de macros).

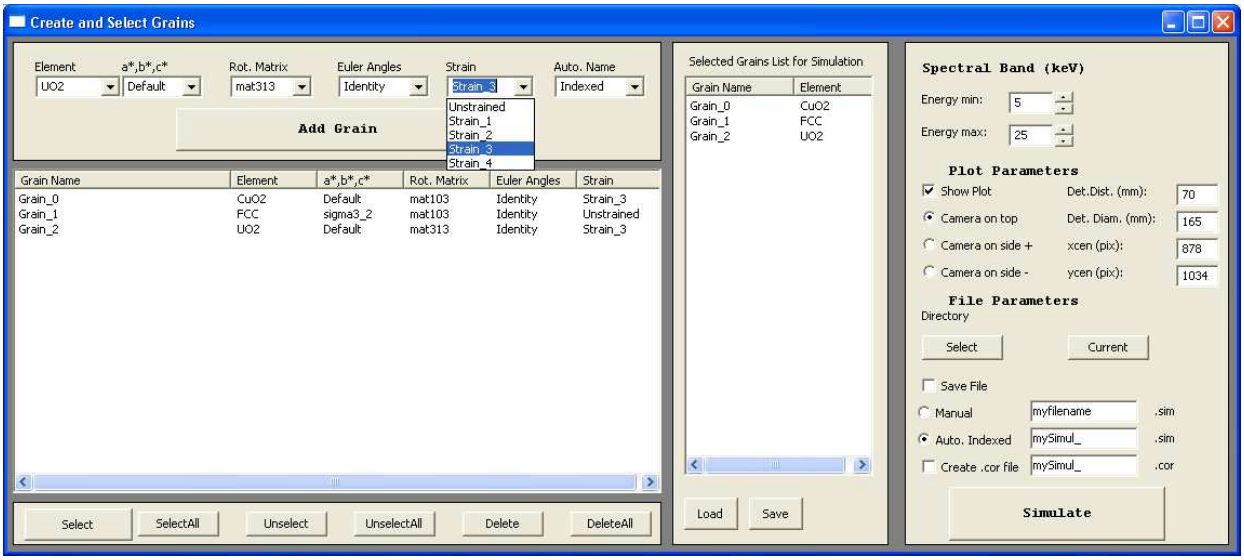

Interface graphique de simulation de diagramme de Laue de polycristaux.

Le développement de ce logiciel s'inscrit aussi dans une démarche générale à l'ESRF (l' « upgrade » de l'ESRF comporte un volet de traitement de données) d'analyse des données toujours plus volumineuse et orientées vers le traitement en ligne. Certaines méthodes développées ici peuvent être adaptée pour d'autres techniques de caractérisation à l'aide de rayons X ou non (diffraction neutron, microscopie électronique, kossel)

Le traitement des données issues des mesures de microdiffraction comporte les étapes essentielles suivantes: 1) recherche et mesure des angles de diffraction 2) la calibration du détecteur 3) l'indexation et 4) détermination des déformations/contraintes 5) la cartographie automatique.

Cette année, une interface graphique à été réalisée permettant à l'utilisateur d'indéxer manuellement les images. Il peut au préalable déterminer les paramètres (et d'en apprécier les effets) en vue d'une indexation automatique. En plus de sa transparence, l'indexation manuelle est aussi un atout (par rapport au programme XMAS) car elle permet de résoudre des cas complexes (généralement beaucoup de pics ou pics éclatés au positionnement incertain), donnant la possibilité à l'utilisateur de fixer les paramètres avant et pendant l'indéxation (resp. choix du jeu de pics et seuils de décision).

Au bout de deux ans de fonctionnement de l'instrument et d'écriture de méthodes d'analyses, nous pouvons dégager les besoins en fonctionnalités nécessaires et les axes de travail à suivre.

Recherche et mesure de la position des pics :
L'analyse des données repose au départ sur la mesure de la position de pics de diffraction sur le plan du détecteur 2D (image 2D intensité diffusée en fonction de x,y). La pertinence/dispersion/précision des résultats repose sur cette mesure qui correspond à l'extraction correcte des 2 angles de diffraction correspond à chaque pic. Si cette extraction est aisée pour les monocristaux, elle peut devenir difficile en raison de limitations instrumentales…:
-résolution du détecteur (pixélisation des tâches)
-statistique de comptage déterminant le nombre de pixels (émergeant du bruit) contenu dans un pic

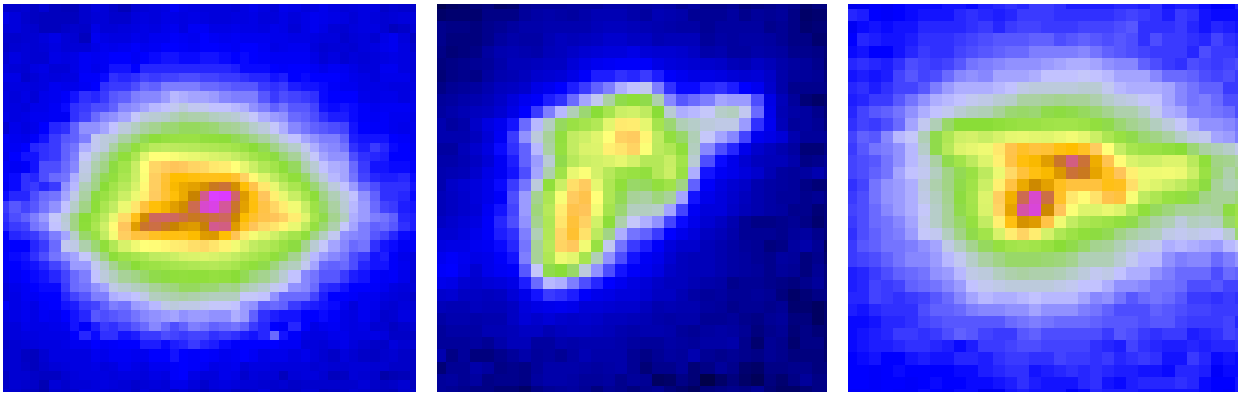

Morphologie de la réflexion de Bragg en fonction de la nature des plans réticulaires sondés pour un même grain. La détermination correcte des contraintes nécessite dans ce cas une analyse plus fine de l'origine de l'éclatement (distribution orientations et/ou déformations) afin

…mais aussi surtout celles liées au matériau étudié lui-même :

-élargissement (dans une direction seulement) due à l'épaisseur de la zone sondée
-forme non circulaire voire pic éclaté d'origines multiples: distributions de déformations et d'orientation, même dans un volume de quelques microns cube et élargissement dû à la présence de défauts (dislocation, plans de glissement, …).

Objectifs 1:

- Simuler en fonction de modèles prédéfinies ou entrés par l'utilisateur la forme des pics ou groupe de pics
- Adapter alors l'extraction de l'information contenues dans chaque pic ou groupe de pics (barycentres, largeurs,) en fonction de modèles prédéfinies ou entrés par l'utilisateur pour aider l'indexation et améliorer la précision sur la détermination des contraintes

Calibration:
Elle consiste a déterminer la relation entre tout point sur la caméra (coordonnées en pixel) et deux angles définissant une direction de diffusion (vecteur d'onde final). A partir d'un cristal de référence connu ou facilement identifiable (en général considéré comme non déformé), on cherche les 5 paramètres de la caméra minimisant les positions calculées et celles mesurées (par une méthode des moindres carrés par exemple).
Cette procédure est en cours d'achèvement. La détermination des paramètres est délicate et converge vers des solutions numériques sans réalité expérimentale si l'on part de valeurs trop éloignées de la solution. Des efforts sont donc fait actuellement pour rendre cette procédure la plus automatique possible.

Objectifs 2 :

- Prise en compte du décalage de position des pics en fonction de l'énergie (profondeur de pénétration variable)
- Localisation de la profondeur des plans diffractant à l'origine des pics (cartographie 3D), par triangulation (détecteur à plusieurs distances) par la méthode d'ombrage par un fil micrométrique mobile et absorbant.
- Auto-calibration (avec un nombre suffisant de pics, la calibration peut être effectuée à partir des pics d'un grain aux paramètres de maille inconnus).

Indexation:
Elle consiste à attribuer pour chaque pic un grain d'origine et une famille de plan réticulaire (indices de Miller (hkl)).
aLa **méthode de base** d'indexation, utilisée pour les monocristaux, consiste à choisir 2 ou 3 pics, à comparer la ou les distance(s) angulaire(s) les séparant à une table de données ; si aucunes correspondances n'est trouvée, on choisit d'autre pics, jusqu'à trouver une solution. Dans le cas de matériaux polycristallins, cette méthode peut s'éterniser et/ou par coïncidence aboutir à des résultats erronés.

Pour remédier à ces blocages, nous avons implémenter des méthodes de **présélection** d'un jeu de pics possédant une plus grande probabilité d'appartenir au même grain (par défaut sélection par ordre d'intensité des pics) :

- algorithme de recherche de « cliques » de la théorie des graphes
- reconnaissance des principales réflexions en fonction de la position caractéristique des autres réflexions au voisinage
- reconnaissance d'un axe de zone fonction de la répartition angulaire caractéristique des pics qu'il contient)

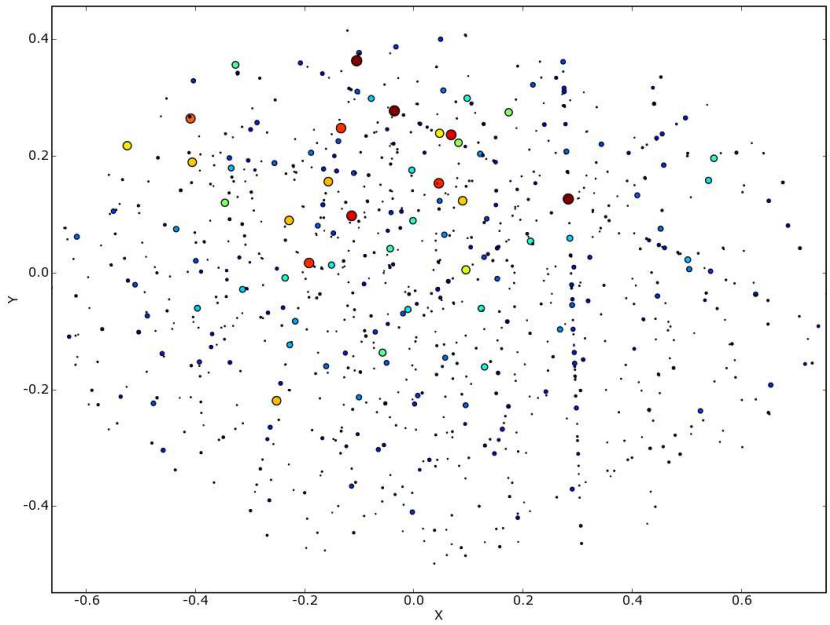

Projection gnomonique des pics révélant immédiatement la contribution d'au moins 2 grains par l'intermédiaire des axes de zones (points alignés). A l'intersection des axes de zones denses se trouvent les principales réflexions de Bragg (faible indices hkl) : on remarque un pic de symétrie 3 (111) en haut à droite. L'intensité des pics est traduite par la couleur et la taille des cercles.

Après avoir indexer tous les pics appartenant à un grain, il est souvent souhaité d'indexer les pics restant correspondant aux autres grains.

La méthode simple consiste à partir d'un jeu de pics ne contenant pas ceux déjà indéxés. Toutefois s'il existe une relation de symétrie entre les orientations de deux grains, des pics de Laue seront communs aux deux diagrammes correspondants. Dans ce cas, l'indexation du premier grain aura retiré des pics du jeu de pics pour l'indexation du second. Cette dernière peut alors ne pas aboutir ou donner une indexation partielle sujette à caution.

Pour lever toutes incertitudes et répérer les pics non communs (possédant qu'un seul triplet hkl), nous avons donc construit des outils de simulation de diagrammes de Laue afin aider et d'achever l'indexation de grains en relations de **macle**, configuration assez courante dans les matériaux étudiés sur BM32 (relaxation des contraintes après traitement thermique).

Pour éviter cette démarche séquentielle, qui peut s'avérer longue et mener à des indexations érronées des derniers grains, nous avons élaborée une méthode alternative permet de reconnaître plusieurs grains à la fois.

La réduction des données (positions des pics) dans un espace adéquat (cf. rapport au CA précédent) et leur **comparaison à une base de données** préalablement établies en échantillonnant l'espace des orientations (par pas de 1° pour l'instant), pour une structure cristallographique donnée, permet de classer plus efficacement les pics en fonction de leur grain d'origine. L'indexation des pics de plusieurs grains est alors opérée simultanément, en étant moins sensible aux bruits et coïncidences de positions. Une méthode numérique ingénieuse élaborée par E. Rauch (CNRS SIMaP/GPM2 St-Martin d'Hères) réalise la comparaison de manière très rapide (moins d'une seconde pour une base de 180 Mo).

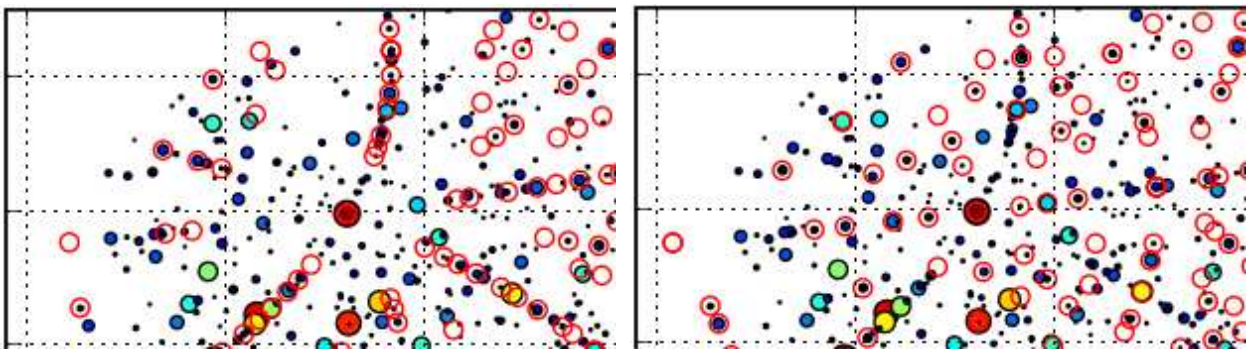

Diagramme de Laue (cercle pleins : données expérimentales, cercles vides rouges : simulation) d'un polycristal de CdTe comportant deux grains en relation de mâcle possédant des pics communs (deux indexations possibles, exemple pic central : (111) et (-511)). Pour l'analyse des déformations des 2 grains, il faut considérer seulement les pics propres à chacun des grains.

Objectifs 3:

- Mise en place de l'indexation automatique de plusieurs grains
- Introduction générale des mâcles ou d'éléments de symétrie spécifique (règles sur les indices hkl)
- Introduction générale des données matériaux (lecture d'une base)
- Utilisation d'une indexation préalable venant de l'utilisateur ou d'une image adjacente de la cartographie où l'indexation est plus aisée.
- Estimation des performances des méthodes en fonction du nombre de grains et du nombre total de pics (temps et taux de réussite d'indexation)

Détermination des déformations:

Des procédures ont déjà été écrites. Elles sont analogues à celles utilisées pour la calibration. Les premiers essais montrent que la convergence, rapide, vers une unique solution physiquement réaliste nécessite un soin particulier sur la précision des données (position des pics) et le nombre de pics impliqués lors de la méthode de minimisation.

Objectifs 4 :

- Achever l'ajustement des déformations
- Laisser le choix à l'utilisateurs du jeu de pics impliqués (nombre, principales réflexions, en fonction de l'intensité ou de l'énergie correspondante,…)
- Estimation des barres d'erreur sur les déformations/contraintes

Automatisation et cartographie :

La mise en place d'un tableau de bord pour l'automatisation de l'indexation pour une série d'images ne devrait pas poser de problèmes. La gestion du produit du l'indexation automatique, notamment la navigation à travers la base de données de résultats mérite réflexions afin de privilégier l'ergonomie et répondre avec souplesse à la diversité des demandes des utilisateurs présentes et futures.

IV Surfaces/Interfaces/Nanostructures en ultra-vide (SUV)

IV.1. Introduction

Personnel

L'équipe SUV (Surfaces Under Vacuum) est composée de deux chercheurs CEA (T. Schülli et G. Renaud), d'un ingénieur de recherche CNRS (H. Tolentino) et d'un chercheur CNRS (M.de Santis). Depuis le départ de Marion Noblet-Ducruet, le support technique sur SUV est très insuffisant. L'aide d'Olivier Geaymond et l'embauche pendant 9 mois d'un jeune technicien intérimaire ont permis de réaliser le plus gros du travail technique, mais aucune embauche stable n'a fait suite à ce contrat. L'instrument SUV, techniquement très complexe et demandant un suivi quotidien, nécessite le travail d'un technicien dédié, à plein temps. Il est donc urgent de débloquer l'embauche d'un technicien sur cet instrument.

Développements

Les développements techniques majeurs de cette année, la nouvelle tête goniométrique et les nouvelles fentes, développées au SERAS, sont présentée dans le premier chapitre de ce rapport. La nouvelle tête goniométrique a été conçue pour apporter une bien meilleure précision que la tête actuelle, indispensable pour certaines expériences. Les nouvelles fentes de définition du faisceau et de détection sont elles aussi très précises, adaptées au fonctionnement sous vide et au très faible encombrement dont nous disposons.

Faute de support technique, les travaux d'amélioration de la chambre de caractérisation et ceux du support de la chambre ont encore été décalés.

L'instrument est actuellement (fin octobre 2008) complètement démonté, et les pièces stockées en divers lieus de l'ESRF, afin de laisser le champ libre aux travaux, en-cours, d'extension de la cabane expérimentale.

Activité scientifique

Nous résumons ci-dessous les principaux résultats des expériences réalisées sur la période novembre 2007-octobre 2008. De plus en plus, les expériences demandent des mesures combinées de GISAXS et de GIXD durant la croissance. Elles montrent les limites de l'installation actuelle, et le fort intérêt d'agrandir la cabane, de façon à améliorer et les expériences de GISAXS (longueur) et celle de GIXD (détection 1D et 2D).

In 2007/2008, the trend already visible in recent years, namely the growth of complex structures and co-deposition of several materials was confirmed to dominate largely classical surface physics topics. The combination of Grazing Incidence Small Angle X-ray Scattering (GISAXS) and Diffraction (GIXD) offers ideal and almost unique possibilities to access structural parameters on a vast length scale from subatomic distances to particles of 100 nm. It is especially the opto mechanical elements inside the UHV chamber that allow for low noise GISAXS recording and the extreme versatility of the chamber to connect multiple deposition sources that make the instrument attractive to our users.

The following experimental reports and the examples of two publication highlights of the recent months underline clearly the trend of growth of complex nanostructures and the in situ tracking of their functionality.

IV. 2. SUV highlights :

Scientific Highlights in 2008: Publications on functional nanostructures
The following two publications give an example how *in situ* x-ray scattering can bridge the link between structural and functional properties of nanostructures. Catalytic nanoparticles in the first case, magnetic ones in the second case:

P. Nolte, A. Stierle, N. Y. Jin-Phillipp, N. Kasper, T. U. Schulli, H. Dosch,
"*Shape Changes of Supported Rh Nanoparticles During Oxidation and Reduction Cycles*",
Science 321, 1654 (2008).

conducting order parameters include a finite momentum –q. (D_x, D_y) is the gauge invariant gradient. Introducing the magnetic field allows one to couple M_q in linear order to preserve time-reversal symmetry. These combinations allow for a second-order phase transition within the superconducting phase and a first-order transition to the nonmagnetic normal state. For the coupling term V_2, no magnetic structure is induced for fields **H** || [100]. Given the weak dependence of the **Q** phase on the magnetic field orientation in the basal plane, our measurements suggest the presence of a V_1 or V_3 coupling term, inducing the finite-momentum even-parity Γ^+_5 state or the odd-parity Γ^-_3 state.

This Landau theory shows that incommensurate magnetic order induces a superconducting gap function that carries a finite momentum—the first experimental evidence of a superconducting condensate that carries a momentum. However, we show that this state may not arise purely from Pauli paramagnetic effects and the formation of a new pairing state between exchange-split parts of the Fermi surface, a state commonly known as the FFLO state (*16*, *17*). In the FFLO state, the

Shape Changes of Supported Rh Nanoparticles During Oxidation and Reduction Cycles

P. Nolte,[1] A. Stierle,[1]* N. Y. Jin-Phillipp,[1] N. Kasper,[1] T. U. Schulli,[2] H. Dosch[1]

The microscopic insight into how and why catalytically active nanoparticles change their shape during oxidation and reduction reactions is a pivotal challenge in the fundamental understanding of heterogeneous catalysis. We report an oxygen-induced shape transformation of rhodium nanoparticles on magnesium oxide (001) substrates that is lifted upon carbon monoxide exposure at 600 kelvin. A Wulff analysis of high-resolution in situ x-ray diffraction, combined with transmission electron microscopy, shows that this phenomenon is driven by the formation of a oxygen–rhodium–oxygen surface oxide at the rhodium nanofacets. This experimental access into the behavior of such nanoparticles during a catalytic cycle is useful for the development of improved heterogeneous catalysts.

Many industrial chemicals and fuels are synthesized with the use of heterogeneous, solid-phase catalysts that often contain metals in the form of nanoparticles (NPs). The direct study of these catalysts is challenging, and model catalysts such as single crys-

tals and vicinal surfaces have been extensively investigated and have provided important insights (*1*–*3*). The emerging challenge for fundamental research is to provide a detailed microscopic understanding of the different physical and chemical processes that take place at NPs during catalytic reactions. Although there is a consensus that NPs should exhibit enhanced catalytic activity because (i) they posses an increased number of undercoordinated atoms and (ii) different low-index facets coexist [which should facilitate mass transport and thereby lift kinetic barriers known from single crystal surfaces (*4*)], it is still an open question as to whether the metallic or the oxidized state of the particle is the catalytically more active phase [Langmuir-Hinshelwood versus Mars–van Krevelen mechanism (*5*, *6*)]. During catalytic cycling experiments, NPs undergo reversible size changes that are associated with cyclic shape changes, material redispersion, and sintering (*7*, *8*).

Among the many catalytically active metals, the 4d transition metals [Ru, Rh, Pd, and Ag (*1*)] are finding increased use in organic reactions, the synthesis of biologically active compounds under sufficiently mild conditions, and the treatment of contaminated water. Rh is a well-known catalyst for hydrocarbon and CO oxidation, as well as for NO_x reduction in three-way car catalysts (*9*). Recent experimental and theoretical studies of 4d transition metal single-crystal surfaces carried out near atmospheric pressures suggest that their catalytic activities are related to an ultrathin metal oxide film on the surface (*5*, *10*–*12*). In the case of Rh, a hexagonal O–Rh–O trilayer structure forms basically independently of the surface orientation whenever the oxygen chemical potential is near that of the bulk oxide (*11*, *13*, *14*). To date, it is not clear if such surface oxides do also form on the different facets of NPs and, if so, whether they are relevant in industrial catalysis.

In the past, transmission electron microscopy (TEM) has shown that metal NPs undergo shape changes as a function of the gas composition (*15*–*17*). Scanning tunneling microscopy experiments on the top facet of flat NPs have illustrated oxygen-induced superstructures at the edges of different facets (*18*), and recently, the shape of unsupported Pd and Rh NPs was investigated by density functional theory as a function of the oxygen chemical potential using the Wulff construction (*19*). The results of these experiments prove that surface oxides stabilize the low-index (100), (110), and (111) facets at chemical potentials near that for bulk oxide formation, which results in an overall rounding of the NPs.

To upgrade our microscopic understanding of the catalytic activity of NPs, the interplay between the shape and size change of the NPs and the oxidation/reduction process must be established. Here, we report an in situ high-resolution x-ray diffraction (XRD) study of epitaxial Rh NPs on MgO(001) during oxidizing and reduction reactions, which uncovers a reversible facet rearrangement of the NP in direct relation to the formation of oxygen-induced superstructures. From a quantitative analysis of the extended reciprocal-space maps that have been recorded from the Rh nanofacets at elevated temperatures and under varying gas atmospheres, we can access the average NP shape and size with atomic resolution and obtain robust atomic insights into the structure of the surface oxide forming on the facets.

The XRD experiments were performed at beamline BM32 of the European Synchrotron Radiation Facility and at the Max Planck beamline of the Angström Quelle Karlsruhe. The photon energies were 11.04 and 10.5 keV, respectively. The in situ x-ray analysis was complemented by high-resolution TEM (HRTEM) performed on a JEOL 1250 atomic-resolution microscope that is operated at 1250 kV (*20*).

In the first experimental setup, we deposited the Rh NPs in situ at a substrate temperature of 670 K in the BM32 ultrahigh vacuum (UHV) surface XRD chamber, after cleaning the MgO substrates by sputtering and annealing under oxygen atmosphere (*20*). After the growth and an initial oxidation/reduction cycle, the sample was annealed at 970 K to achieve the equilibrium shape of the NPs. Wide-angle diffraction reciprocal-space mapping and grazing-incidence small-angle scattering (GISAXS) were performed simultaneously (*20*). In the second experimental setup, Rh was deposited on MgO in a laboratory UHV chamber, annealed at 870 K, and the sample was subsequently transferred into a portable UHV XRD chamber, which was shipped to the synchrotron radiation facility while maintaining UHV conditions. The epitaxial relation between the Rh NPs and the MgO substrate was determined from reciprocal-space scans in high-symmetry directions. We find that the Rh NPs grow in a cube-on-cube epitaxy on MgO(001), with an in-plane angular distribution of 1.7°. After the annealing, the average lattice constant of the particles is equal to the bulk value for Rh (a_{fcc} = 0.380 nm, where fcc is face-centered cubic), resulting in a misfit of 9% to the MgO substrate. The particles exhibit a typical size distribution of ~30%.

Figure 1A is a schematic view of the NP model together with the four shape parameters N_P, N_T, N_B, and N_E, which can be interrogated by XRD (*21*). N_P describes the particle diameter given by $a_{fcc}/\sqrt{2}\cdot N_P$; N_T and N_B describe the number of atomic layers involved in the top and bottom part of the particle, respectively. The parameter N_E gives the number of layers removed from the particle corners to form the side [100] type facets. The extended reciprocal-space maps contain detailed information about the shape and size of nanoscale objects (*22*). This is illustrated in Fig. 1B, which shows an experimental wide-range reciprocal-space map of the (110) plane taken at 600 K. The (111) Bragg reflection in the center of the map is interconnected with the neighboring Bragg reflections by broad intensity ridges along the [001], [−1,1,1], and [1,−1,1] directions that emanate perpendicularly from the associated facets. The observation and quantitative analysis of these so called "crystal truncation rods" (*23*) in four symmetry-equivalent directions gives direct evidence for the truncated pyramidal shape of the nano-objects under investigation.

To obtain detailed information on the size and shape of the NPs, high-resolution reciprocal-space maps have been recorded from $(H,K) = (-0.5,0.5)$ to $(0.5,-0.5)$ and from $L = 0.6$ to 0.84, as indicated by the white box in Fig. 1B (here, H, K, and L represent the Miller indices of the bulk reciprocal lattice). In Fig. 2A (top) a high-resolution map of

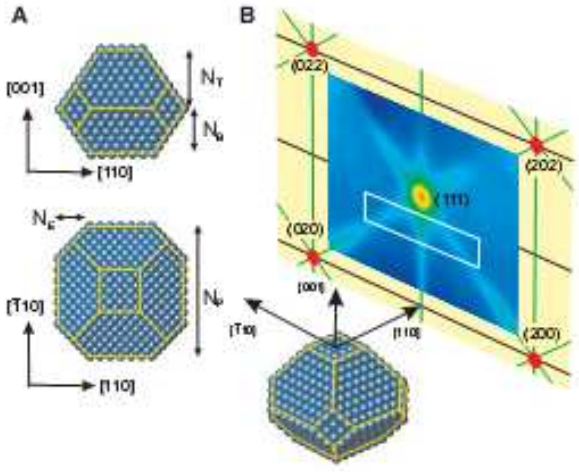

Fig. 1. (**A**) Schematic representation of the particle shape for fcc-based NPs. The lateral particle size is characterized by $a_{fcc}/\sqrt{2}\cdot N_P$, its height by $a_{fcc}/2\cdot(N_T + N_B)$, and the missing edge atoms by N_E. For a Wulff shaped particle (without substrate), $N_T = N_B$ and $N_E = N_P - N_T$ (*25*). (**B**) (110) plane reciprocal-space map of clean Rh NPs on MgO(001) with an average lateral size of 8 nm. Fcc bulk coordinates are used throughout the text, if not otherwise indicated. The white box indicates the area for high-resolution scans used for the quantitative analysis. The reciprocal-space area close above the Bragg peaks cannot be used, because it contains, on the (111) type rods, signal from internal twinning of the particles at $(^2/_3,^2/_3,^4/_3)$, $(^4/_3,^4/_3,^2/_3)$, and equivalent positions (Fig. 4).

[1]Max-Planck-Institut für Metallforschung, Heisenbergstrasse 3, D-70569 Stuttgart, Germany. [2]Institut Nanosciences et Cryogénie/Service de Physique des Matériaux et des Microstructures, Commissariat à l'Energie Atomique, Grenoble, 38054 Grenoble Cedex 09, France.

*To whom correspondence should be addressed. E-mail: sterte@mf.mpg.de

the clean particles is plotted, as observed at 600 K under UHV conditions. The data can be understood in a straightforward way within a kinematical diffraction theory that discloses NPs with truncated octahedral shape (*20*). Figure 2A (middle) shows the best intensity fits associated with the average particle shape presented in Fig. 2A (bottom).

A straightforward understanding of the shape of a NP is provided by the Wulff construction, which is based on the rule $\frac{\gamma_i}{h_i} = \text{constant}$ (here, γ_i is the surface energy of facet plane i with distance h_i from the center of the unsupported particle) (*24*). From the fit to the data, we obtain the following parameter values: $N_F = 31 \pm 1$, $N_T = 20 \pm 1$, $N_H = 5 \pm 1$, and $N_E = 3 \pm 1$, corresponding to an average NP diameter of 8.3 nm and an average NP height of 4.8 nm. For the ratios of the surface energies, we deduce $\frac{\gamma_{100}}{\gamma_{111}} = \frac{h_{100}}{h_{111}} = \sqrt{3}\cdot\frac{N_T}{N_F} = 1.12 \pm 0.09$ for the top facets, which agrees well with the theoretical value of $(\gamma_{100}/\gamma_{111})^* = 1.16$ (*19*), but $\frac{\gamma_{100}}{\gamma_{111}} = \sqrt{3}\frac{N_F - N_H}{N_F} = 1.56 \pm 0.06$ for the side facets (the asterisk indicates theoretical values). This marked deviation from the expected value of $(\gamma_{100}/\gamma_{111})^*$ means that the side facets are noticeably smaller than predicted by the Wulff argument. We suggest that this observation is related to strain and/or NP edge effects (line tensions) neglected in the Wulff approach. The Rh NP adhesion energy $E_{ad} = \gamma_{100}\cdot\frac{N_T - N_E}{N_T} = 108 \pm 10$ meV/Å^2 (*25*) is less than the theoretical value $E_{ad}^* = 130$ meV/Å^2 associated with one extended monolayer of Rh on MgO(001), which is in line with the trend that the adsorption energy decreases as a function of the Rh coverage (*26*).

In the next step, the Rh NPs were exposed to 3×10^{-5} mbar O_2 at 600 K [i.e., above the oxygen chemical potential for Rh_2O_3 bulk oxide formation (*27*)], and we simultaneously recorded the XRD pattern (Fig. 2, B and C). We observed a distinct change in the XRD signal (see difference map in Fig. 2B) that essentially consists of an intensity enhancement along the (001) rod and an intensity loss along the (111) rods, which can also be observed in the large area difference map in fig. S2B (*28*). The best fit to this x-ray intensity change (Fig. 2B) results in an average NP shape as characterized by $N_F = 31 \pm 1$, $N_T = 16 \pm 1$, $N_H = 5 \pm 1$, and $N_E = 7 \pm 1$ (Fig. 2C), with an unchanged average NP diameter of 8.3 nm and a reduced average height of 4 nm. These reconfigured Rh NPs now have a nanosized oxide skin composed of an ultrathin hexagonal surface oxide layer, as we explain below.

An unexpected result of this analysis is that the area of both the (100) side facets and the (001) top facet increases upon oxidation (*29*). This result implies that only intraparticle mass transport takes place during oxidation, which removes Rh atoms from the (100) side and top facets with an average amount that corresponds to the number of atoms incorporated into the surface oxide layers on all facets. However, the strong increase of the (110) facet area, which is predicted by theory (*19*) for the conditions applied, was not observed. Furthermore, no additional facets are formed in between the top (001) and (111) facets (they would readily be observable via additional diffraction intensities).

To get a microscopic insight into the forces that drive this NP shape transformation, we interrogated the atomistic structure of the oxidized (001) and (111) facets by quantitative surface XRD. Figure 3A shows a line scan along the (1,–1,0) direction ($L = 0.3$) associated with clean NPs and NPs exposed to 2×10^{-5} mbar oxygen at 500 K, which witnesses the formation of an oxygen-induced (3x1) superstructure at the top (001) nanofacet that progressively disappears upon further oxidation. The intensity of these superstructure reflections cannot be explained by a simple oxygen chemisorption structure; it is rather in line with a shifted-row structure that creates threefold adsorption sites for oxygen (Fig. 3B). The two-dimensional character of this structure can be inferred from the rodlike diffraction pattern (Fig. S4). A similar structure appears during the oxidation of $Pt_{25}Rh_{75}(100)$ single crystals (*30*) as a precursor for the surface oxide formation on Rh(100) (*13*).

When the sample temperature was only slightly increased to 550 K, a fast transformation takes place on the (001) top facets from the (3×1) adsorption structure to the hexagonal surface oxide that forms a c(2×8) coincidence structure with the underlying Rh lattice (Fig. 3, C and E) (*13*). At the same time, on the (111) side facets a hexagonal surface oxide is formed with a p(9×9) coincidence structure. The c(2×8) coincidence structure on the (001) facets and the p(9×9) structure on the (111) facets give rise to additional peaks that can be readily identified (Fig. 3C).

In the presence of the surface oxide on both the (111) and (100) facets, the theoretical value of the surface free energy ratio is lowered to $(\gamma_{100}/\gamma_{111})^* = 0.9$ (*19*). This value needs to be compared with our experimental data $(\gamma_{100}/\gamma_{111}) = \sqrt{3}\cdot\frac{N_T}{N_F} = 0.89 \pm 0.09$ and $(\gamma_{100}/\gamma_{111}) = \sqrt{3}\frac{N_F - N_H}{N_F} = 1.34 \pm 0.07$ for the top and side (100) facets, respectively. Thus, the observed increase of the total (100) type facet surface area is in good agreement with the Wulff prediction and can be directly related to the slightly higher stability of the surface oxide on the (100) facets, as compared with the (111) facets. Although bulk oxide formation is thermodynamically favored under the conditions applied (*27*), the surface oxide at

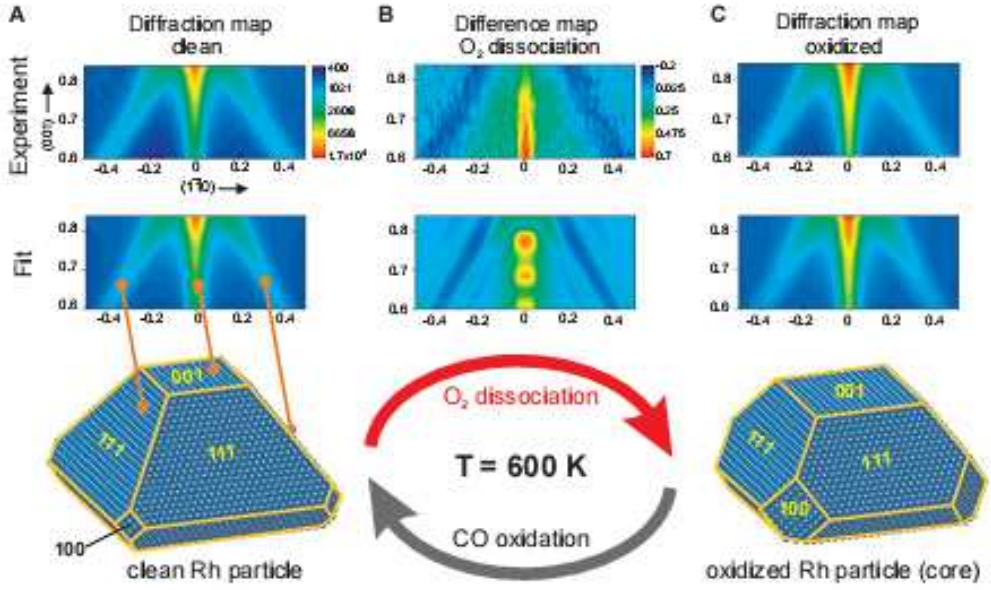

Fig. 2. (**A**) (Top) (110) diffraction map of clean Rh particles at 600 K. (Middle) Fitted diffraction map corresponding to the average particle shape given below. (**B**) (Top) oxygen-induced signal change in the (110) plane. (Middle) Simulated signal change for particles with increased (100) side facet area. (**C**) (Top) Experimental (110) diffraction map at 600 K and 2×10^{-5} mbar O_2 pressure. (Middle) Fitted diffraction map for particles under oxygen exposure. (Bottom) Best-fit core particle shape after oxidation.

the Rh nanofacets is metastable and prevents bulk oxide growth.

A further key observation is that the oxygen-induced shape change of the Rh NPs is fully reversible when the surface oxide is removed by CO exposure (at 1×10^{-5} mbar). The observed x-ray intensity line scans (Fig. 3, C and E) obtained after reduction are identical to the clean particle scans, which is evidence for decomposition of the facet oxide layers. Simultaneously, the oxygen-induced intensity change of the scattering from the (111) and (001) facets (Fig. 2B) is reversible, as can be inferred from the line scans in fig. S3, demonstrating the reformation of the clean particle facets.

Complementary information on the shape of the Rh NPs has been obtained by GISAXS (*31*), which has been carried out parallel to the above surface XRD experiment and by cross-section HRTEM (*20*). The observed marginal changes of the GISAXS patterns and associated line scans for two different azimuths confirm that the average particle size does not change during the oxidation and reduction process (fig. S5). The cross-section TEM image (Fig. 4) taken of a Rh NP on MgO(001) along the (110) direction uncovers a NP shape that corresponds very well with the x-ray results (dashed line in Fig. 4A). We also observed structures with a different periodicity on the particle facets that can be identified as oxide over layers. In some cases (for instance, on the right facet of the particle in Fig. 4A), a one-monolayer-thick oxide layer can be observed with atomic resolution. The zoomed-in view of the white box in Fig. 4A reveals a surface layer on the (111) facet with a different periodicity, a finding that is strongly supported by the simulated TEM image contrast for the O–Rh–O surface oxide trilayer (box in Fig. 4B). The observation that the surface oxide is present, even after exposure of the sample to ambient conditions and the rather destructive TEM specimen preparation, gives us the first evidence for the presence of noticeable kinetic barriers toward bulk oxide formation once the surface oxide is formed.

Our high-resolution in situ oxidation experiments demonstrate that the surface oxide O–Rh–O trilayer stabilizes Rh NPs with low-index facets. We assume that this reversible shape transformation also occurs for smaller particles [as long as they have (111) and/or (100) facets] and that the observed surface oxide formation at the facets of the NPs also takes place in oxidation catalysis involving Rh NPs under technologically relevant conditions.

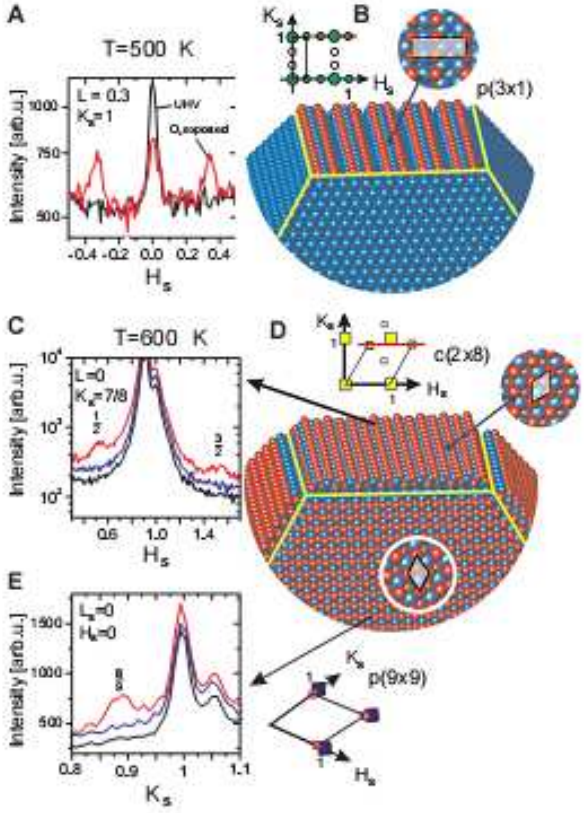

Fig. 3. (**A**) Line scans along the H_S direction in (100) surface coordinates (*13*). Black line, clean particles; red line, under oxygen exposure. (**B**) Reciprocal- and real-space lattice of the (3×1) shifted-row superstructure on the (001) particle top facet. The scans in (*A*) were performed at $K_S = 1$; see red line. The peaks at $H_S = -1/3$ and $1/3$ are characteristic for the (3×1) superstructure. (**C**) H_S scan in (100) surface coordinates ($K_S = 7/8$) along the red line in the top reciprocal lattice in (D). Satellite peaks at $H_S = 1/2$ and $H_S = 3/2$ give evidence for the c(2×8) coincidence structure of the hexagonal surface oxide (*13*) (hexagonal real- and reciprocal-space unit cells are indicated). (**D**) Structural model of a Rh NP on MgO, covered on all facets by a O–Rh–O trilayer surface oxide. (**E**) *K* scan along the (01) direction in surface coordinates (*11*) of the (111) side facet pictured in (D). The reflection at $K_S = 9/9$ stems from the surface oxide. (C and E) Black lines, clean surface; red lines, under oxygen exposure; blue lines, after CO reduction.

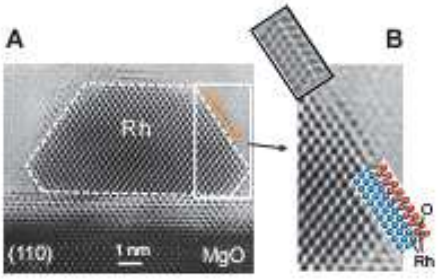

Fig. 4. (**A**) HRTEM micrograph of a Rh particle on MgO(001) in (110) view. On the left side, close to the substrate, a small twin is present with (111) twinning plane. From the XRD data, we can infer that ~5% of the particles are twinned. The dashed line represents the particle shape derived from the XRD data for the oxidized particles. The white box denotes the zoomed-in area of the surface oxide on (111) facets plotted in (B). (**B**) Atomically resolved structure of the O–Rh–O trilayer surface oxide on the (111) facets. In the box, a TEM image simulation is plotted as obtained from the structural model in the second inset. The dark spots correspond to Rh atom rows.

References and Notes

1. G. Ertl, H. Knözinger, F. Schüth, J. Weitkamp, *Handbook of Heterogeneous Catalysis* (Wiley-VCH, Weinheim, Germany, 2008).
2. M. D. Ackermann *et al.*, *Phys. Rev. Lett.* 95, 255505 (2005).
3. J. G. Wang *et al.*, *Phys. Rev. Lett.* 95, 256102 (2005).
4. E. Lundgren *et al.*, *Phys. Rev. Lett.* 92, 046101 (2004).
5. B. L. M. Hendriksen, S. C. Bobaru, J. W. M. Frenken, *Surf. Sci.* 552, 229 (2004).
6. C. H. F. Peden *et al.*, *J. Phys. Chem.* 92, 1563 (1988).
7. M. A. Newton, C. Belver-Coldeira, A. Martínez-Arias, M. Fernández-García, *Angew. Chem. Int. Ed.* 46, 8629 (2007).
8. M. Bäumer *et al.*, *Phys. Chem. Chem. Phys.* 9, 3541 (2007).
9. H. S. Gandhi, G. W. Graham, R. W. McCabe, *J. Catal.* 216, 433 (2003).
10. H. Over *et al.*, *Science* 287, 1474 (2000).
11. J. Gustafson *et al.*, *Phys. Rev. Lett.* 92, 126102 (2004).
12. J. Rogal, K. Reuter, M. Scheffler, *Phys. Rev. Lett.* 98, 046101 (2007).
13. J. Gustafson *et al.*, *Phys. Rev. B* 71, 115442 (2005).
14. C. Dri *et al.*, *J. Chem. Phys.* 125, 094701 (2006).
15. P. L. Hansen *et al.*, *Science* 295, 2053 (2002).
16. G. Rupprechter, K. Hayek, H. Hofmeister, *J. Catal.* 173, 409 (1998).
17. C. R. Henry, *Surf. Sci. Rep.* 31, 231 (1998).
18. K. Hojrup Hansen, Z. Sljivancanin, E. Laegsgaard, F. Besenbacher, I. Stensgaard, *Surf. Sci.* 505, 25 (2002).
19. F. Mittendorfer, N. Seriani, O. Dubay, G. Kresse, *Phys. Rev. B* 76, 233413 (2007).
20. See the supporting online material for details.
21. N. Kasper *et al.*, *Surf. Sci.* 600, 2860 (2006).
22. U. Pietsch, V. Holy, T. Baumbach, *High-Resolution X-Ray Scattering* (Springer, New York, 2004).
23. I. K. Robinson, D. J. Tweet, *Rep. Prog. Phys.* 55, 599 (1992).
24. G. Wulff, *Z. Kristallogr.* 34, 445 (1901).
25. W. L. Winterbottom, *Acta Metall.* 15, 303 (1967).
26. S. Noblin, J. Lintrakul, K. Hermansson, *Surf. Sci.* 566–568, 977 (2004).
27. This corresponds to a chemical oxygen potential (*29*) $\mu = -1.04$ eV. $\mu(Rh_2O_3)$ is -1.23 eV.
28. Noticeable oxygen-induced lattice distortions lead to intensity asymmetries between the low-*Q* and high-*Q* side of the associated Bragg point (where *Q* is the x-ray momentum transfer). Inspection of fig. S2B shows that this is not observed.
29. For slightly larger particles (diameter $D = 9$ nm), the formation of (100) side facet rods, in addition to (110) side facet rods, is observed upon oxidation. The latter is not observed for particles with $D = 8$ nm; for both see fig. S2.
30. M. Spiro *et al.*, *Surf. Sci.* 416, 384 (1998).
31. G. Renaud *et al.*, *Science* 300, 1416 (2003).
32. We thank G. Richter and M. Puddu for the preparation of Rh/MgO reference samples, N. Jeutter for help with the x-ray experiments, and the European Union for financial support under contract no. NMP3-CT-2003-505670 (NANO2).

Supporting Online Material
www.sciencemag.org/cgi/content/full/321/5896/1654/DC1
Materials and Methods
SOM Text
Figs. S1 to S5
References

22 May 2008; accepted 12 August 2008
10.1126/science.1160845

- J. Penuelas, P. Andreazza, C. Andreazza-Vignolle, H. Tolentino, M. De Santis, C. Mottet, *"Controlling structure and morphology of CoPt nanoparticles through dynamical or static coalescence effects"*,
Phys. Rev. Lett. 100, 115502 (2008).

Controlling Structure and Morphology of CoPt Nanoparticles through Dynamical or Static Coalescence Effects

J. Penuelas,[1] P. Andreazza,[1,*] C. Andreazza-Vignolle,[1] H. C. N. Tolentino,[2] M. De Santis,[2] and C. Mottet[3]
[1]*Centre de Recherche sur la Matière Divisée, UMR 6619 Université d'Orléans & CNRS, 1 bis, rue de la Férollerie, 45071 Orléans Cedex, France*
[2]*Institut Néel, CNRS & UJF, 25 avenue des Martyrs BP 166, 38042 Grenoble Cedex 9, France*
[3]*Centre de Recherche en Matière Condensée et Nanosciences-CNRS, Campus de Luminy, case 913, 13288 Marseille Cedex 9, France*
(Received 12 November 2007; published 18 March 2008)

The structure and morphology of 1 to 3 nm size CoPt nanoparticles have been investigated *in situ* and in real time under different conditions: growth at 500 °C or at room temperature (RT) followed by annealing at 500 °C. The small-angle x-ray scattering measurements show size and temperature dependent growth mode with particle motions on the surface, while wide-angle scattering results, supported by Monte Carlo simulations, allow structure identification. If icosahedra are systematically detected at the first growth stages at RT, annealing at 500 °C yields the decahedral structure from the quasistatic coalescence of icosahedral morphology. Meanwhile, growth at 500 °C proceeds by a dynamical coalescence mechanism at the early stage, yielding truncated octahedral cubic structures.

DOI: 10.1103/PhysRevLett.100.115502 PACS numbers: 61.46.Df, 61.82.Bg, 64.70.Nd, 68.55.A–

Magnetic nanoparticles (NPs) have attracted a lot of interest because of their applications in ultrahigh density recording media. In particular, FePt and CoPt NPs are especially promising due to the combination of size reduction and alloying effects, which lead to an enhancement of both their magnetic moment and anisotropy [1,2]. Apart from size effects, their magnetic behavior is governed by chemical composition [2,3] and influenced by the degree of chemical order or segregation and by morphology [4–6]. These latter parameters are highly dependent on kinetic processes during the NPs formation. Indeed, metastable multitwinned structures, such as large icosahedra or decahedra [7], as well as metastable chemical arrangements, such as onionlike clusters [8], may occur. To achieve suitable magnetic performances, thermal annealing, during or after the NPs growth, is often required [1]. Such thermal assistance may induce morphological changes [9] or important chemical rearrangements in the NPs [10,11]. Moreover, in the case of supported NPs, it may also modify their size and dispersion on the substrate by coalescence or Ostwald ripening. Thus, it is of primary importance to understand temperature effects on the NPs formation mechanisms since their properties are directly connected to their structure and spatial organization.

In this Letter we focus on the morphology and structure of 1 to 3 nm supported CoPt NPs studied *in situ* and in real time by grazing incidence small-angle x-ray scattering (GISAXS) and grazing incidence x-ray diffraction (GIXD). The growth temperature effect, and the result of 500 °C annealing, is reported in terms of the mobility of atoms and particles and in terms of their structural evolution. For such temperature and cluster size ranges, morphological and structural changes occur without long range chemical ordering [6,11,12]. GISAXS and GIXD can make a statistical analysis of the morphology, structure and chemical order of NPs over the whole sample [13]. Grazing incidence ensures a minimum probing depth, so that surface mechanisms may be studied with high sensitivity. *In situ* analysis under ultrahigh vacuum (UHV) is also of prime importance because of the high reactivity of CoPt NPs with their environment that affects their morphology and structure [12]. Time scales for each growth step (nucleation, coarsening, or coalescence) are large enough to allow real time experiments and to study dynamical processes. We demonstrate that irrespective of the chemical ordering, the role of coalescence prevails over size-dependent morphology and structure and yields decahedral or face centered cubic (fcc) structures according to the thermal treatment.

The experiments were performed using the UHV setup of the French-CRG (BM32) beam line at the European Synchrotron Radiation Facility, which combines molecular beam epitaxy (MBE) growth with GISAXS and GIXD techniques [13]. The 18 keV monochromatic x-ray beam was set at a grazing incidence angle α_i of 0.07° with respect to the sample surface. Two-dimensional GISAXS patterns were recorded with a CCD camera mounted at 1 m behind the sample. For the GIXD measurements, a standard scintillator detector was set at a fixed exit angle related to the sample surface ($\alpha_e = \alpha_i$) and the scattering vector q was changed by scanning the in-plane angle. Co and Pt atoms were codeposited by MBE under a pressure varying from 2 to 5×10^{-10} mbar depending on the deposition or annealing temperature. The amorphous SiO_2 substrate was covered with a 10 nm-thick amorphous carbon (a-C) film. Such film limits cluster-to-substrate interactions and allows comparisons with our previous transmission electron microscopy (TEM) results [11]. Co and Pt deposition rates [0.26×10^{15} atoms/(cm^2 h) for each kind of atom] were adjusted to yield a composition close to $Co_{50}Pt_{50}$ with a constant flux of atoms during all the growth stages.

Real time GISAXS measurements were performed with an interval of 30 min between each recording. Beyond 1 h of deposition time on the substrate held at 500 °C, the 2D GISAXS pattern exhibits two distinct lobes of scattered intensity [Fig. 1(a)] that are proportional to the form factor $F(q)$ and the interference function $S(q)$ of cluster assembly. $F(q)$ represents the Fourier transform (FT) of the particle shape and $S(q)$, the FT of the cluster-cluster pair correlation function so that the size, shape, and correlation distance Λ of the NPs can be extracted by simulations using ISGISAXS software [14] from the $q_\perp$ and $q_\parallel$ cross sections [Fig. 1(b)]. The form factor is calculated in the distorted-wave Born approximation, which includes substrate reflections of the scattered intensity and allows fitting the Yoneda peak [15]. The NPs have a truncated spherical shape with an aspect ratio $H/D < 1$ at the beginning of the growth, where D and H are the NPs diameter and height, respectively. The size distribution has been fitted using a narrow Gaussian function with a geometrical standard deviation of $\sigma(D)/D = 0.3$ according to our previous TEM results [11]. The evolution of D and H with time for NPs grown at 500 °C was derived [Fig. 2(a)] from that of the cross sections [Figs. 1(c) and 1(d)]. D increases as a power law during the deposition, the exponent (0.3) is in good agreement with theoretical predictions in the case of Volmer-Weber growth [16]. The NPs aspect ratio increases from 0.63 (truncated sphere) in the early stage to almost 1 at the end [Fig. 2(b)]. The shape goes to a more stable morphology (isotropic) similar to that obtained without support effect. In order to validate the GISAXS simulations, we performed *ex situ* TEM observations [Fig. 2(c)]. Statistical measurements gave an average diameter of 3.2 nm and an aspect ratio of 0.95. These measurements reported in Figs. 2(a) and 2(b) are in a remarkable agreement with the GISAXS results. The NPs density d is derived from the mean interparticle distance, by assuming one particle per Λ^2 surface. For small amounts of CoPt deposits, we observe a decrease of the NPs density [Fig. 2(b)] that we interpret as a dynamical coalescence, because their diffusion length is larger than their average separation Λ. Since the cluster mobility decreases as a power law when their size increases [17], it is understandable that dynamic coalescence stops after 4 h and the density remains almost constant until the end of the deposition.

GIXD patterns were obtained simultaneously with GISAXS measurements (Fig. 3). The background contribution ($t = 0$ h) is mainly the scattering of the amorphous substrate. Beyond 1 h deposition time, which corresponds to 0.52×10^{15} atoms/cm^2, the metal contribution to the scattered signal can be clearly distinguished from the background and increases with time. For the lowest deposited quantities, background subtraction is a crucial aspect of the data analysis. At these very low deposition times (insert in Fig. 3), the position of the main peak (29–30 nm^{-1}) is shifted, whereas beyond 4 h deposition time, a shoulder develops at 33 nm^{-1} simultaneously with the occurrence of another contribution around 47 nm^{-1}. In the early deposition steps, i.e., during the dynamical coalescence stage, we never observe the fcc structure but rather a noncrystalline atomic arrangement instead (amorphous or multitwinned). For longer deposition times, when the NPs density is nearly constant, the diffraction patterns exhibit the characteristic fcc peaks with an interatomic

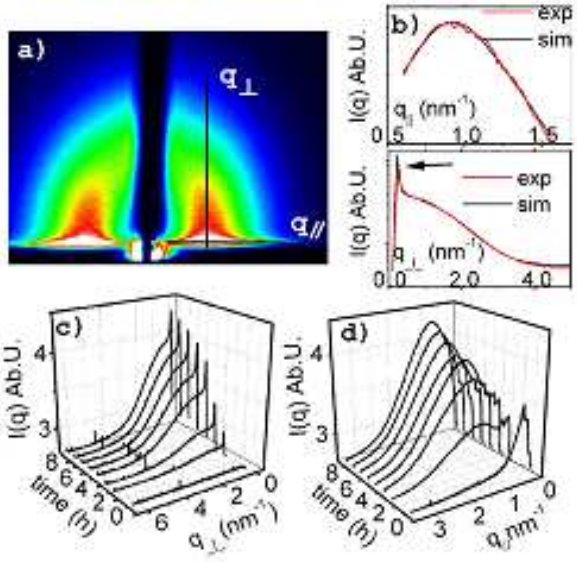

FIG. 1 (color online). (a) Measured GISAXS pattern of sample grown at 500 °C, after five hours corresponding to 2.6×10^{15} atoms/cm^2. The scattering vector q is separated in reciprocal space coordinates $q_\perp$ and $q_{//}$, perpendicular and parallel to the sample surface, respectively. (b) corresponding cross sections and fits. The arrow shows the Yoneda peak. (c) and (d) graphs show the evolution of $q_\perp$ and $q_{//}$, respectively, with deposition time.

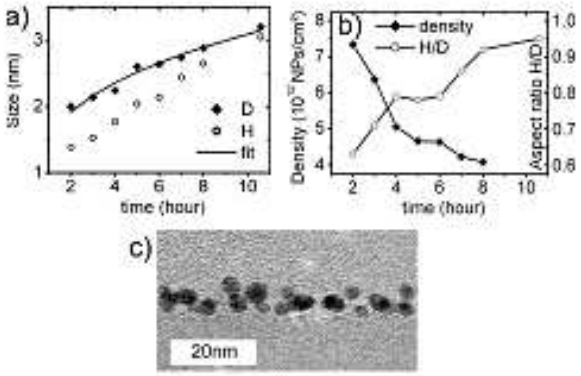

FIG. 2. From the fit of cross sections we deduce the evolution of (a) the mean diameter D and height H ($\pm$ 5%) and (b) the density d of CoPt NPs on the surface (the values at 10.6 h was deduced from TEM measurements) together with the aspect ratio H/D. (c) shows *ex situ* cross section TEM image of the sample.

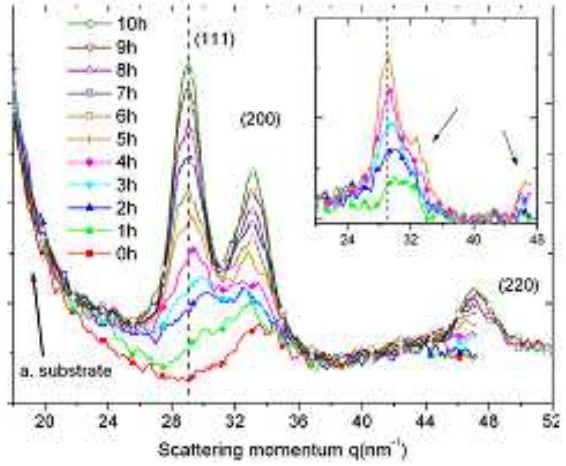

FIG. 3 (color online). Evolution of the GIXD patterns as a function of deposition time. 0 h diffraction data correspond to the background. The inset displays the first scans (up to 5 h) after background subtraction, arrows show fcc additional peaks.

distance of 0.265 nm, close to the fcc disordered bulk value [18], clearly pointing to Co and Pt alloying. However, one may wonder if the structure evolution from a noncrystalline arrangement at the beginning of deposition to a cubic structure after 4 h deposition is linked to the growth mode.

Further interpretation of these measurements requires better knowledge of size and structural effects on the diffraction pattern. The wide-angle scattering intensity for a model cluster i is calculated quantitatively on the basis of the Debye equation [19]:

$$I_{i,N}(q) = \sum_j \sum_{j' \neq j} \exp(-\sigma^2 q^2) f_j f_{j'} \frac{\sin(q r_{jj'})}{q r_{jj'}} + S_{\mathrm{inc}}(q),$$

where f_j is the atomic scattering factor of the jth atom, $r_{jj'}$ is the distance between atom j and atom j', and σ^2 is the mean-square displacement in the Debye-Waller prefactor, which expresses the attenuation of the interference term in the Debye equation, due to thermal vibrations or/and static random defects. $S_{\mathrm{inc}}(q)$ is the incoherent scattering function. Preliminary, calculations of the polarization and absorption evolution effects were made but were neglected due to their weak change with q. We have used three structure types in our cluster models: truncated octahedral (TOh) based on face-centered-cubic structure, decahedral (Dh) and icosahedral (Ih) according with Wulff, Marks, and Ino constructions [20], respectively. To fit the diffraction patterns, we used either single size and single cluster type, or a weighted sum of the intensities from several sizes or structures [7]. Models composed of clusters (between 50 and 2000 atoms) with complete shells have been found to be sufficient for data analysis. Monte Carlo simulations of a representative small number of relaxed CoPt cluster structures (TOh, Dh, and Ih illustrated in the inset of Fig. 4) were performed using a semiempirical tight-binding potential [6], to validate the diffraction profiles of these geometrical models [7]. It is worth noting that the possible ordering of the clusters in their low temperature phase has been taken into account in the analysis. However, as mentioned above, in the *in situ* experiments performed at 500 °C, chemical disorder is more probable for NPs smaller than 3 nm as predicted by the Monte Carlo simulations [6].

Figures 4(a) and 4(c) show two stages (5 and 10 h deposition times) of the growth at 500 °C with diameters centered at $D = 2.5$ and 3.2 nm, respectively. For the largest dimension, i.e., cluster with about 1300 atoms, the sample is dominated by fcc clusters, with a small fraction of icosahedral ones (less than 10%). For the smallest dimension, the best fit is obtained with a mix of Ih and TOh-fcc models (around 50% each in atomic fraction) with about 309 and 405 atoms, respectively. Decahedral models were also considered, but no improvement in the fit quality was found. These results show a structural evolution with the NPs size that is predicted in first approximation by energetic stability calculations in metallic clusters [21]. The icosahedral shape is the most energetically stable structure for small dimensions, while fcc clusters are favored for larger ones. Thus, one possible interpretation is that this continuous shape transition, from Ih to TOh structure, is only due to a size effect and the clusters reaching their equilibrium shape during the growth [6].

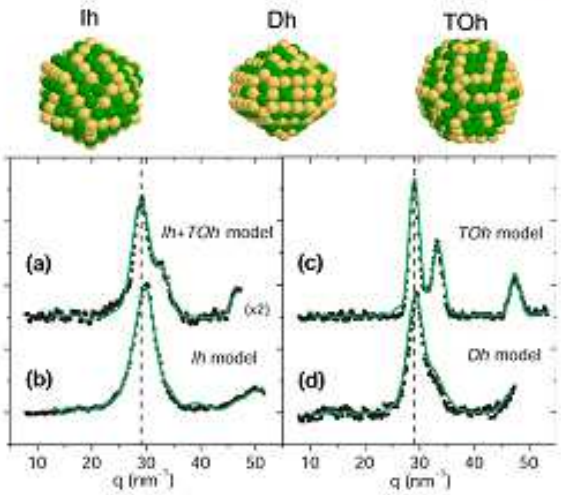

FIG. 4 (color online). Snapshots of icosahedral (Ih), decahedral (Dh) and truncated octahedral (TOh) clusters, and experimental (square marks) and calculated (green or gray solid line) diffraction patterns of similar size distribution samples: $D = 2.5$ nm (a) growth at 500 °C (2.6×10^{15} at/cm^2) and (b) growth at RT (5.2×10^{15} at/cm^2); $D = 3.2$ nm (c) growth at 500 °C and (d) annealing the sample (b) at 500 °C during 1 h. Profiles were offset vertically, and a magnification was applied in one case (in parentheses). A vertical dashed line corresponding to the fcc (111) line of 500 °C grown sample is given for comparison.

However, for small sizes, the 50:50 Ih and TOh-fcc mixture indicates that the sample is still under nonequilibrium conditions. Indeed, the GISAXS results concerning the evolution of the shape and cluster density suggest a coalescence process during the early growth stage. Such events can provide sufficient internal morphological disruption [22] to allow the NPs transformation to the minimum energy morphology, i.e., the TOh shapes at larger sizes [23].

These results have been compared with those obtained for a sample grown at room temperature and then annealed at 500 °C, whose spectra have been chosen to correspond to equivalent cluster sizes:

(i) At room temperature (RT), assuming a size distribution with Gaussian shape (centered between $N = 309$ and 561 atoms), the icosahedral model alone fits the data quite well [Fig. 4(b)]. The growth mechanism at RT is completely different from that at 500 °C: the NPs density is higher (11×10^{12} NPs/cm^2) and the dynamical coalescence is inhibited. After the nucleation stage, the growth at RT corresponds to an atom-by-atom impingement and the initial Ih structure is preserved without transition towards TOh structures [23]. In addition, a shift in the diffraction profile is observed, corresponding to a contraction of the average interatomic distance ($r_i = 0.263$ nm) with respect to the fcc model ($r_i = 0.268$ nm) in the 500 °C sample. Indeed, the contraction is too large to be explained by a thermal effect [6], but is coherent with the denser packing of the Ih structure. For similar NPs size and deposition temperature (RT), Favre *et al.* [4,12] found TOh NPs rather than Ih ones, which could be explained by a matrix effect. Indeed, their NPs were subsequently covered by a thin amorphous silicon layer or embedded in a matrix, thus favoring fcc structures.

(ii) After annealing this sample at 500 °C for 1 h, an average NPs size of 3.2 nm is reached. GIXD refinements [Fig. 4(d)] are consistent with decahedral clusters (centered at $N = 967$) with an average interatomic distance of 0.265 nm. The diffraction signature of Ih and TOh models does not show any similarity with the experimental data. GISAXS measurements indicate that the annealing process induces a decrease of the particle density (6×10^{12} clusters/cm^2) simultaneously with the increase of the particle size from 2.5 to 3.2 nm, which are characteristic of the Ostwald-ripening or static coalescence process [11]. The present structure differs from that of the 500 °C grown sample [Fig. 4(c)] because the kinetic and dynamic history of the samples are different. In the first case (500 °C growth), dynamical coalescence occurs at the early stage of the growth. After this stage, the fcc resulting morphology is locked in and the size increase is dominated by an atom-by-atom growth mechanism. In the second case, the coalescence occurs upon annealing, when the particle size is larger and simultaneously the interparticle distance smaller. Thus, the Dh structure is the result of a quasistatic coalescence [23,24] of Ih structures.

In summary, we have shown, experimentally and with the support of Monte Carlo simulations, the effect of temperature on the structure and morphology of CoPt nanoparticles. Dynamical coalescence in the early stage ($N < 300$ atoms) of growth at 500 °C yields the formation of fcc clusters, while atom-by-atom growth at room temperature produces almost exclusively the nonequilibrium icosahedral morphology. On the other hand, the coalescence from Ih particles (>300 atoms) induced by annealing, yields the formation of decahedral rather than fcc morphology. These *in situ* and real time results bring new understanding of the coalescence versus size effect on small (<3 nm) bimetallic nanoparticle structural transitions at different temperatures.

We acknowledge beam time by the French-CRG of ESRF as well as the help of the BM32 beam line staff. Special thanks to G. Renaud (BM32) for GISAXS training and to T. Sauvage (CERI-Orleans) for RBS facilities.

*Corresponding author.
Pascal.Andreazza@univ-orleans.fr

[1] S. Sun *et al.*, Science **287**, 1989 (2000).
[2] S. Rohart *et al.*, Phys. Rev. B **74**, 104408 (2006).
[3] P. Imperia *et al.*, Phys. Status Solidi (a) (to be published).
[4] P. Moskovkin *et al.*, Eur. Phys. J. D **43**, 27 (2007).
[5] N. Jaouen *et al.*, Phys. Rev. B **76**, 104421 (2007).
[6] G. Rossi, R. Ferrando, and C. Mottet, Faraday Discuss. **138**, 193 (2008).
[7] D. Reinhard *et al.*, Phys. Rev. B **55**, 7868 (1997).
[8] F. Baletto, C. Mottet, and R. Ferrando, Phys. Rev. Lett. **90**, 135504 (2003).
[9] K. Koga, T. Ikeshoji, K.I. Sugawara, Phys. Rev. Lett. **92**, 115507 (2004).
[10] D. Alloyeau *et al.*, Nanotechnology **18**, 375301 (2007).
[11] J. Penuelas *et al.*, Surf. Sci. **602**, 545 (2008).
[12] L. Favre *et al.*, Phys. Rev. B **74**, 014439 (2006).
[13] G. Renaud *et al.*, Science **300**, 1416 (2003).
[14] R. Lazzari, J. Appl. Crystallogr. **35**, 406 (2002).
[15] Y. Yoneda, Phys. Rev. **131**, 2010 (1963).
[16] M. Zinke-Allmang, L.C. Feldman, and M.H. Grabow, Surf. Sci. Rep. **16**, 377 (1992).
[17] P. Jensen, Rev. Mod. Phys. **71**, 1695 (1999).
[18] J.M. Bugnard, Y. Gauthier, and R. Baudoing-Savois, Surf. Sci. **344**, 42 (1995).
[19] B.E. Warren, *X-Ray Diffraction* (Dover, New York, 1990).
[20] L.D. Marks, Rep. Prog. Phys. **57**, 603 (1994).
[21] F. Baletto and R. Ferrando, Rev. Mod. Phys. **77**, 371 (2005).
[22] S. Hendy, S.A. Brown, and M. Hyslop, Phys. Rev. B **68**, 241403(R) (2003).
[23] G. Grochola *et al.*, J. Chem. Phys. **126**, 164707 (2007).
[24] S. Tsyganov *et al.*, Phys. Rev. B **75**, 045421 (2007).

IV. 3. SUV : selected scientific results

Self-assembling of magnetic nanoparticles on nanostructured oxide templates: a GIXRD and GISAXS study. FR-32-03-674

Maurizio De Santis[1], Andreas Buchsbaum[2], Helio Tolentino[1], Marcio Soares[1].
1 MCMF, Institut Néel, CNRS-BP166, 25 av. des Martyrs, 38042 Grenoble Cedex 9, France.
2 Institut für Allgemeine Physics , Technische Universität Wien, A-1040 Wien, Austria.

The aim of this experiment was to exploit the nanostructuring observed at the surface of ultrathin oxide layers for growing self-assembled magnetic nanoparticles.

Self-assembling of metallic clusters on nanostructured templates is a very active surface science research area. Step edges or dislocation networks on single crystal substrates are used for preferential positioning of atoms during film deposition. Depending on the deposition conditions, compact or fractal shape, nanowires or three-dimensional islands can be prepared. This research is motivated by the new electronic, magnetic and catalytic properties expected for these extremely small nanostructures. Preferential nucleation sites, generated by a lateral strain modulation, were found in the Moiré pattern of FeO(111) layers grown on Ru(0001) [1] and Pt(111) [2], which was exploited for the preferential nucleation of Fe_3O_4 island-like domains, and of Fe and V clusters, respectively.

In this experiment we wanted to exploit the Moiré pattern observed during the growth of CoO/Pt(111) (fig.1) to self-organize magnetic clusters of nanometric size.

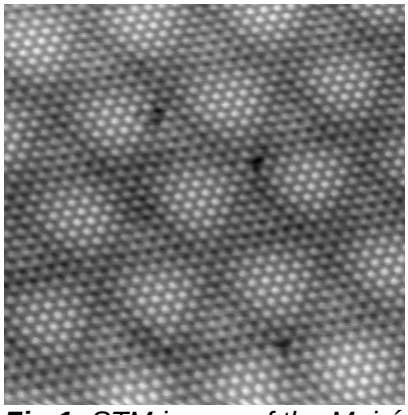

Fig 1: *STM image of the Moiré pattern of 1ML CoO/Pt(111).*

Preliminary results showed that clusters formed by evaporation of transition metal atoms (Co, Pd) do not self-organize at room temperature. At higher temperature (200℃) the Moiré pattern is irreversible destroyed during evaporation.

For this reason, we moved to a more stable nanostructured oxide film, the $(\sqrt{67}\times\sqrt{67})R12.2°$ reconstruction obtained by oxidation of $Ni_3Al(111)$ [3], thanks also to a collaboration of the *Institut Néel* with the *Technische Universität* of Vienna. The experiment was performed recently and the data analysis is in progress. Deposition of Co on the $(\sqrt{67}\times\sqrt{67})R12.2°$ resulted in the grown of self-organized nanoparticles in the low coverage regime, as shown by GISAXS of Fig. 2 and in agreement with previous STM measurements. GISAXS allowed following the nanoparticles coalescence. The structure of the final deposit (10 ML) was studied by GIXRD.

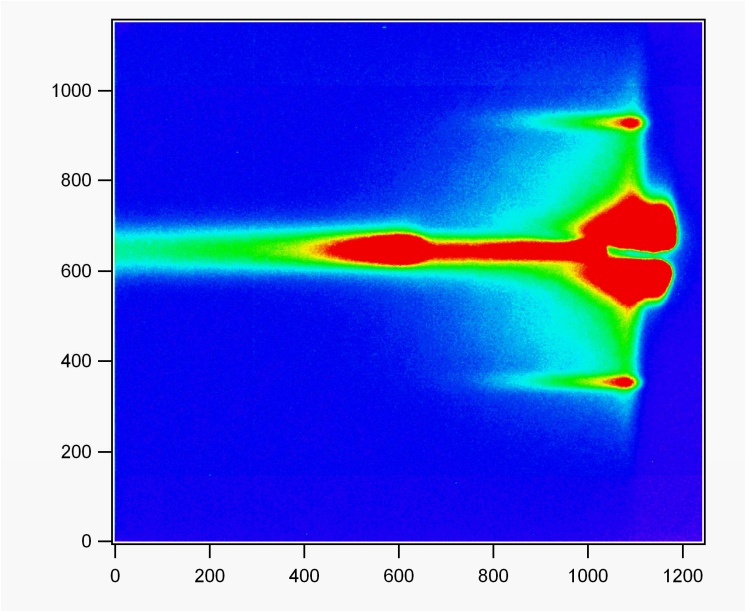

Fig 2: *GISAXS of 1 ML Co on ultrathin* (√67×√67)*R*12.2° aluminium oxide on $Ni_3Al(111)$

The aim was mainly to establish whether the nanoparticles are fcc or hcp, the compact hexagonal atomic layer being parallel to the surface. The magnetic anisotropy is strongly dependent on the structure. A first analysis shows that the staking is random.

[1] G. Ketteler and W. Ranke, Phys. Rev. B 66, 033405 (2002).
[2] N. Berdunov, G. Mariotto, K. Balakrishnan, S. Murphy and I. V. Shvets, Surf. Sci. 600, L287 (2006).
[3] M. Schmid, G. Kresse, A. Buchsbaum, E. Napetschnig, S. Gritschneder, M. Reichling and P. Varga, PRL 99, 196104 (2007).

X Ray diffraction study of self-organized tert-butyl- calix[4]arenes film deposited on Au(110)(1x2) FR-32-03-674

V. Abad-Langlais[1,2], Y. Gauthier[2], Maurizio De Santis[2], Helio Tolentino[2], Xavier Torrelles[3]
1 Departament de Física, Universitat Autònoma de Barcelona, 08193 Bellaterra (Barcelona), Spain
2 MCMF, Institut Néel, CNRS-BP166, 25 av. des Martyrs, 38042 Grenoble Cedex 9, France
3 ICMAB, 08193 Bellaterra (Barcelona), Spain

The aim of this experiment is to investigate the growth and the structure of p-tert-butyl-calix[4]arene molecules on the (1x2) reconstructed Au(110) surface by grazing incidence surface X-ray diffraction (GIXRD). The main applications of calixarenes reported up to date are their use as sensors[1,2]. Functionalized calix[4]arene derivatives exhibit, for example, sodium ion selectivity while calix[6]arene has shown excellent sensitivity to cesium ions. In supramolecular chemistry, the calixarene molecules are known for their properties as receptors of neutral and ion guests[3-5]. Although the ability of these molecules to accept guest species and/or to act as sensor highly depends on their structural properties, only indirect studies have been carried out up to date to determine their orientation with respect to the substrate and relatively to their neighbouring molecules. This study is of importance for interfacial supramolecular assemblies, since further interaction with organic or inorganic species could either be promoted or forbidden by the type of molecule-substrate interaction.

We have deposited the tert-butyl-calix[4]arenes on Au(110). The molecule is 12 Å long and the initial substrate surface is a (1x2) missing rows reconstruction. The deposition temperature has been optimized following the disappearance of the 0 ½ fractional rods of the substrate and the optimum temperature has been found at in the range of ~ 200-250ºC. STM images obtained on a monolayer allow seeing a regular distribution of the molecules. They form long chains along the [1-

10] direction (fig. 1). Each molecule appears as 4 circular lobes which can be assigned to the phenol groups, which mean that in this configuration, the tert-butyl groups cannot be imaged by STM. The detailed analysis of the STM images is quite difficult and a full interpretation can only be achieved thanks to the X-ray diffraction results. GIXRD data allow us to identify correctly the unit cell. The STM visible chains are formed by two different molecular conformers. In the unit cell, the molecules are rectangular and their dimensions are similar to those in gas phase, while in the centre of the unit cell, they adopt a more elongated geometry. The LEED pattern is also very complicated and due to the distortions of the low working energy, its analysis requires additional information provided by the X ray diffraction results. The experiment carried out at BM32 permits to resolve the structure: the tert-butyl-calix[4]arenes are arranged into a rectangular cell with 4 molecules per cell. Similarly to the « simple » calixarenes case, the substrate suffers a drastic reconstruction change and its surface became a (1x3) missing rows upon molecular absorption. The coincidence cell is a (21x14). In the [100] direction, the x14 corresponds in fact to a 4* (1x3) +1* (1x2), which is confirmed by the STM images (fig. 2) which show large bands assigned to the 1x3 together with some narrower bands corresponding to the (1x2), but without real space regularity.

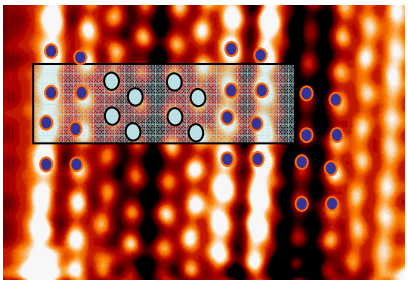

Fig 1: *High resolution STM image showing the molecular internal structure (10 nm x12 nm).*

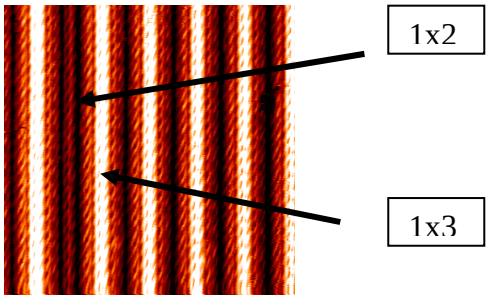

Fig. 2: *STM Image showing the (30 nm x30 nm) bands width alternating.*

In fig. 3, two scans acquired respectively in the H and K directions show the periodicity of the molecular overlayer. Due to the large surface periodicity and surface disordering, only some of the fractional rods are visible. The strongest reflexions arise from the averaged cells.

In conclusion, the gold substrate suffers a partial reconstruction and adapts itself to the molecules by adopting a (1x3) missing rows reconstruction probably due to a charge transfer. The coincidence cell is found to be a (21x14) corresponding in the K direction to the alternating large/narrow bands seen by STM. In this work, the complementarity of the experimental techniques (STM, LEED and GIXRD) is of fundamental importance to resolve the structure.

1. Rösler S., Lucklum R., Borngräber R., Hartmann J., Hauptmann P., *Sensors and Actuators B* 1998, 48 415–424
2. Kunsági-Máté S. , Bitter I., Grün A., Nagy G., Kollár L., *Anal. Chim. Acta* 2001, 443 227–234
3. Gutsche C. D., Calixarenes in Monographs in Supramolecular Chemistry, edited by Stoddart J.F., Royal Society of Chemistry, Cambridge, 1998
4. *Calixarenes in action*, edited by Mandolini L. and Ungaro R., Imperial College Press, London, 2000
5. *Calixarenes 2001*, edited by Z. Asfari, V. Bohmer, J. Harrowfield and J. Vicens, Kluwer Academic Publishers, Dordrecht, 2001

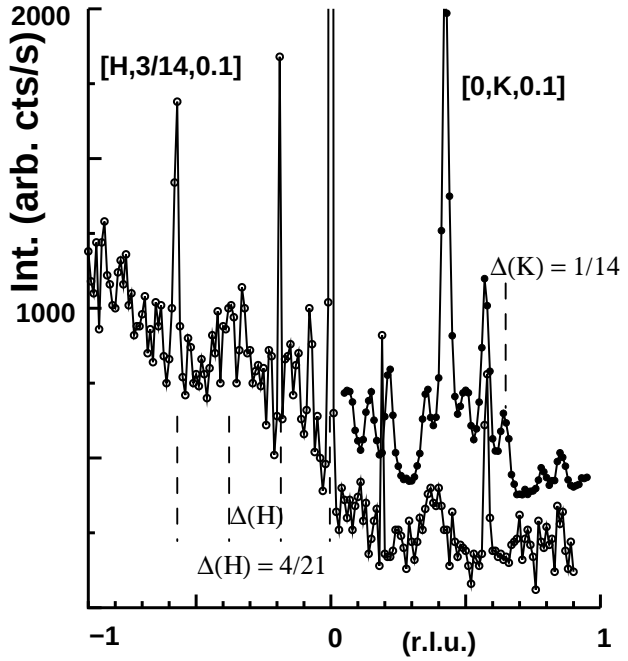

Fig 3: *H and K-directional scans (open and solid circles, respectively)indicating the periodicities of the (21x14)supercell. Due to the large surface periodiciy, and surface ordering, not all the reflections are observed, but mainly those coming from averaged supercells.*

Propagation and stability of stacking faults in Ir(111) homoepitaxy

S. Bleikamp, J. Coraux,† and T. Michely, G. Renaud[1], and O. Robach[1]
II. Physikalisches Institut, Universität zu Köln, Zülpicher Str. 77, D-50937 Köln, Germany
[1]CEA Grenoble, 17 rue des Martyrs, F-38054 Grenoble, France

Homoepitaxial growth is a basic playground for studying the kinetics of stacking faults (SFs) formation, as no SF should form relying on energetics. It is a first step towards understanding the practical issue of thin films microstructuration through SFs. It was recently successfully employed by two of the Authors, who discovered heterogeneous nucleation of SFs on monoatomic rows decorating the boundary between regular and SF areas in Ir(111).

We used X-ray surface diffraction to investigate *in situ* the propagation and stability of SFs during Ir(111) homoepitaxy, in ultra-high vacuum. Figure (a) shows the qualitative evolution of the integrated scattered intensity corresponding to the volume of (1) twinned crystallites, i.e. resulting from SFs along [111], (2) twinned crystallites resulting from SFs along an alternative <111> direction, and (3) crystallites twinned twice, corresponding to a SFs along [111] + another one along another <111> direction. The twinned signals are clearly identified on the crystal truncation rods (CTRs) by the presence of additional Bragg peaks. This is exemplified for the [01L] CTR [fig. (b)] where the regular fcc stacking peaks being only present in the case of the clean Ir(111) single crystal surface, are supplemented by twin peaks after the thin Ir film growth. While the defect type (1) was already observed by scanning tunneling microscopy (STM) by two of the Authors, defect types (2) and (3) were not identified up to now, and are now tentatively searched for in new STM measurements.

The monotonic increase of the various twin volumes directly points out the

propagation of the SFs which was proposed following STM observations. The similar trends observed, whatever the type of twin, indicate similar processes are involved. Starting with no SFs, the growth is first layer by layer and then dominated by a roughness increase after a couple of nm, as a result of the proliferation of SFs, consistent with the STM observations. While defect type (1) exhibits high thermal stability (above 1500 K), defects types (2) and (3) are found to disappear at moderate temperatures around 750 K. Preliminary quantitative analysis of the CTRs yield a 50±10 % volumic fraction of twins; thorough analysis will yield the absolute volume fraction of twins during deposit. A comprehensive growth model is currently developed to interpret the presence of the new defect types (2) and (3), the distinctive thermal stability of the different defects, as well as the sharp signals evolving from growth and pointing at well-defined locations in reciprocal space, such as the one highlighted in fig. (b). This should provide a unified picture of Ir(111) homoepitaxy through STM and X-ray surface diffraction.

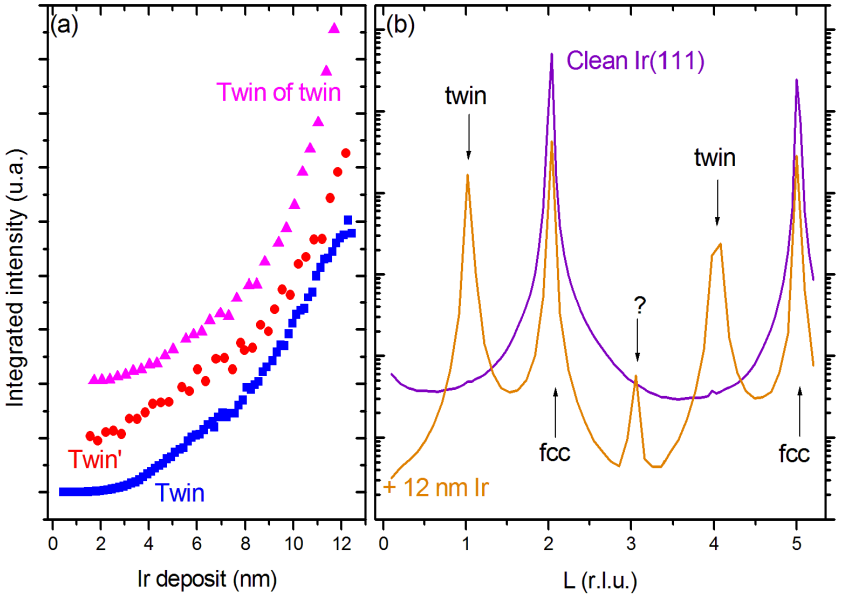

Figure: (a) Integrated intensity associated with the fraction of the crystal that are twinned with respect to (111) (blue), or another <111> plane (red), and twinned with respect to (111) + twinned with respect to another <111> plane (pink). Curves are vertically shifted for clarity. (b) [01L] CTRs of the bare Ir(111) single crystal (violet) and after 12 nm of Ir have been grown (orange). “fcc” and “twin” denote the regular fcc and the twin stackings Bragg reflections. “?” remains unidentified.

Understanding the MBE growth of GaN nanowires with *in situ* grazing incidence diffraction

Proposal number 32 02 722

O. Landré , H. Renevier, B. Daudin, R. Songmuang, G. Renaud
CEA-INAC and INPG/LMGP

III-Nitride semiconductor material is of major importance for blue and UV light emission applications. Unfortunately, the potentialities of the material are still plagued by the high density of dislocations (10^{10} cm^2) and other structural defects which result from the lack of lattice adapted substrates. GaN nanowires grown by MBE exhibit an exceptional crystalline quality and could be an option to overcome this difficulty. These defect-free nanostructures motivate a serious hope for creating high efficiency III-V nanowires based devices. The nucleation process of nitride nanowires (NWs) grown by molecular beam epitaxy (MBE) remains unclear. It was the aim of this *in situ* diffraction experiment, in grazing incidence, to elucidate the nucleation process. For instance, what are the seeds/precursors for NWs growth? How are they forming on the surface (Stransky-Krastanow process or Volmer-Weber one) ?

The samples were grown *in situ* in the SUV chamber. First, a thin (3nm) AlN buffer was grown on a Si(111) substrate. The AlN buffer enhances the orientation and the homogeneity (size, high) of the wires. Then at a high substrate temperature (760℃) (with respect to the temperature growth of conventional nitride layer or quantum dots) we exposed the surface with Ga and N fluxes

with a Ga/N ratio lower than 1 (N rich condition). Once optimized, these growth conditions gave rise to GaN nanowires well aligned along the c-axis. The diffraction experiment consisted in measuring the in-plane (3030) Bragg reflection of the GaN seeds/NWs and AlN buffer continuously during the growth. Grazing incidence setup, with an incident angle equal to 0.2° for the sample grown with the medium Ga flux and 0.15° for the sam ples grown with the higher and lower Ga flux, allowed us to be more sensitive to phenomena occurring on the surface by drastically decreasing the Si scattering. One advantage to work at synchrotron (ESRF) is the amount of photon available permitting us to decrease the scan duration at about 15 seconds and still having a good noise/signal ratio. The shorter is the time scan higher is the sensitivity to the very early stage of the growth. Furthermore we decided to reduce the amount of Ga impinging on the surface and hence slow down the nucleation process. We grew three samples with the same substrate temperature and N flux but with different Ga fluxes. Fig 1 shows *h*-scans across GaN and AlN (3030) Bragg peaks taken a different growth time for the sample grown with the medium Ga flux. Figure 2 shows the integrated intensity of the GaN diffraction as a function of time for the 3 different Ga fluxes.
These experiments brought about two main results:

1. Decreasing the amount of Ga impinging per second on the sample surface results in delaying the 3D growth.

2. Once the growth has started, the GaN diffracted intensity is a quadratic function of time at the beginning of growth then it is linear.

These results suggest three different stages during the GaN NWs formation :

1. First of all the growth begins with the formation of a layer of dots on the thin AlN buffer by a Stransky-Krastanov process. According to this process the formation of a two dimensional (2D) layer is followed by a three dimensional (3D) growth mode (dots formation). We interpret the delay to the nucleation as being the time for the formation of this 2D layer.

Note that the substrate temperature is high, then the Ga sticking coefficient is low, this explain why it takes such a long time to deposit only 2 ML of GaN.

2. Once the dots layer is formed, the sticking coefficient of Ga adatoms increases. Indeed the dots offer new nucleation centers where Ga and N adatoms can be adsorbed. Therefore the growth speed increases and enters in a coarsening stage. At the early stage of growth, the GaN diffracted intensity can be fitted with the equation A_0*t^x where A_0 and x were adjusted. We have found an exponent close to two for the three samples, this depict a coarsening by the sides of the dots.

3. And finally the dots end to grow laterally as a consequence they develop only by their top and give rise to the NWs growth. This explains the linear behavior of the growth after the quadratic one.

These growth behaviors: high lateral/low vertical growth rate for the dots at the early stage followed by a high vertical/low lateral growth rate for the wires has been first suggested Songmuang and *al*. (Appl. Phys. Lett. 91, (2007), 251902). Our x rays diffraction results strongly support this model of growth.

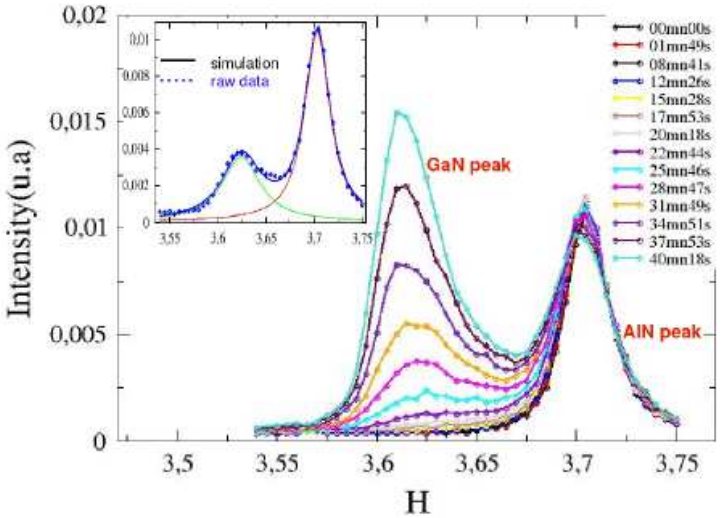

Figure 1: Bragg peaks of the (3030) GaN precursors/NWs (3,62) and AlN buffer (3,7) recorded as a function of time for the sample with the medium Ga flux. The incident angle was equal to 0.20°. The inset shows the

experimental and fitted h-scans recorded after 31 minutes of growth. This fit is made of two pseudoVoight functions: one corresponding to the AlN peak and the other to the GaN peak.

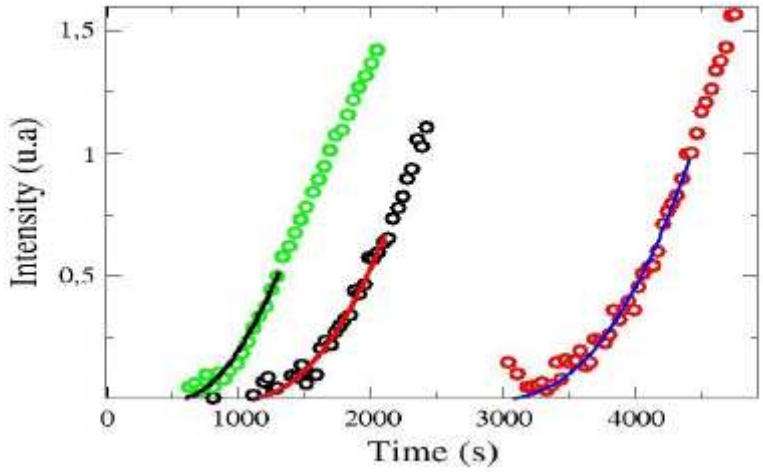

Figure 2: Open symbols represent the integrated area under the GaN peak for the three samples grown with different Ga flux. Continuous lines are fits with the equation A_0*t^x where A_0 and x were adjusted. Two effects are induced by decreasing the Ga flux: the time delay to the growth occurrence increases and the rippening is longer. Note that only the ripening is influenced by the Ga flux, after reaching the linear growth mode the growth rate is the same for all samples. This fact points out the fundamental role of the Ga adatom diffusion occuring during the NWs growth (see also Songmuang and *al*., Appl. Phys. Lett. 91, (2007), 251902.

Structural investigation of silicon nanowires using GIXD and GISAXS: Evidence of complex saw-tooth faceting

T. David *, D. Buttard, T. Schülli, F. Dallhuin, P. Gentile
CEA-Grenoble, INAC

In many fields of physics today, there is a growing need for smaller and smaller structures. Microelectronics immediately comes to mind, but biology, optics and even mechanics have a similar need. This need has drawn the attention of many research people to nanostructures. Among these interesting structures, nanowires, grown by the vapor liquid solid (VLS) method, have attracted particular attention, one of the reasons being their many potential applications. Concerning the choice of material, silicon is extremely well-known and thus seems to be a good candidate. The first obvious use of such nanostructures would be in microelectronics, but nanowires could also be extremely useful in the field of sensors for instance. In order to use these basic structures, however, we need to understand their structural properties. A few studies have already shown interest in the structural and morphological properties of silicon nanowires grown by VLS, with the very small diameters (5–20 nm) attracting most attention. It seems that nanowires generally grow in epitaxy on the silicon substrate if the interface between the catalyst and the silicon is clean at the beginning of growth. In addition, 'Big' nanowires (with a diameter greater than 50 nm) appear to have six sides, one out of two presenting saw-tooth faceting, with the preferred growth direction being the (111) direction of the silicon crystal. In the case of smaller diameters, however, six faces also appear but the axis and the faces of the nanowire exhibit different directions. In order to investigate the crystalline nature and faceting of an assembly of small objects, X-rays are a very suitable tool. With regard to shape in particular, grazing incidence small-angle X-ray scattering (GISAXS) has already proved its efficiency in the study of silicon nanocrystals. We performed grazing incidence X-ray diffraction (GIXD) and GISAXS experiments on 'big' silicon nanowires (diameters from 50 to 500 nm) grown by VLS on (111)-oriented silicon substrate with a gold catalyst. Crystal orientation and structural properties of the nanowires were deduced from GIXD while GISAXS provided information about the shape of the nanowires, their faceting and the orientation of their facets.

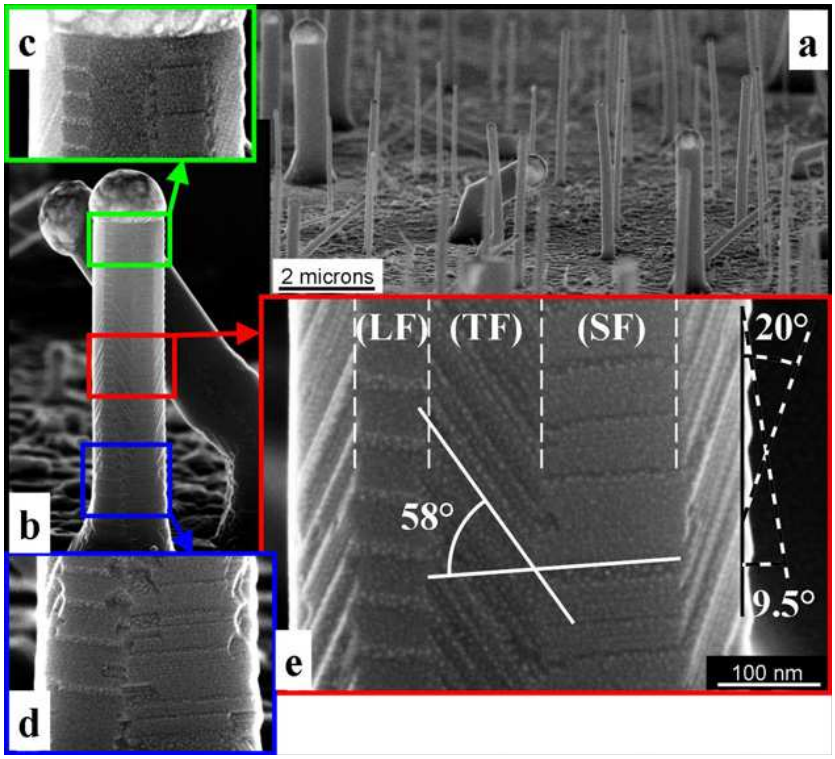

Fig. 1: SEM images of nanowires. (a) overall view, (b) single nanowire, (c), (d) and (e) detailed views from (b). Every face seems to be saw-tooth faceted with different types of facets oriented upwards. (SF) type faces have small upward-facing facets while (LF) type faces have large upward-facing facets. The edges of the hexagonal prism are truncated and the cross-section would thus be dodecagonal. These new faces are themselves finely faceted with tilted facets (TF), and appear wide at the top of the nanowire (c) and almost non-existent at the bottom (d).

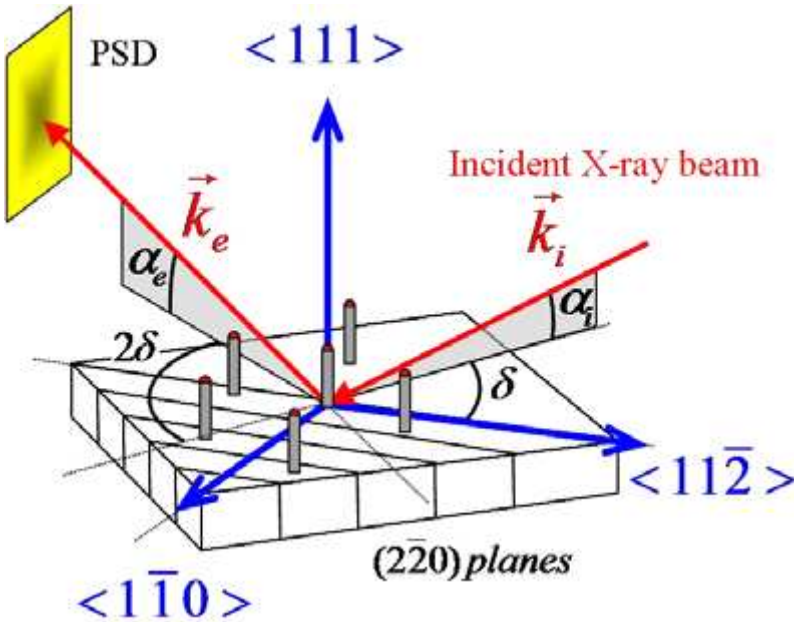

Fig. 2. Setup used for GIXD experiments.

Fig. 3a shows a profile of the diffracted intensity around the (220) reflection. We observe two diffraction peaks, the narrower (S) coming from the substrate and the broader (NW) from the wires, indicating that nanowires are single crystals and that their in-plane orientation is the same as the one of the substrate. Using Bragg's law we can estimate the lattice parameter a_{Si} and a_{nw},

respectively, of the substrate and the nanowires. We then deduce the lattice mismatch parameter $\Delta a/a = (a_{nw}-a_{Si})/a_{Si}$=-1.23 *$10^{-3}$ corresponding to a compression. Analysis of this strain is in progress but it can be tentatively explained by surface effects in the nanowires coming from a thin oxide shell. Fig. 3b shows a reciprocal space map of the diffracted intensity around the (220) peak of silicon. On this map, we see six diffusion streaks indicated by the dotted lines. These streaks are produced by vertical "planes". Consequently, they provide evidence of the hexagonal cross-section of the wires. The angle between two streaks is 60° and the directions of the six sides of the nanowires can be deduced from the directions of these streaks on the map. Thus, the directions of the six sides of the nanowires are <112> facets. Similarly, the directions of the edges between two faces are <110>. These results are consistent with previous electronic microscopy observations. As this map shows the scattered intensity coming from the entire population of nanowires illuminated by the beam, we can be sure that these nanowires are all in epitaxy with the substrate and have the same in-plane orientation. Otherwise the map would show an arc following a Debye–Scherrer ring. The same experiment was performed on another sample obtained
after a shorter period of growth, resulting in nanowires at the very beginning of their growth. The corresponding map (not shown) has a round shape without streaks, showing that the hexagon faces have not yet been formed.

Fig. 4a shows a GISAXS image obtained with the incident beam along the <110> direction (i.e., incoming on the nanowires through an edge), while Fig. 4b shows the same image obtained with the incident beam along the <112> direction. The coordinates on the image correspond to the in-plane (q_x) and the out-of-plane (q_z) scattering vector. As there is no periodic vertical rod, no lateral periodicity of the wires is observed. However we can observe several tilted rods on the left and right of the image. As the rods are tilted, the facets do not correspond to the principal faces of the hexagonal cross-section of the wires shown earlier. These rods are produced by supplementary facets on the principal faces. This is consistent with the saw-tooth faceting observed earlier. By measuring the tilt angle we can estimate the orientation of the facets. Finally, on all GISAXS measurements, and especially in Fig. 4a, a splitting of the scattered streak may be observed. This phenomenon is due to multiple scattering effects and has already been investigated.

The diffuse streaks produced by facets are schematically represented in Fig. 5. The incident X-ray beam is scattered by facets and the scattering vector **q** normal to these facets is located by angles α_R and φ. The axis x and z correspond to the plane of the CCD camera (respectively the horizontal and the wires axes), while y is the X-ray beam direction. In the plane of the camera, the projection of the vector **q** has a measured angle α_f from the vertical. Depending on the facet orientation in relation to the CCD plane φ can take several values. If the facet is normal to the CCD plane φ =0, so $\mathbf{q}_{xy}$
and **q** are in the CCD plane and no correction is needed ($\alpha_R=\alpha_M$). But if $\varphi \neq 0$, $\mathbf{q}_{xy}$ and **q** are out of the CCD plane and a correction is needed as $\tan\alpha_R = \tan\alpha_M/\cos\varphi$. It is important to note that the visibility of streaks on the GISAXS image decreases quickly when φ increases. Facet indexation with the corrected angle is analysed below.

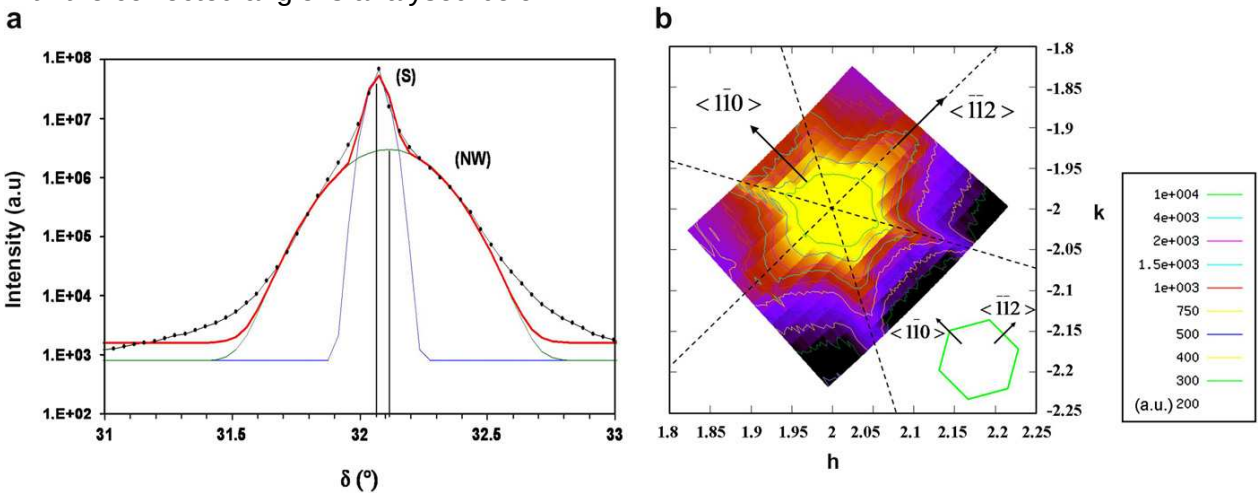

Fig. 3. (a) Experimental profile of diffraction (dotted line) close to the (220) peak of silicon with peak (S) from the substrate and peak (NW) from the nanowires. The solid lines correspond to fits for the center of the

peaks in order to accurately determine the maximum peak position, (b) Reciprocal space map of scattered intensity (arbitrary units) around the (2 20) peak of silicon. h and k are the reciprocal space coordinates. There are six diffusion streaks spread regularly every 60° around the peak, providing evidence of the hexagonal cross-section of the nanowires and thus allowing determination of facets direction.

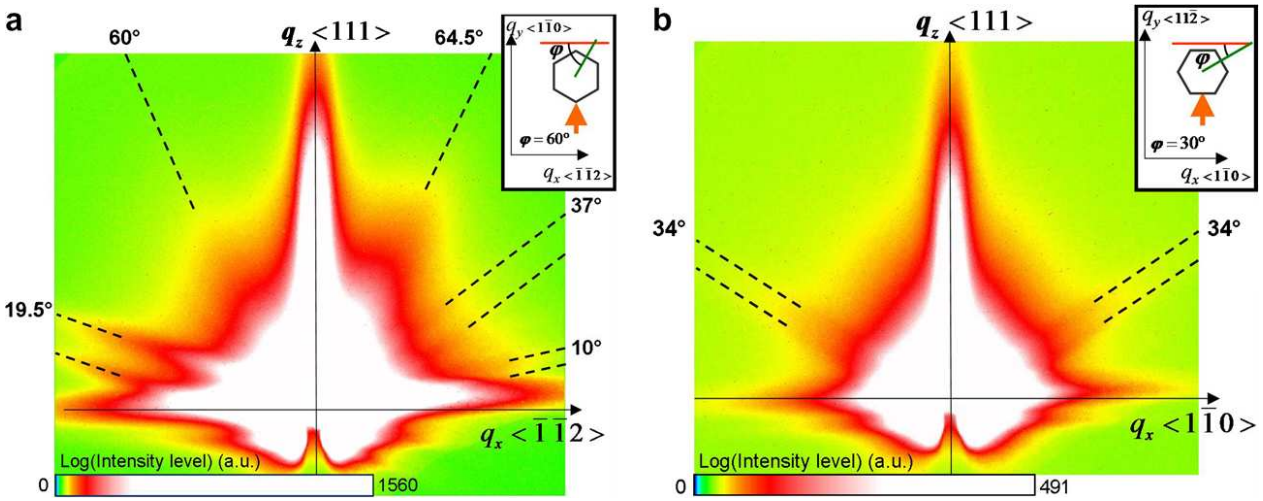

Fig. 4. GISAXS image obtained along (a) the <110> direction and (b) the <112> direction. We see scattering streaks tilted in relation to the vertical q_z direction, produced by different facet families. The angles indicated correspond to the measured angles (90°- α_M) and φ are defined in Fig. 5. In image (a) asymmetry between the left and right is noticeable, while image (b) is symmetrical. Intensity is given in a logarithmic scale. Inserts: schematic top view of a nanowire cross-section.

The asymmetry in Fig. 4a reflects the trigonal character of the nanowires. This is not in contradiction with the Friedel rule of centrosymmetry nor with the six symmetrical diffuse scattering streaks around the (220) reflection of silicon obtained in Fig. 3b. Indeed, in GISAXS the full inversion symmetry rule is eliminated. This apparent trigonal character corroborate the observations of Ross et al. which show that only one out of two sides are saw-tooth faceted. However, as shown in Fig. 1b–e, our SEM observations are not very consistent with the simple faceting model usually proposed. Indeed, we observe saw-tooth faceting on each side of the nanowire. For large-diameter wires (i.e. diameter larger than 200 nm) the hexagonal cross-section is replaced by a dodecagonal section. It seems that the six additional faces are wider at the top (Fig. 1c), while almost non-existent at the bottom (Fig. 1d). All these observations lead us to reconsider the nanowire facet model and to propose a new one, as shown in Fig. 6. In Fig. 6a we can observe the dodecagonal section. The twelve faces are all sawtooth faceted and distributed in three families. The (LF) family corresponds to large upward-oriented facets as indicated in Fig. 6b and the (SF) family corresponds to small upward-oriented facets. The two opposite faces are centrosymetric. This is the reason why the GISAXS image in Fig. 4a is asymmetric. This is perfectly consistent with the trigonal character of the nanowires. For large diameter nanowires (diameter larger than 200 nm), six additional faces appear as a result of the truncation of the hexagon edge, producing the (TF) family corresponding to tilted saw-tooth faceting. The GISAXS image is consistent with this explanation, as shown in Fig. 7. On the GISAXS image in Fig. 7, the 'large' facets produce a streak at 10°≈(90°- α_{Mright}) = (90-α_R) n the right of the image and one at 19:5°≈(90°- α_{Mleft}) on the left tanα_{Mleft}= tan(α_R) *cos60°. However, the streak at 19.5° should be much less intense than the one at 10° because of th e in-plane angle correction explained earlier. In the same way, the 'small' facets would produce streaks at 19.5° (intense) and 37° (weak). Combining the two, we have one superimposed streak at 19.5° on the left of the image and two distinct streaks at 10° and 37° on the right. As th e streak at 37° corresponds to a diffraction vector outside the detector plane (φ ≠0), its intensity is very weak compared to the two other at 10° and 19.5°. This is exactly what we observe in Figs. 4a and 7 with an acceptable error of 1°. The SEM image in Fig. 1 corresponds well with this explanation since we measure an angle of about 9.5° with respect to the vertical for the large facets and 20° for the small ones. It is interesting to not e that the angles determined locally by Ross et al. in using SEM measure 11.2° and 23.3° values,

which are close to ours. Similar results have also been reported with TEM observations. In terms of direction, the facets tilted at 19.5° correspond to <111> planes and those tilted at 10° correspond to <113> planes. Finally, we must explain the existence of the diffuse streaks at approximately 60° in Fig. 4a and at approximately 34° in Fig. 4b.

For big wires with a diameter larger than 200 nm, tilted facets appear, as we can see in Fig. 1e, at an angle with respect to the horizontal $\omega \approx 58°$. By applying corrections, we can find the approximate orientation of the diffuse streaks in Fig. 4a and b.

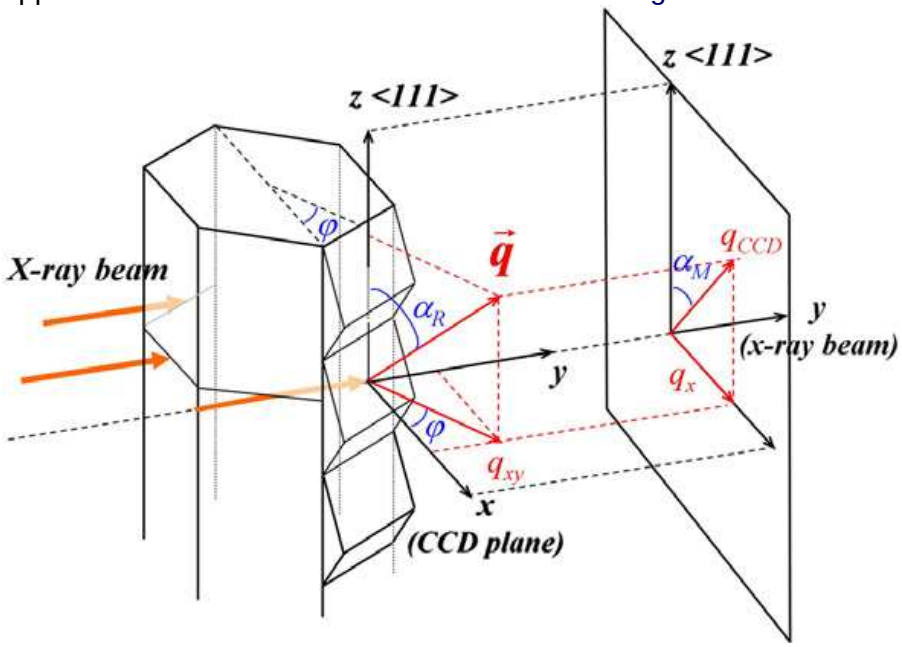

*Fig. 5. Schematic representation of the faceted wire and the CCD camera plane. **q** is the scattering vector, x; the horizontal axis in the CCD plane, y; the X-ray beam direction, z; the wire axis, α_R and α_M, respectively the real and measured angles between **q** and the vertical and φ the angle between the normal of the facet and the CCD plane.*

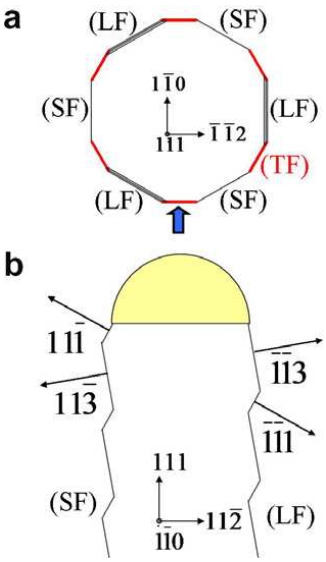

Fig. 6. Model of the nanowires. (a) The nanowire cross-section has the six usual faces, all saw-tooth faceted. Half of them (LF) present the large upward-facing facets and the other half (SF) present the small upward-facing facets. The six additional faces truncating the edges are represented in red and marked (TF). They also exhibit a saw-tooth faceting but with tilted facets. (b) shows a view in the vertical plane along the direction indicated by the blue arrow in (a). The two opposite faces are of different type, one being (LF) and the other (SF). This is the reason why the GISAXS image is asymmetric.

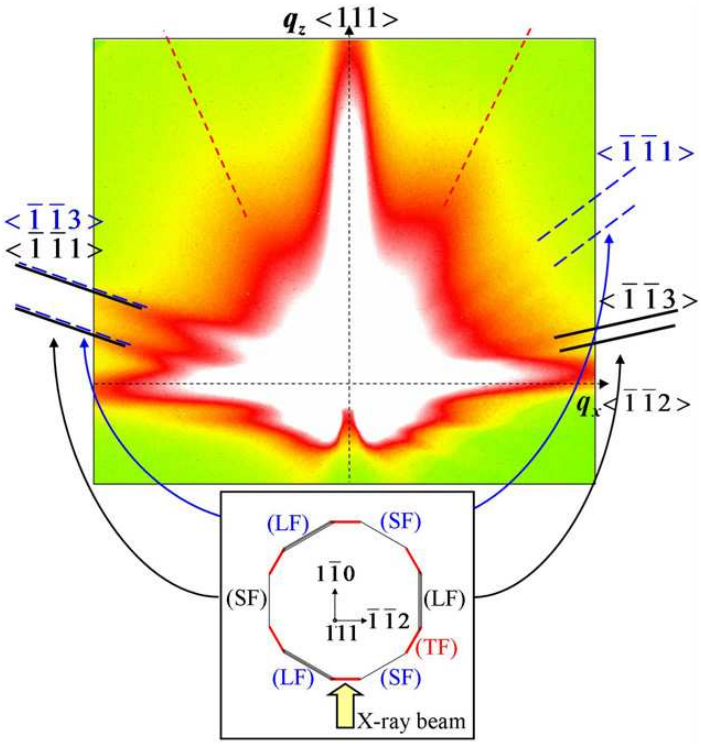

Fig. 7. Correspondence between the streaks visible on the GISAXS image and the different types of facets. The two streaks marked with black solid lines correspond to the facets whose normal is in the detector plane (φ =0). These facets are present on two of the faces of types (LF) and (SF). The two streaks marked with large blue dashed lines correspond to the same facets but with (φ ≠0), present on the other faces of type (LF) and (SF). Finally, the two streaks marked with small red dashed lines probably correspond to the other tilted facets present on the faces of type (TF). These faces are only present on nanowires whose diameters are larger than 200 nm. The intensity is given in a logarithmic scale.

In situ nucleation of Si-wires, MBE growth and liquid Au-catalysts

T. U. Schülli, G. Renaud
CEA-Grenoble, INAC

Following first publications on the x-ray investigation of nanowires, fundamental questions on their growth as the formation of defects or twinning, maybe addressed by *in situ* investigation of early nucleation stages. We have followed the deposition of a thin Au film and the formation of catalytic droplets during annealing, as well as the nucleation of si nanowires by subsequent MBE deposition of Si.

After the deposition of a thin Au-film on Si(111), its crystallinity was studied and a preferential orientation, parallel to the cubic axes of Si was found. Upon annealing, islands are formed prior to melting. This could be followed *in situ* by monitoring the width of the Au(113) Bragg peak, as shown in Fig. 1: for a thin layer, and scanning in q_z direction in reciprocal space (here q_z is parallel to the substrate's surface normal), broad size oscillations are visible. Their spacing can be attributed to the 1.8 nm thick film as deposited at room-temperature. Upon annealing at 350°C, Islands were formed, witnessed by the narrowing of the Au (113) peak as visible in Fig. 1 (b). At 360°C, all crystalline signals from Au disappear a nd a eutectic AuSi liquid is formed.

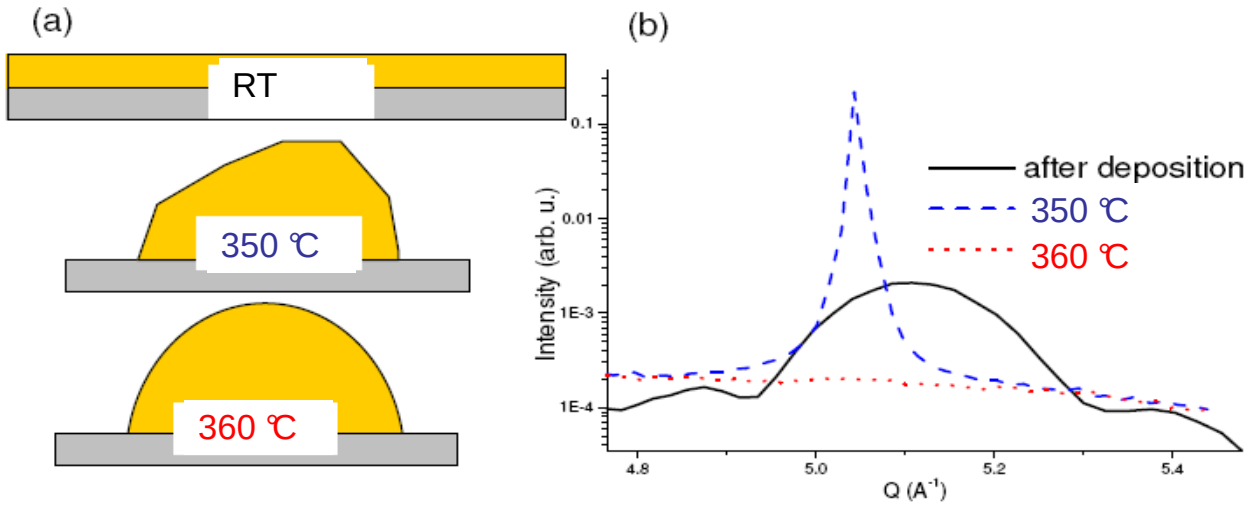

Figure 1: Growth of eutectic catalysts, here for the system Au-Si. A 1.5 nm thin Au film is deposited in (a), the black curve in (b) shows its size oscillations corresponding to its thickness. Annealing at 350℃ leads to islands (dashed blue curve in (b)). At 360℃ the island transforms into a $Au_{80}Si_{20}$ liquid droplet.

Figure 2 shows a secondary electron microscopy (SEM) of a Au-island produced by this method at the SUV endstation. In its liquid state, at 550℃ it was exposed to a MBE Si-flux, and the nucleation and growth of nanowires was followed *in situ*. A reciprocal space map of the Si(220) after the growth is shown in Fig. 3. The hexagonal cross section of the wire is visible in the form of six facet streaks.

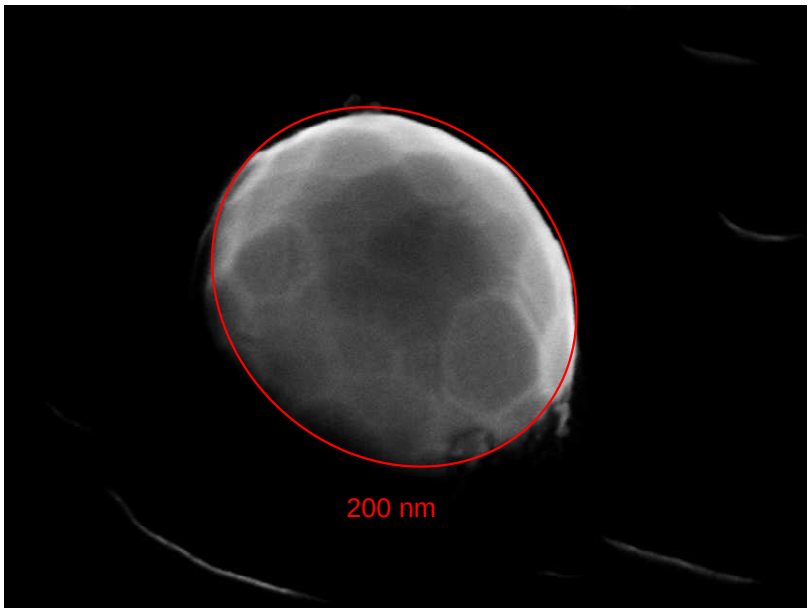

Figure 2: Au island formed on a Si(111) surface after annealing

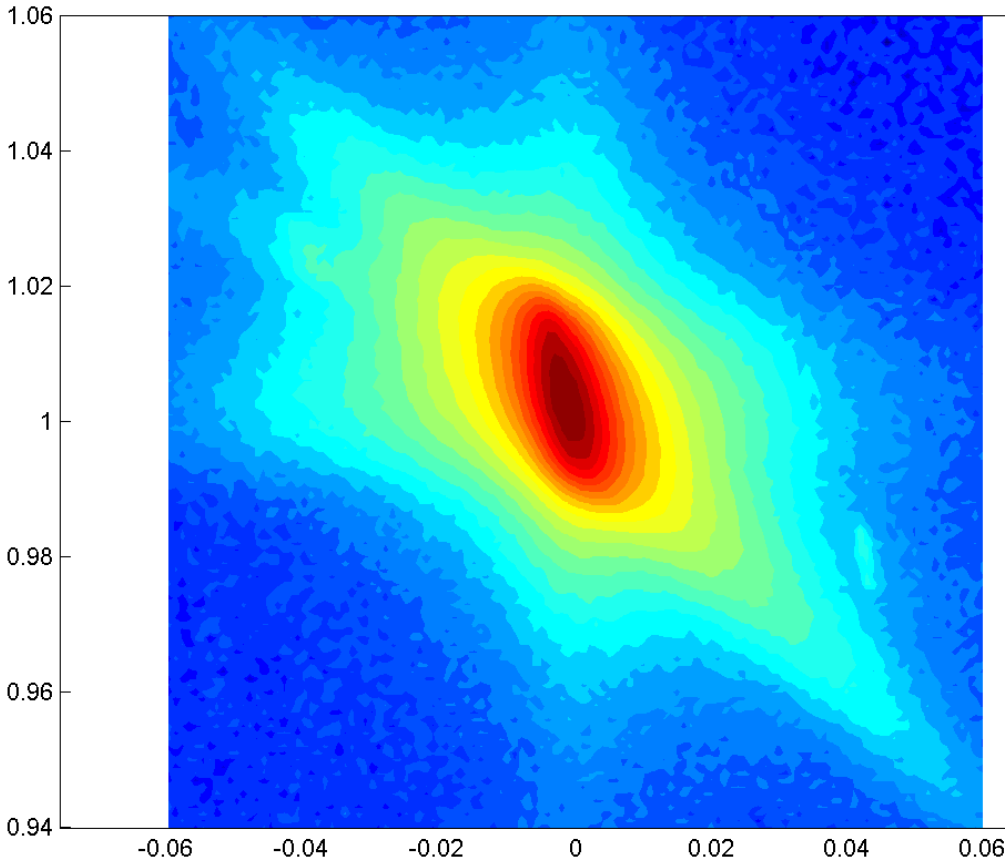

Figure 3: in-plane reciprocal space map of the Si(220) reflection of an in situ MBE grown nanowire.

Surface induced giant supercooling in AuSi catalysts

T. U. Schulli, R. Daudin, G. Renaud, A. Vaysset, A. Pasturel

CEA-Grenoble, INAC

The rapidly developing field of vertical Semiconductor nanowire growth makes use of metal catalysts combined with chemical vapour deposition. It is essentially the formation of low temperature eutectics between semiconductors and metal that drives the nucleation and growth of these structures. For Silicon nanowires, previously deposited metallic nanoparticles, Au as the most commonly used, serve as catalysts and offer unique growth conditions and restrictions due to their capacity of transporting Si even at low temperatures in the eutectic liquid $Au_{80}Si_{20}$. As research is focusing on alternative catalysts, an atomistic understanding of the outstanding transport properties of Si in AuSi even at massive Si overpressure in the growth chamber remains unresolved.

We have investigated the melting behavior and the liquid state of these AuSi droplets on a Si(111) surface by Grazing Incidence X-ray Scattering on the BM32 beamline. It is found that in case of the formation of a complex Si(111)-(6x6) surface reconstruction, supercooling down to 120 K below the melting point (of only 636 K) is observed. A detailed analysis of the surface structure shows that more then 50 % of the surface atoms form pentagonal structures, incompatible with the fcc solid state of Au, but corresponding to the theoretical atomic arrangement and distances present in a calculated icosahedral AuSi “molecule” as it could exist in a liquid. Modification of the thermal history leaves a $3\sqrt{3}x3\sqrt{3}R30°$ surface reconstruction and does not reveal the same supercooling effect. We state that this is the first observation of stabilization of a liquid in interaction with a surface. It confirms the theory that supercooling of metals is induced by local five fold symmetry. Figure 1 (a) shows the atomic positions of the Au atoms in the surface unit-cell obtained from the analysis of 976 measured reconstruction peak intensities. The red lines are a guide to the eye for the deformed pentagonal atomic arrangement of Au atoms around a threefold

center. The atomic distance of the Au atoms in these pentagons is 0.29 nm, corresponding to the atomic distances observed in *e.g.* an icosahedral $Au_{12}Si$ molecule. Our findings are of fundamental interest in the understanding of liquid-solid interaction, as well as on the stabilities of liquids and the local arrangement of binary liquids. The solid-liquid transition could be observed by the appearance/disappearance of Bragg peaks of the Au fcc structure as well as by the observation of the liquid structure factor. Figure 1(b) shows the hysteresis opening due to the supercooling of the melt. Depending on the interface structure, the solidification temperatures differ by 40 K.

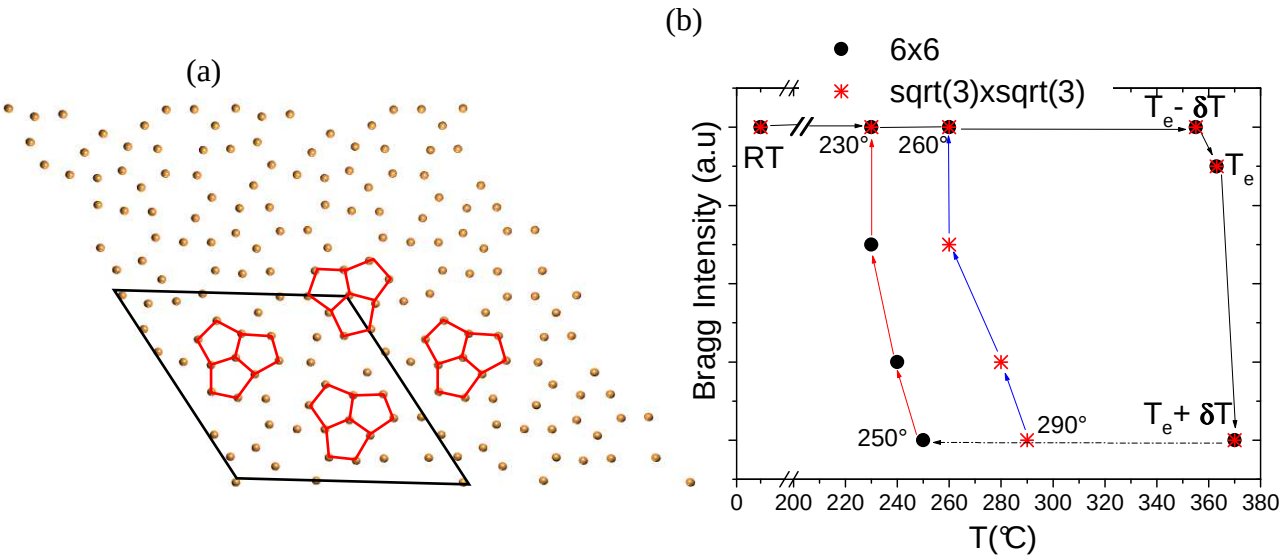

Fig. 1(a): Arrangement of the Au atoms on the Si(111) 6x6 reconstructed surface. The hexagonal unit cell with a=2.3 nm is indicated in black; in red: pentagonal arrangement of Au atoms around a threefold centre.
Fig. 1(b): Hysteresis of the solid-liquid-solid (s-l-s) transitions of the AuSi catalysts on the Si(111)6x6 and 3√3x3√3R30° surfaces . Note that the transition is accomp anied by a chemical mixing (s-l) and de-mixing (l-s).

Investigations of GeMn on Ge(001)

V. Favre-Nicolin, S. Tardif, A. Barski, M. Jamet, T. Devillers, C. Porret, T. Schülli
CEA-Grenoble, INAC

Scientific background:

The realization of carrier-induced ferromagnetism, with possible applications in rapidly developing areas such as "spintronics", has boosted the interest in the study of semiconducting materials that show ferromagnetism upon transition-metal doping, known as diluted magnetic semiconductors (DMS). The manipulation of both the electronic spin and the electronic charge requires the development of new DMS with a large density of carriers, which maintain their ferromagnetic behavior at high temperature - close to room temperature. Despite several encouraging results, DMS materials are still struggling to reliably achieve the desired high Curie temperature T_c. Up to now, semiconductor spintronics has been mainly devised based on diluted magnetic semiconductors, in which magnetic atoms randomly substitute the semiconductor atoms. DMS's containing secondary phases (metallic inclusions, semiconducting ferromagnetic phase or simply concentration modulation) were seldom studied and usually not well controlled. The presence of secondary phases or inhomogeneities could increase the critical temperature, or enhance the magnetoresistance by multiplying the number of interfaces for spin scattering.

Samples grown and studied:

During this experiment a total of 5 samples were grown in-situ in the adjoined MBE chamber, varying the substrate (Ge or GaAs), the Mn concentration (from 6% to 15% Mn). A few samples

were studied by X-ray scattering before and after capping with amorphous silicon. Another sample, previously studied by XMCD, was also studied.

The growth conditions were chosen so as to minimize the formation of Ge3Mn5 clusters, i.e. at a moderate temperature.

X-ray measurements:

All X-ray measurements were done around E=11 keV, either right below the Ge K-edge, or around it for anomalous diffraction. For the GaAs samples constant-wavelength measurements were carried out below the Ga K-edge. The incident angle was (except for some GISAXS images, see below) set to the experimentally found critical angle, in order to maximize the scattered intensity.

For all samples the following measurements were made :

-GISAXS images taken along the (110) and (100) azimuths, for several incident angles (0.15°, 0.25° and 0.35°)

-One large in-plane X-ray scattering map including the (220) and (400) reflections

-Several detailed scattering map around possible in-plane reflections: (200), (400), (620). These were collected as “medium” (reciprocal lattice range ±0.2) and “fine” maps (range ±0.02) around the main Bragg peaks.

-Fine 1D angular and radial scans around the (200), (400), (620) reflections

Anomalous diffraction measurements were carried out only for the GaAs samples, in order to avoid the anomalous contribution from the substrate.

Preliminary results:

The maps collected on the different samples all include the same basic features : a diffusion line between the (220) and (400) reflections (see figure 1), some diffuse scattering around (0.6 2.6 0), and a distinctive diffuse scattering around all main Bragg peaks.

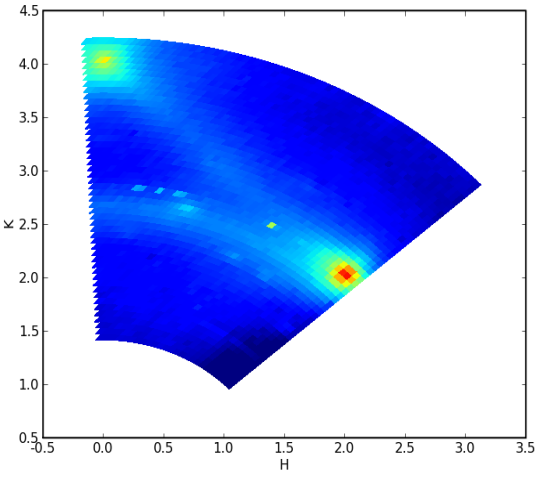

Figure 2: Large grazing incidence X-ray scattering map

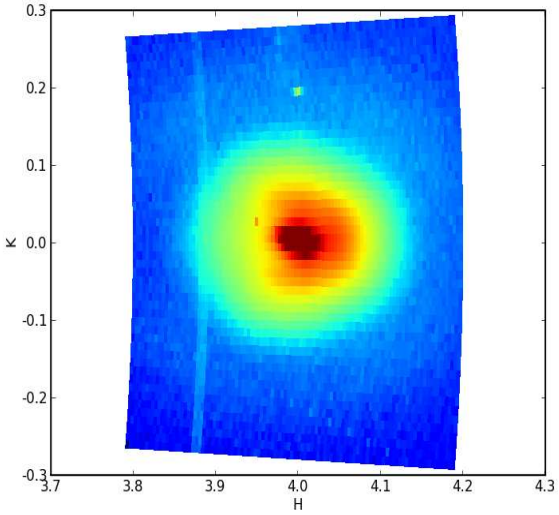

Figure 1: grazing-incidence X-ray scattering map around the (400) reflection (logarithmic colour scale). Note the shape of the diffuse scattering, which depends on the sample growth conditions.

The most interesting results of this experiment are the variation in shape and intensity of this diffuse scattering around the main Bragg peaks, which depend on the sample growth conditions. We are in the process of reproducing this diffuse scattering by taking into account the size of the nanocolumns, their internal structure (strain, composition,..), and the deformation of the surrounding Ge matrix.

Enhanced relaxation and intermixing in Ge islands grown on pit-patterned Si(001) substrates

T.U. Schülli, M.I. Richard, A. Malachias, G. Renaud, F. Uhlik, G. Vastola, F. Montalenti, G. Chen, L. Miglio, F. Schäffler, G. Bauer

Ordering, shape and size uniformity of epitaxial Ge (or SiGe) islands on Si(001) is very important whenever microelectronic applications based on such nanostructures are concerned . Island formation is known to follow the Stranski-Krastanow (SK) growth mode, allowing for partial elastic-energy relaxation. Since on flat substrates islands tend to nucleate randomly, substrate pre-patterning prior to growth can be used to achieve controlled positioning. A high degree of ordering was indeed obtained in, exploiting a suitably pit-patterned substrate. Remarkably, patterning was also shown to increase size uniformity, possibly because of a more regular distribution of capture areas. The possibility of controlling also the relaxation level of the islands by growth on patterned substrates appears extremely intriguing. We show that the presence of pits influences not only the average relaxation, but also the distribution of Ge within the islands. Pit-patterned substrates were prepared by lithography. 7 ML of Ge were deposited at 620℃ on a Si(001) substrate with a 900x900 μm² part of it being patterned with pits at a periodic spacing of 495 nm. The growth of a thick Si buffer prior to Ge-deposition leaves a periodically facetted surface with flat {1 1 10} pits with the shape of downward pyramids. AFM analysis showed that Ge islands nucleate at the bottom of these pits and form dome-shaped islands with identical facets as on the nominal part of the substrate. The average island density per surface unit area is 5 μm^{-2} for the patterned part and 20 μm^{-2} for the nominal one. The domes on the patterned (nominal) part have an average height of 28 nm (23 nm) and a diameter of 130 nm (110 nm).

The sample was then transferred under N_2 atmosphere and introduced in the UHV chamber at BM32. The islands were characterized in grazing incidence x-ray diffraction (GIXD) at an x-ray energy of 11.04 keV. The incident beam and the collimation on the detection side were translated on the sample in order to select between the different regions. Reciprocal space maps in the vicinity of the 400 Bragg reflection were recorded as shown in Fig. 1 (a) and (b) together with corresponding AFM images as insets. The intensity distribution along the radial direction clearly extends to higher lattice parametres for the patterned region. In Fig. 2 (a) radial scans (corresponding to the full or dotted lines in Fig.1 (a) and (b) are plotted as a function of the lattice parameter, inferred from the radial momentum transfer. It is clearly visible that the nominal sample has its main lattice relaxation at lattice parameters around 5.46 Å whereas for the patterned part, the lattice-parameters are streched over a longer area in reciprocal space, showing a maximum at about 5.51 Å.

To better understand the reported difference, we related the lattice-parameter results to the local Ge content inside the islands by exploiting anomalous x-ray scattering. We recall that by monitoring the variation of the scattered intensity when varying the x-ray energy in the vicinity of the Ge K-edge (E_e=11.103 keV) at a fixed momentum transfer Q, the corresponding average Ge concentration can be determined, so that lattice parameter versus Ge content (c) data are extracted, basically without any model assumption. A first key result came out: both for the nominal and for the pit-patterned region, the average Ge content turned out to be ~60% in both cases: the presence of the pit does not influence neither the shape (dome) nor the relative amount of Si and Ge atoms within the island. Let us see where, instead, differences exist. Figure 2 (b) shows Ge-concentration vs. the in-plane lattice parameter $a_{||}$ for the nominal (full lines) and the patterned region (dashed lines). A qualitative observation can be immediately made. By assuming the usual base-to-top lattice relaxation within islands, the flatness of the dashed curve indicates more uniform alloying within the pits in comparison to the nominal case. A possible explanation of this different behavior will be given after completing the presentation of the results. More insights can indeed be gained by extracting the actual 3D Ge distribution and the elastic-energy profile. Over the last ten years, x-ray methods have been developed, coupling lattice parameter with lateral size and chemical composition of an object, reconstructing a concentration profile inside nanostructures.

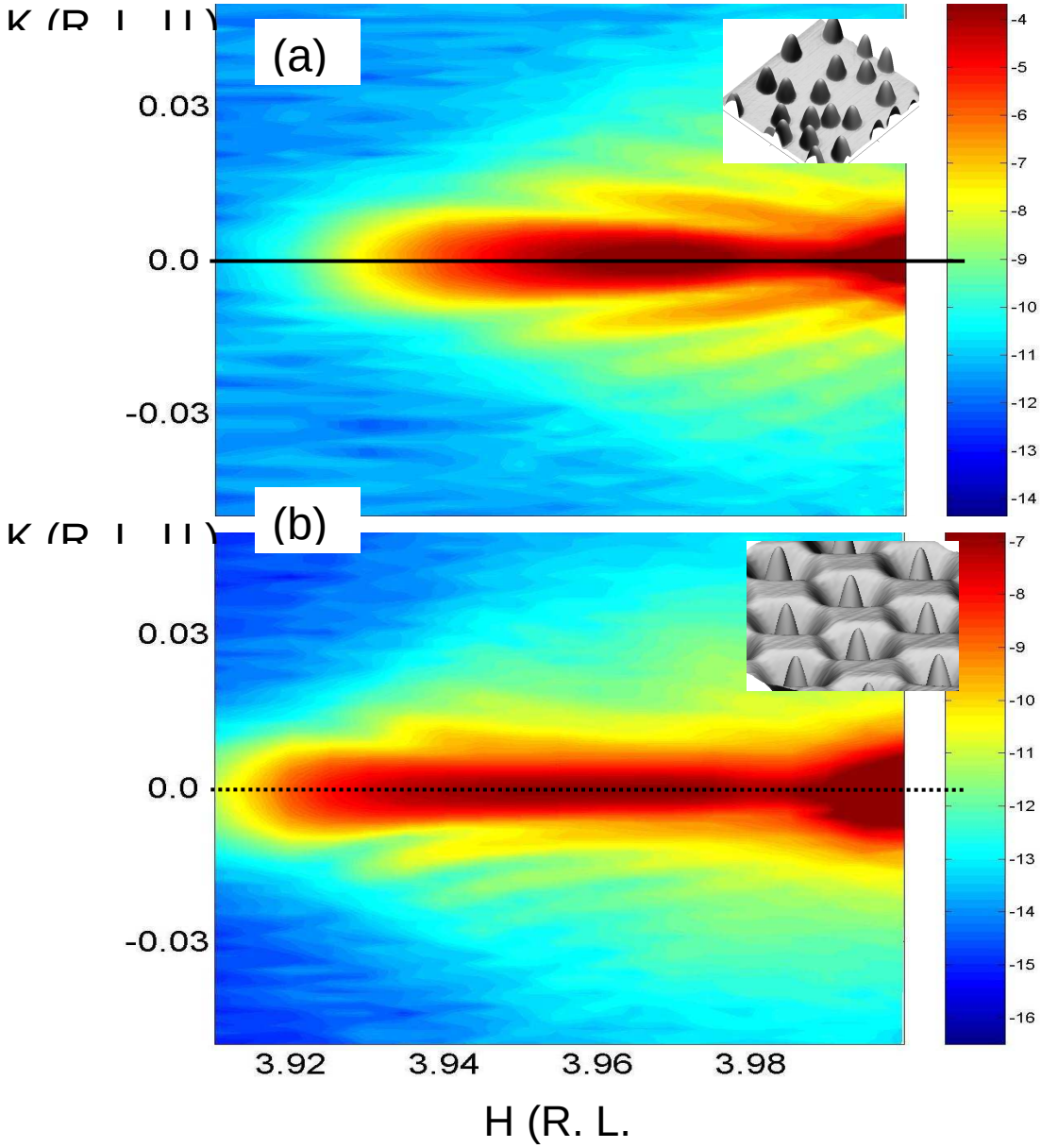

FIG. 1: (a) Reciprocal space map around the 400 Bragg reflection for the SK-grown sample on the nominal part. (b) The same region of reciprocal space shown in (a) but for the Ge-islands grown on the patterned part.

These methods are limited however by model assumptions concerning the shape of the considered iso-strain regions. Instead, we have used a novel fitting procedure exploiting a FEM-based treatment of non-uniform concentration profiles, allowing us to determine the local Ge content without any constraint. After the island and substrate geometry is created based on AFM images, non-uniform concentration values are assigned on a discrete mesh. The elastic problem is then solved exploiting linear interpolation, $(c,a_{||})$ data are extracted, and the statistical χ^2 is evaluated by comparison with the corresponding x-rays data. Using an iterative procedure based on local concentration exchanges preserving the assigned experimental average concentration value, χ^2 is minimized. It is important to emphasize that particular care is required in assigning the correct statistical weight to the data. During the fit, indeed, $(c, a_{||})$ pairs were computed not only from the island interior, but also from a surrounding region in the substrate with a lateral extension inferred from the experimental island density, and a depth of 12nm, i.e. the estimated penetration depth of the x-rays in our set-up. This allowed us to filter out from the experimental data the substrate contribution which, as shown in Fig. 2(c) for the nominal case, causes a sudden drop of the average Ge content at low lattice parameters, hiding important data coming from the island interior. Another difficulty stems in the vanishing experimental scattering volume (see Fig. 2(c)) of

the regions with lattice parameter close to bulk Ge.

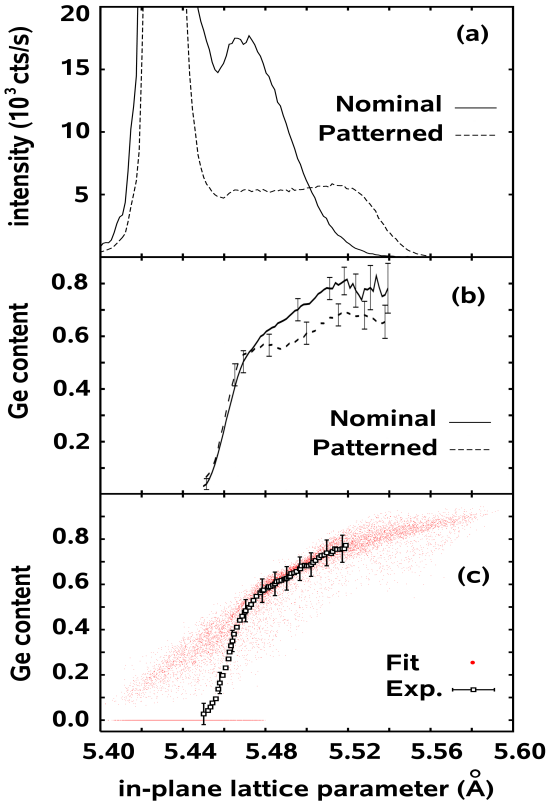

FIG. 2: (a) Radial intensity distribution as a function of lattice parameter for Ge-islands grown on the nominal part (full line) and on the prepartterned part (dashed line). (b) Germanium concentration inside the islands as a function of lattice parameter for growth on the nominal (full line) and on the patterned part (dashed line). (c) Experimental raw data, and fitted data after proper separation of the Si substrate contribution (nominal case).

In the fit their concentration value was extrapolated from experiments, assigning a large error bar in order not to bias the region where real data were present. Finally, a satisfactory fit (which required ≈10^4 iterations) is obtained, the full solution of the elastic problem being required at each step.

The 3D compositional maps for the nominal and the patterned substrate corresponding to our theoretical best fit are displayed in Fig. 3(a)-(d) together with their horizontally-averaged values (Fig. 3(e)), while the elastic energy per atom is reported in Fig. 3(f), where a comparison with the uniform composition case is also shown. In the nominal case - Fig. 3(a) and (b), an almost Si-pure region is found close to the base edges, a result fully compatible with selective-etching data. From Fig. 3(c) and (d) one sees that Si enrichment at the base is less evident in the pit case where the overall Ge distribution is more uniform, but for more localized irregularities. This is particularly evident from the horizontally averaged Ge content values displayed in Fig. 3(e). The above observations can be justified using both thermodynamic and kinetic arguments. The edges of the islands grown on flat substrates are the most compressed regions in case a uniform Ge distribution is considered, so that replacing Ge with smaller Si atoms produces significant relaxation. By comparing the energy per atom in flat vs. pit-patterned substrates (Fig. 3(f)) in the case of a uniform distribution, one sees that the driving force for Si segregation at the island base is weaker in pits, since the elastic-energy difference between base and top is smaller.

If pit pre-patterning is already seen as a powerful tool to control positioning and homogeneity of heteroepitaxial islands, in this Letter we have shown that it also allows one to control elastic-energy release. This opens up the possibility of tuning strain in the islands by selecting the shape of the pits in order to grow islands with the desired degree of relaxation. The kinetics of Si supply, however, seems to be also influenced by the presence of the pit, calling for further investigations for achieving full control.

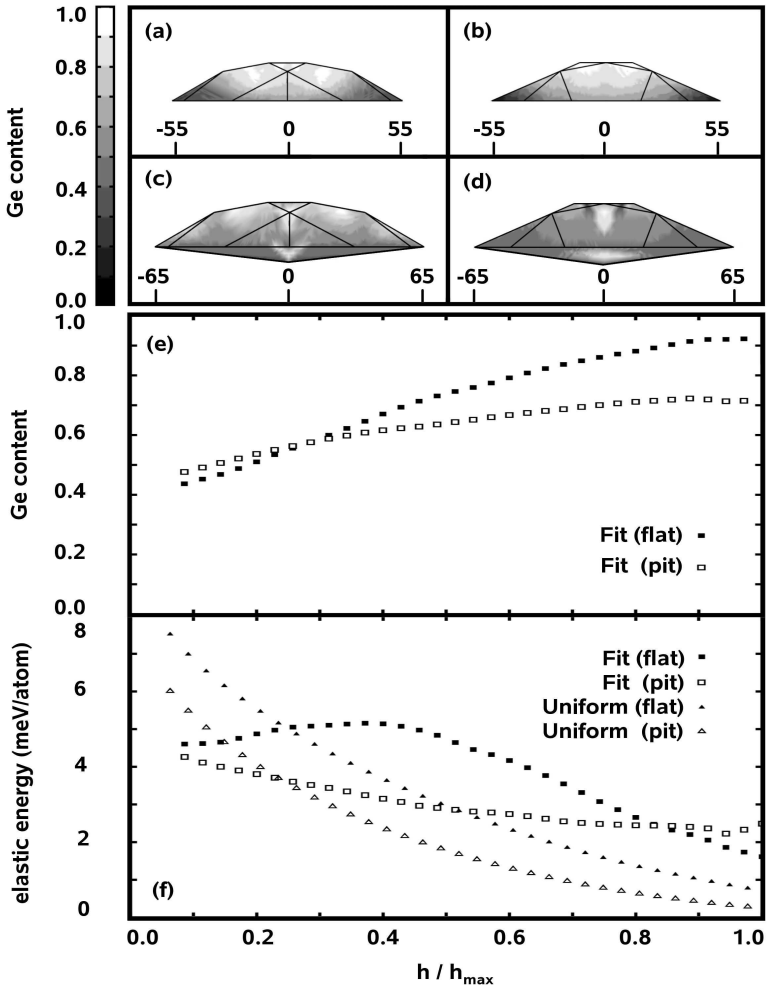

FIG. 3: Cross-section map of the 3D-reconstructed Ge content profile for islands grown on nominal (a-b) and patterned (cd) samples. Sections are showed along the [100] (a,c) and the [110] (b,d) crystallographic directions. Islands lateral size is shown in nm. Panel (e) displays the average Ge content as a function of height. Panel (f) reports for the elastic energy profile correspoding to the fitted Ge distribution on flat (filled box) and patterned (empty box) substrates. Plots made for the case of uniform concentration are analogously displayed for flat (filled triangles) and pit (empty triangles) case.

Instrumental refurbishment project for 2008/9 : New BM32 hutch and integration of a CBE gas injection system

The refurbishment project presented in last years report, supported by the RTRA **« Nanosciences aux limites de la nanoélectronique »** is currently under realisation. The isntrument is currently closed down (since October 8th) until the end of February 2009 where the new lead hutch and lab space will be finished. The integration of the gas injection system to combine solid source and gas source MBE growth will follow in 2009.

Plan of the new experimental hutch:

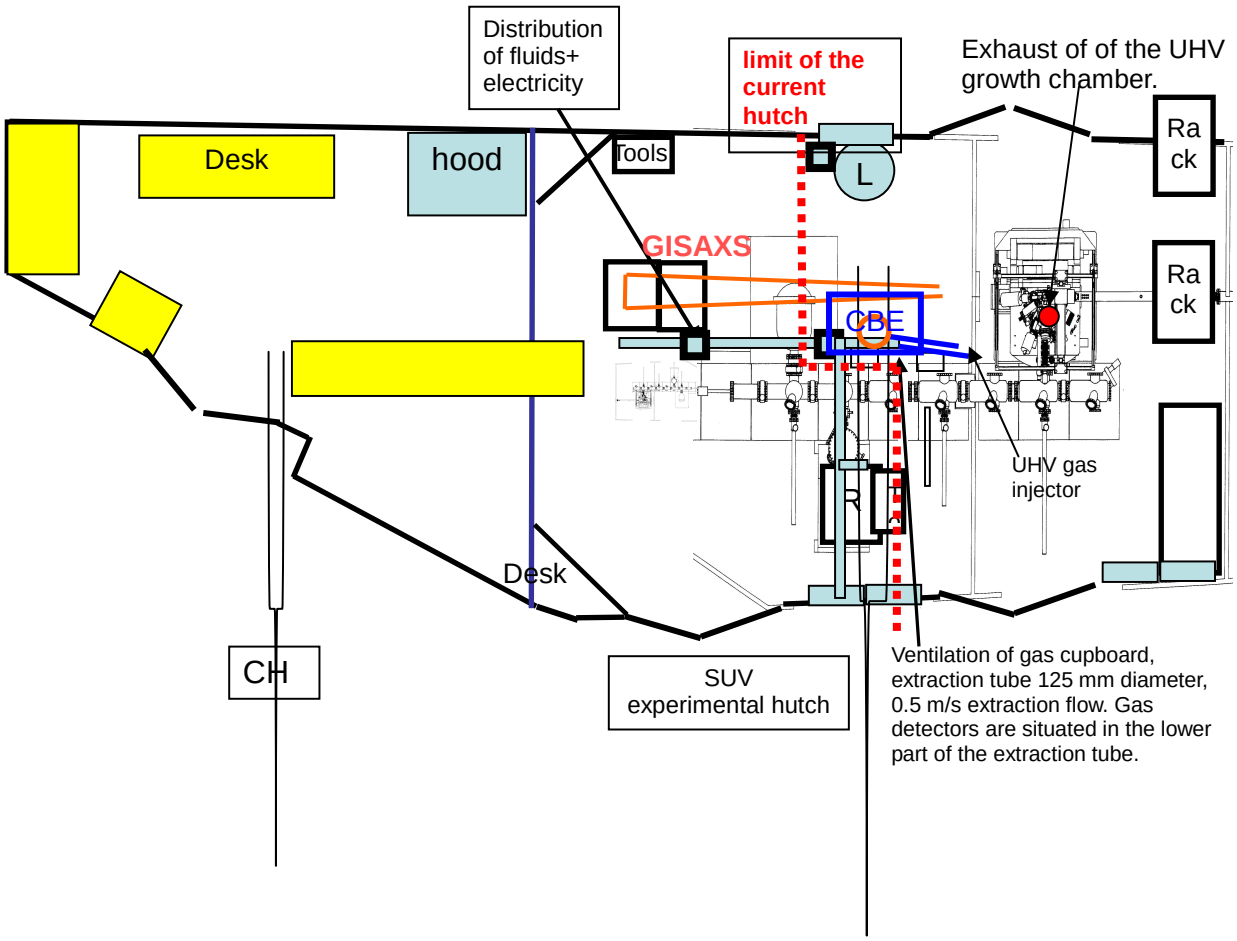

The increase of the possible sample-detector distance will permit higher resolution in GISAXS and diffraction. The mounting of bulky 1D and 2D detectors on the diffractometer arm will be possible.

Liste des publications résultant de mesures sur la ligne IF publiés en 2007-2008 :

( ) : nombre de citation au 15 Octobre 2008 [ ] : facteur d'impact (selon web of science)

2008

Publications:

[26.4] *"Shape Changes of Supported Rh Nanoparticles During Oxidation and Reduction Cycles"*,
P. NOLTE, A. STIERLE, N. Y. JIN-PHILLIPP, N. KASPER, T. U. SCHULLI, H. DOSCH,
Science **321**, 1654 (2008).

[6.94] *"Depth Magnetization Profile of a Perpendicular Exchange Coupled System by Soft X-ray Resonant Magnetic Reflectivity",*
J. M. TONNERRE, M. DE SANTIS, S. GRENIER, H.C.N. TOLENTINO, V. LANGLAIS, E. BONTEMPI, M. GARCIA-FERNANDEZ, AND U. STAUB
Phys. Rev. Lett. **100**, 157202 (2008)

[6.94] "*Controlling structure and morphology of CoPt nanoparticles through dynamical or static coalescence effects",*
J. PENUELAS, P. ANDREAZZA, C. ANDREAZZA-VIGNOLLE, H.C.N. TOLENTINO, M. DE SANTIS, AND C. MOTTET
Phys. Rev. Lett. **100**, 115502 (2008)

[3.6] "*Germanium oxynitride (GeOxNy) as a back interface passivation layer for Germanium-on-insulator substrates"*
T. SIGNAMARCHEIX, F. ALLIBERT, F. LETERTRE, T. CHEVOLLEAU, L. SANCHEZ, E. AUGENDRE, C. DEGUET, H. MORICEAU, L. CLAVELIER, F. RIEUTORD
Appl. Phys. Lett. **93**(2), 022109 (2008)

[3.6] *"Spontaneous compliance of the InP/$SrTiO_3$ heterointerface"*
G. SAINT-GIRONS, C. PRIESTER, P. REGRENY, G. PATRIARCHE, L. LARGEAU, V. FAVRE-NICOLIN, G. XU, Y. ROBACH, M. GENDRY, GUY HOLLINGER
Appl. Phys. Lett. **92**, 241907 (2008)

[3.17] *"Kink ordering and organized growth of Co clusters on a stepped Au(111) surface: A combined GISAXS, GIXD and STM study"*
F. LEROY, G. RENAUD, A. LÉTOUBLON, A. ROHART, Y. GIRARD, V. REPAIN, S. ROUSSET, A. COATTI, Y. GARREAU
Phys. Rev. B **77**, 235429 (2008)

[3.17] *"Growth of Co on Au(111) studied by multiwavelength anomalous grazing-incidence small-angle x-ray scattering: From ordered nanostructures to percolated thin films and nanopillars"*
F. LEROY, G. RENAUD, A. LETOUBLON, R. LAZZARI,
Phys. Rev. B **77**, 235429 (2008).

[3.17] *"Self-organized growth of Ni clusters on a cobalt-oxide thin film induced by a buried misfit dislocation network"*
P. TORELLI, E.A. SOARES, G. RENAUD, L. GRAGNANIELLO, S. VALERI, X. GUO AND P. LUCHES,
Phys. Rev. B **77**, 081409(R) (2008)

[1.89] *"Effects of thermal annealing on C/FePt granular multilayers: in situ and ex situ studies"*
D. BABONNEAU, G. ABADIAS, J. TOUDERT, T. GIRARDEAU, E. FONDA, J.-S. MICHA and F. PETROFF,
J. Phys : Cond. Mat. **20**, 035218 (2008)

[1.86] *"Coalescence of domes and superdomes at a low growth rate or during annealing: Towards the formation of flat-top superdomes"*
M.-I. RICHARD, G. CHEN, T.U. SCHÜLLI, G. RENAUD, G. BAUER,
Surf Sci. **602**, 2157 (2008).

[1.86] *"Structural investigation of silicon nanowires using GIXD and GISAXS: Evidence of complex saw-tooth faceting"*

T. DAVID, D. BUTTARD, T. SCHÜLLI, F. DALLHUIN, P. GENTILE
Surf. Sci **602**, 2675 (2008).

[1.45] « Looking by grazing incidence small angle x-ray scattering at gold nanoparticles supported on rutile TiO2(110) during CO oxidation »
M.C. SAINT-LAGER, A. BAILLY, M. MANTILLA, S. GARAUDEE, R. LAZZARI, P. DOLLE, O. ROBACH, J. JUPILLE, I. LAOUFI, P. TAUNIER
Gold Bulletin **41**, 159 (2008)

[1.41] *"Real time investigation of the growth ofsilicon carbide nanocrystals on Si(100) using synchrotron X-ray diffraction"*
S. MILITA, M. DE SANTIS, D. JONES, A. PARISINI, V. PALERMO,
Applied Surface Science **254**(7), 2162 (2008)

"Structure and morphology of thin MgO films on Mo(001) "
S. BENEDETTI, P. TORELLI, S. VALERI, H.M. BENIA, N. NILIUS, G. RENAUD
Phys. Rev. B accepted 2008

"Hydrophilic low temperature direct wafer bonding"
C. VENTOSA, F. RIEUTORD, L. LIBRALESSO, C. MORALES, F. FOURNEL, H. MORICEAU,
J. Appl. Phys. accepted

Book Chapters :

-"Chapter 10: Nanostructures in the light of synchrotron radiation: Surface sensitive x-ray techniques and anomalous scattering"
T. METZGER, V. FAVRE-NICOLIN, G. RENAUD, H. RENEVIER, T. SCHÜLLI
Chapitre de livre: « Characterization of Semiconductor Heterostructures and Nanostructures »
Edited by C. Lamberti, Elsevier 2008, p 361-403

-F. Rieutord, in X-ray and neutron reflectivity edited by A. Gibaud and J. Daillant
(Springer, Berlin, 2008).

PhD-thesis

M. I. Richard « "The growth of Ge islands on nominal and pre-patterned Si(001) surfaces: in situ and ex situ X-ray studies" Univ. Joseph Fourier, December 14, 2007.

B. Mallard (soutenance en attente) ILL-ENSAM (Metz) « Alliage CuBeAl à mémoire de forme »

Vincent Consonni « Mécanismes de structuration et de dopage au chlore dans le CdTe polycristallin. » 22 Octobre 2008
l'Institut polytechnique de Grenoble, spécialité Matériaux, Mécanique, Génie Civil, Electrochimie

Michel Eberlein « Contraintes locales induites par le procédé 'Shallow Trench Isolation' : Diffraction X haute résolution et simulation par éléments finis » 24 janvier 2008, Université Paul Cézanne, Marseille

Delphine Borivent « Interdiffusion réactive dans le système Ni-Si. » Physique et Sciences de la Matière, Université Paul Cézanne, Marseille
24 Juin 2008

2007

Publications:

(2) [9.63] "Grazing incidence X-ray measurements of epitaxial InAs/InP nanowires."
J. EYMERY, F. RIEUTORD, V. FAVRE-NICOLIN, O. ROBACH, L. FRÖBERG, T. MÅRTENSSON, and L. SAMUELSON
Nano Letters **7** (2007) 2596–2601.

(0) [4] “Unexpected stability of phospholipid langmuir monolayers deposited on triton X-100 aqueous solutions”
P. FONTAINE, M.C. FAURE, F. MULLER, M. POUJADE, J.S. MICHA, F. RIEUTORD, M. GOLDMANN
Langmuir **23**(26), 12959 (2007)

(1) [3.60] "Strain field in silicon on insulator lines using high resolution x-ray diffraction »
GAILHANOU M, LOUBENS A, MICHA JS, CHARLET B., MINKEVICH AA, FORTUNIER R., THOMAS O.
Appl. Phys. Lett. **90** (2007) 111914

(2) [3.17] « Self-similarity during growth of the Au/TiO_2(110) model catalyst as seen by the scattering of x-rays at grazing-angle incidence “
R. LAZZARI, G. RENAUD, J. JUPILLE, AND F. LEROY
Phys. Rev. **B 76** (2007) 125412

(1) [3.17] “Grazing-incidence small-angle x-ray scattering from dense packing of islands on surfaces: Development of distorted wave Born approximation and correlation between particle sizes and spacing “
R. LAZZARI, F. LEROY, AND G. RENAUD
Phys. Rev. **B 76** (2007) 125411

(2) [3.17] “Size and temperature dependent epitaxy for a strong filmsubstrate mismatch : the case of Pt/MgO(001)”
J. OLANDER, R. LAZZARI, J. JUPILLE, B. MANGILI, J. GONIAKOWSKI, G. RENAUD
Phys. Rev. **B 76** (2007) 075409

(2) [3.17] "Inversion of the diffraction pattern from an inhomogeneously strained crystal using an iterative algorithm »
MINKEVICH AA, GAILHANOU M, MICHA JS, CHARLET B., CHAMARD V., THOMAS O.
Phys. Rev. **B 76** (2007) 104106

(0) [3.17]*"Structure and magnetic properties of Mn/Pt(110)-(1x2): a joint x-ray diffraction and theoretical study”*
M. DE SANTIS, Y. GAUTHIER, H. C. N. TOLENTINO, G. BIHLMAYER, S. BLÜGEL, V. LANGLAIS,
Phys. Rev. B **75**, 205432 (2007)

(1) [3.17]*"Role of hydrogen interaction in two-dimensional molecular packing with strong molecule-substrate bonding"*
V. LANGLAIS, X. TORRELLES, Y. GAUTHIER, M. DE SANTIS,
Phys. Rev. B **76**, 035433 (2007).

(0) [2.17] “Quantitative study of hydrogen-implantation-induced cavities in silicon by grazing incidence small angle x-ray scattering »
L. CAPELLO, F. RIEUTORD, A. TAUZIN, F. MAZEN
J. Appl. Phys. **102** (2007) 026106

(4) [1.86] “X-ray scattering from stepped and kinked surfaces: An approach with the paracrystal model »
LEROY F, LAZZARI R, RENAUD G
Surf. Sci. **601** (2007) 1915-1929

(0) [1.86] “Nanostructuration of a CoO film by misfit dislocations”
P. TORELLI, E. A. SOARES, G. RENAUD, S. VALERI, X. X. GUO AND P. LUCHES
Surf. Sci. **601** (2007) 2651-2655

(1) [1.86] “Structural and morphological evolution of Co on faceted Pt/W(111) surface upon thermal annealing”
C. REVENANT, F. LEROY, G. RENAUD, R. LAZZARI, A. LETOUBLON, T. MADEY
Surf. Sci. **601** (2007) 3431

(0) [1.86]*"Chlorine chemisorption on Cu(001) by surface X-ray diffraction: Geometry and substrate relaxation"*
H. C. N. TOLENTINO, M. DE SANTIS, Y. GAUTHIER, V. LANGLAIS,
Surf. Science **601** (2007) 2962-2966

(0) [1.86]*“Surface structure and composition of the missing-row reconstruction of $VC_{0.8}$(110): A LEED,*

GIXRD and photoemission study"
Y. GAUTHIER, I. ZASADA, M. DE SANTIS, V. LANGLAIS, C. VIROJANADARA,
Surf. Science **601** (2007) 3383-3394

(2) [1.38] "*New reactor dedicated to in operando studies of model catalysts by means of surface x-ray diffraction and grazing incidence small angle x-ray scattering*"
M.-C. SAINT-LAGER, A. BAILLY, P. DOLLE, R. BAUDOING-SAVOIS, P. TAUNIER, S. GARAUDÉE, S. CUCCARO, S. DOUILLET, O. GEAYMOND, G. PERROUX, O. TISSOT, J.-S. MICHA, O. ULRICH, and F. RIEUTORD
Rev. Sci. Instrum. **78** (2007) 083902

(0) [1.32] "*Water penetration mechanisms in nuclear glasses by X-ray and neutron reflectometry*"
REBISCOUL D, RIEUTORD F, NE F, FRUGIER P,CUBITT R, GIN S
J. Non Cryst. Solids **353** (2007) 2221-2230

(0) [1.21] "*Investigation by High Resolution X-ray Diffraction of the local strains induced in Si by periodic arrays of oxide filled trenches* »
EBERLEIN M, ESCOUBAS S, GAILHANOU M, THOMAS O., MICHA JS, ROHR P., COPPARD R.
Phys. Stat. Sol.**A 204** (2007) 2542-2547

(0) "*Structure of the 3C-SiC(100)-5x2 Surface Reconstruction Investigated by Synchrotron Radiation Based Grazing Incidence X-ray Diffraction"*
M. SILLY, H. ENRIQUEZ, J. ROY, M. D'ANGELO, P. SOUKIASSIAN, T. SCHÜLLI, M. NOBLET AND G. RENAUD
Mater. Sci. Forum **556-557**, 533 (2007).

ESRF Highlights:

ESRF Highlights 2007: "Determination of the complete stress state of sub-micrometric Cu grains by microdiffraction", p 77
O. SICARDY, X. BIQUARD, J.S. MICHA, F. RIEUTORD, O. ROBACH, O. ULRICH, O. GEAYMOND, V. CARREAU

ESRF Highlights 2007: "From now to then: real-time studies, nanoscale surface faceting", p 79
C. REVENANT, F. LEROY, G. RENAUD, R. LAZZARI, A. LETOUBLON, T. MADEY

INAC Bulletin 2007 : « Laue back at work at ESRF », J.S. MICHA *et al ,* August 2008

Brevet:

L. Libralesso, C. Morales, H. Moriceau, F. Rieutord,
Brevet Traitement de surface par plasma d'azote dans un procédé de collage direct

Conférences invités:

"Strain determination in nanostructures via X-ray scattering measurements"
O. Thomas et al.
SizeDepEn Workshop Size-dependent materials behaviour: Challenges in miniaturisation and materials characterisation - March 15th -16th 2007, Fraunhofer Institut für Werkstoffmechanik Freiburg (Allemagne)

"Local strains in micro and nanostructures using synchrotron radiation"
O. Thomas et al.
ICMCTF 2007, International Conference on Metallurgical Coatings and Thin Films, April 23-27, 2007 San Diego, USA

“Diffraction analysis of elastic strains in micro- and nano-structures (keynote lecture)”
O. Thomas et al.
Size&Strain V 2007, "Diffraction analysis of the microstructure of materials",
October 7-9 2007, Garmisch-Partenkirschen (Allemagne).

4 lectures on: Deducing strains and stresses from X-ray diffraction
Advanced synchrotron techniques and small dimensions
O. Thomas et al.
CISM - International Centre for Mechanical Sciences -Mechanical Size-Effects of Materials: Processing, Characterization and Modeling - Udine, May 12 - 16, 2008.

“ La diffraction des rayons X et la mécanique des nano-objets : état de l'art et perspectives » (Conférence semi-plenière)
O. Thomas et al.
11ème Journées de la Matière Condensée - Strasbourg août 2008

« Strain measurements at the nanoscale: micro-beam Laue scattering and coherent x-ray diffraction »
O. Thomas et al.
EPDIC 11, European Powder Diffraction Conference, Varsovie, 18 septembre 2008

« Local strains in micro and nanostructures using synchrotron radiation »
O. Thomas et al.
NANOSTRESS school, Cargese, 29 septembre - 5 octobre 2008

« X-ray structural studies of nanowires »
. J. Eymery
3SN'2008, Summer School on Semiconductor Nanowires, GDR Nanofils Nanotubes Semiconducteurs, june 15-20, 2008, Roscoff, France

,« Guided growth on templates – Use of strain
J. Eymery
Nanostress, Cargese Summer School, CNRS-Max Planck-Fraunhofer-Carnot, 29 Sept. – 5 Oct. 2008 »

“Structure and dynamic of DNA confined between non cationic lipid membranes”
L. Navailles, E. Andreoli de Oliveira, F. Nallet, E. Grelet, A. Fevrier & J. Dobrindt
2nd French Brazilian Polymer Meeting FBPOL2008, 20-25 April 2008, Florianòpolis, Brazil.

“ Organization of DNA fragments between lipid bilayers”
E. Andreoli de Oliveira, L. Navailles, , F. Nallet, E. Grelet, A. Fevrier & J. Dobrindt
Workshop of application of synchrontron radiation on soft matter, fev. 2008, LNLS- Campinas – Brasil

“Study of Fluctuation and Destabilization of Single Phospholipidic Bilayer by Neutron and X-ray Scattering”
T. Charitat et al
54th AVS Meeting,
Seattle, 14-19 Octobre 2007

“Neutron and X-ray scattering to investigate supported bilayer's physical Properties”
T. Charitat et al
Biological Physics at Large Facilities, 19-23 Grenoble, Octobre 2008